SPECTRAL ENGINEERING VIA SILICON NANOCRYSTALS GROWN BY PECVD

SPECTRAL ENGINEERING VIA SILICON NANOCRYSTALS GROWN BY ECR-PECVD FOR PHOTOVOLTAIC APPLICATIONS

By

JUSTIN SACKS

B.Eng.

A Thesis Submitted to the School of Graduate Studies

in Partial Fulfillment of the Requirements for the Degree of

Master of Applied Science

McMaster University

© Copyright by Justin Sacks, August 2012

MASTER OF APPLIED SCIENCE (2012) McMaster University

Department of Engineering Physics Hamilton, Ontario

TITLE: Spectral Engineering Using Silicon Nanocrystals Grown by ECR-PECVD for Photovoltaic Applications

AUTHOR: JUSTIN SACKS, B.Eng., (Carleton University, Ottawa, Ontario)

THESIS SUPERVISOR: Rafael Kleiman

THESIS SUPERVISOR: Peter Mascher

NUMBER OF PAGES: xii, 111

Abstract

The aim of third-generation photovoltaics (PV) is ultimately to achieve low-cost, high-efficiency devices. This work focused on a third-generation PV concept known as down-shifting, which is the conversion of high-energy photons into low-energy photons which are more useful for a typical solar cell. Silicon nanocrystals (Si-NCs) fabricated using electron-cyclotron resonance plasma-enhanced chemical vapour deposition (ECR-PECVD) were studied as a down-shifting material for single-junction silicon cells. A calibration was done to determine optimal deposition parameters for Si-NC formation. An experiment was then done to determine the effect of film thickness on emission, optical properties, and photoluminescence quantum efficiencies.

Photoluminescence (PL) peaks varied depending on the stoichiometry of the films, ranging from approximately 790 nm to 850 nm. Variable-angle spectroscopic ellipsometry was used to determine the optical constants of the Si-NC films. The extinction coefficients indicated strong absorption below 500 nm, ideal for a down-shifting material. Transmission Electron Microscopy (TEM) was used to determine the size, density, and distribution of Si-NCs in two of the films. Si-NCs were seen to have an average diameter of approximately 4 nm, with larger nanocrystals more common near the surface of the film. A density of approximately 10^5 nanocrystals per cubic micron was approximated from one of the TEM samples.

The design and implementation of a PL quantum efficiency measurement system was achieved, using an integrating sphere to measure the absolute efficiency of Si-NC emission. Internal quantum efficiencies (IQE) as high as 1.84% and external quantum efficiencies (EQE) of up to 0.19% were measured. The EQE was found to increase with thicker films due to more intense photoluminescence; however the IQE remained relatively independent of film thickness.

Acknowledgements

I would like to thank my supervisors, Dr. Peter Mascher and Dr. Rafael Kleiman, for always being approachable and encouraging, and for their generous contribution of expertise and guidance. Thanks to Jacek Wojcik for his efforts in training me on several pieces of equipment and sharing his years of experience growing and characterizing thin-films. Thanks to Patrick Wilson and Martin Gerber for sharing their vast knowledge and providing much-needed advice. It was a pleasure working with Rachel Savidge, my partner on this project, whose integrity and work were always of the highest quality. I would also like to thank my parents, Linda and Daniel, and my sister, Joella for their resolute belief in my abilities, and my better half, Lara Rovet, who so often kept me grounded, and provided much support and motivation throughout my degree.

Finally, I would like to acknowledge generous funding from the NSERC Photovoltaic Innovation Network. It was an honour to collaborate with such renowned researchers and be a part of a network committed to strengthening the photovoltaic industry in Canada.

Contents

List of Figures

List of Tables

Chapter 1

Introduction

1.1 The Need for Solar Energy

It is becoming more apparent as our global energy demand continues to grow that a dependence on unsustainable and unclean natural resources is not a viable option for future generations. Not only does the continued addiction to burning fossil fuels cause a global warming effect, but with peak oil predicted to be reached as early as 2015 [1], there simply will not be enough natural resources to meet future energy demands. For these reasons, there is increasing pressure to find alternative sources of clean, cheap, and renewable energy for residential, commercial, and industrial settings as well as for transportation and consumer goods.

The sun provides approximately 100,000 terawatts (TW) of power annually to the earth, while the total power consumed annually by humans is approximately 15 TW [2]. Even considering absorption by molecules in the atmosphere, there is enough energy from the sun incident on the Earth in two hours to meet the annual energy requirement of the entire planet. Solar energy can be utilized naturally, through the growth of biomass that can be converted into ethanol; thermally, by heating water to power a turbine; or through the photovoltaic (PV) effect to directly create electricity from photons. Photovoltaic devices are good candidates to provide a significant portion of the world's energy; however, their feasibility is limited at this time due to lack of suitable storage options, high manufacturing and installation costs, and the low efficiencies of commercial photovoltaic products.

The current viability of solar energy throughout most of the world is heavily dependent on economic policies that incentivise its installation and use. Germany, the current world leader in solar energy, is a prime example of how policies can grow the industry and implementation. The German incentive program was introduced in 1990, and directly correlates with the increased number of solar installations. Similar programs have successfully made renewable energy economically viable in the U.S., Canada, Germany, Spain, France, China, Pakistan, and Australia [3]. Though incentives for renewable energy can sometimes be met with skepticism from the public with regards to causing the rise of electricity prices, a recent study by the Pembina institute showed that such incentives do not significantly increase the cost of electricity for consumers, and will in fact decrease costs in the long term [4].

The reason solar energy is currently so policy-dependent is primarily due to the high manufacturing cost associated with photovoltaic devices. “Grid parity” is a term that describes the point where the cost of solar energy matches the price of electricity in the region. This happens at different times depending on the cost of electricity in the specific location of interest. Once grid parity is achieved, solar energy becomes economically viable without any incentives. Though grid parity is inevitable in all regions due to the ever-increasing costs of traditional energy, it is the aim of researchers all over the world to both decrease the cost and increase the efficiency of solar cells. The former is generally done using cheaper or fewer materials, as well as utilizing mass production and economies of scale. The latter is somewhat more challenging, since current technology is approaching the physical limitations of photovoltaic devices. The following sections will briefly discuss these limitations, and proposed methods of overcoming them.

1.2 Fundamental Limit of Photovoltaic Devices

With the emergence of photovoltaic devices in the 1950's came the publication of Shockley and Queisser's renowned paper detailing the theoretical limit to a conventional semiconductor photovoltaic device [5]. This limit, which was referred to as the *detailed balance* limit, was determined based on several key assumptions:

1. The sun emits as a black body with a temperature of 6000 K;
2. The device is a p-n junction, made of a semiconductor with bandgap E_g;
3. Each incident photon with energy > E_g produces a single charge carrier in the cell, and each with energy < E_g produces no effect on the cell;
4. The only recombination within the photovoltaic device is radiative.

The final assumption was necessary since photovoltaic generation could not occur without the opposite process, radiative recombination.

As a black body, the sun emits according to Planck's law, and its total emitted energy distribution can be written as follows:

$$P_s = \frac{2\pi h}{c^2}\int_0^\infty \frac{v^3 dv}{e^{\left[h\nu/kT\right]}-1} = \frac{2\pi (kT)^4}{h^3 c^2}\int_0^\infty \frac{x^3 dx}{e^x - 1}, \tag{1.1}$$

where v is the frequency of an emitted photon, related to its energy by $E = h\nu = xkT$. The total power incident on the photovoltaic device is then given by:

$$P_{incident} = A \cdot P_s, \tag{1.2}$$

where A is the surface area of the device. When considering all photons that contribute to the generation within the photovoltaic device, the cut-off frequency, v_g, and the bandgap,

$E_g = h\nu_g = x_g kT$, needs to be considered. The total photon flux that will contribute to the photovoltaic device as per assumption 3 above is therefore given by:

$$Q_s = \frac{2\pi}{c^2}\int_{\nu_g}^{\infty} \frac{\nu^2 d\nu}{e^{\left[h\nu/kT\right]} - 1} = \frac{2\pi (kT)^3}{h^3 c^2}\int_{x_g}^{\infty} \frac{x^2 dx}{e^x - 1}, \tag{1.3}$$

which is the Planck energy distribution divided by the energy per photon and integrated over the range of energy above the band gap.

The total power emitted by the device then needs to be determined, as:

$$P_{emitted} = h\nu_g A Q_s . \tag{1.4}$$

Equations (1.2) and (1.4) can then be used to calculate the ultimate efficiency, defined as the ratio between input and output power, and can be written as a function of x_g:

$$u(x) = \frac{P_{emitted}}{P_{incident}} = \frac{h\nu_g A Q_s}{A P_s} = \left[x_g \int_{x_g}^{\infty} \frac{x^2 dx}{e^x - 1} \right] \Bigg/ \left[\int_0^{\infty} \frac{x^3 dx}{e^x - 1} \right] \tag{1.5}$$

The result of Equation (1.5) is shown in Figure 1.1 as a plot of ultimate efficiency versus device bandgap. It is shown that a maximum efficiency is approximately 44%, at the point where v_g = 2.2 eV.

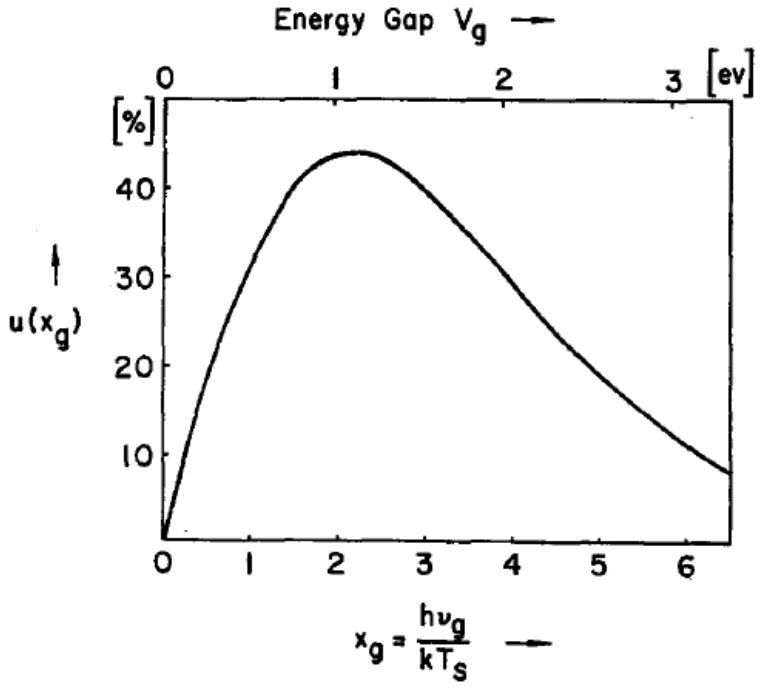

Figure 1.1: Ultimate efficiency versus energy gap (V_g) of a photovoltaic device [5].

Since the ultimate efficiency only considers radiative recombination, it is not an accurate indication of the maximum performance of a photovoltaic device. The *detailed balance* limit is calculated assuming that the radiative recombination is only a portion of the total recombination, with the rest being non-radiative. This limit was calculated to be approximately 32% for an optimal band gap of 1.35 eV, which corresponds well with the band gap of several widely used semiconductors.

The Shockley-Queisser paper provided insight into the limitations of photovoltaic devices, and for many years reaching the limiting efficiency proved to be the Holy Grail for single-junction solar cells. However, if photovoltaics are to experience widespread deployment and

integration, it will be worthwhile to aim for a higher limit than the detailed balance efficiency for single-junction devices.

1.3 Third Generation Photovoltaics

There have been many advances in photovoltaic technology that have led to the birth of so-called third generation PV [6]. The aim of third generation photovoltaics is to obtain a power conversion efficiency greater than the theoretical efficiency for conventional photovoltaic solar cells described in Section 1.2, while maintaining cost-effective production. Multijunction cells utilize more than a single band gap in order to circumvent the Shockley-Queisser limit, and therefore are considered third generation devices; however these cells are generally expensive and therefore limited in their commercialization potential.

Figure 1.2 shows the efficiency versus cost for first, second, and third generation cells, which correspond to conventional wafer-based cells, thin-film cells, and advanced thin-film cells, respectively. It is interesting to note that the efficiency of second generation cells is lower than that of first generation cells, but the cost-effectiveness of second generation cells outweighs this drawback.

Regarding third generation solar cells, there are three main concepts that have emerged as candidates to create cheap and efficient cells:

1. Intermediate band cells
2. Hot carrier cells
3. Spectral engineering

The first two will be discussed briefly, while the third will be the main topic of this thesis.

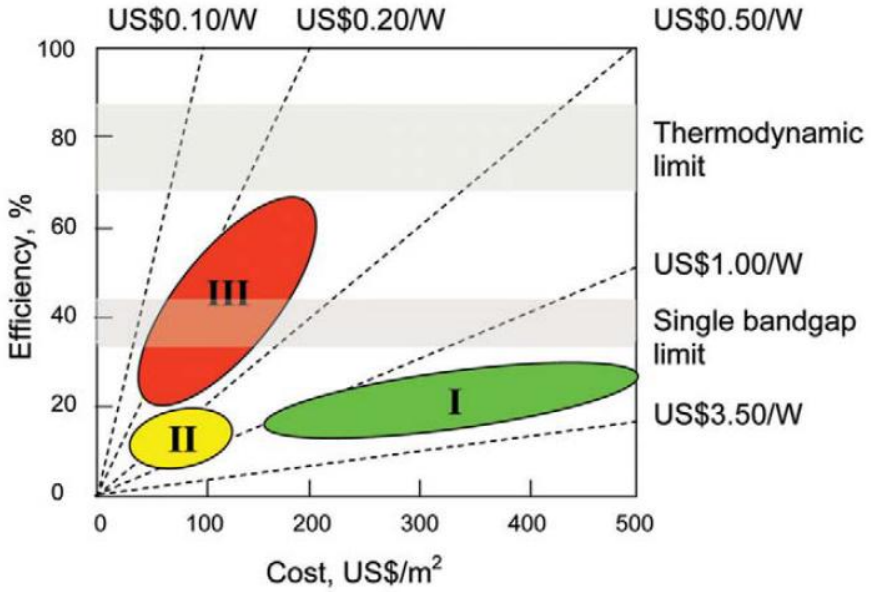

Figure 1.2: Map of efficiency versus cost for first, second, and third generation PV devices [6].

1.3.1 Intermediate Band Cells

Intermediate band cells (IBCs) began in 1960 with Wolf's notion of using localized impurity states to form multiple low-energy pathways from the valence band to the conduction band [7]. This was claimed to theoretically allow for sub-band gap photons to contribute to the photocurrent without the need for a second junction. It was soon realized that excessive non-radiative recombination would have been introduced with localized mid-gap states, negating any gain from low-energy photon absorption. In 1997, Luque identified the need to have an intermediate band rather than localized states, which he claimed would eliminate much of the non-radiative recombination due to wavefunction overlap in the intermediate band [8]. Since then, attempts have been made to fabricate IBCs using III-V semiconductors doped with transition metals [9], chalcopyrite-based materials [10], and quantum dots [11] [12] [13], with the latter

method perhaps having the greatest potential. Much theoretical work is being done on IBCs, however an efficient device with commercialization potential has yet to be fabricated.

1.3.2 Hot Carrier Cells

Hot carrier cells aim to collect carriers while they are still “hot”, in other words, before they have thermalized down to the conduction-band edge, wasting excess energy to heat [6]. In order to do this, the thermalization rate needs to be slowed and carrier collection needs to occur selectively, at high energies. This would allow higher voltages to be produced by a cell, contingent on selective contacts that have very narrow acceptance energy ranges. Much theoretical work has been done on hot carrier cells, however they still remain an elusive technology in the experimental realm.

1.3.3 Spectral Engineering

The final method of producing third generation cells to be discussed, and the main topic of this thesis, is the engineering of the incident spectrum to better suit a photovoltaic device. Much of the fundamental inefficiencies of photovoltaic devices derive from the broad nature of the solar spectrum. The selectivity of the absorption of semiconductors is not well-suited for such a broad spectrum, and therefore introduces inefficiencies at both high and low energies, relative to the band gap. This is illustrated in Figure 1.3, where the external quantum efficiency (EQE) of a typical single-junction silicon cell is shown overlapping the AM1.5G spectrum. It can be seen in both the high and low wavelength regions that a portion of the sun’s energy falls outside of the optimal range of the cell, and will therefore be susceptible to energy loss.

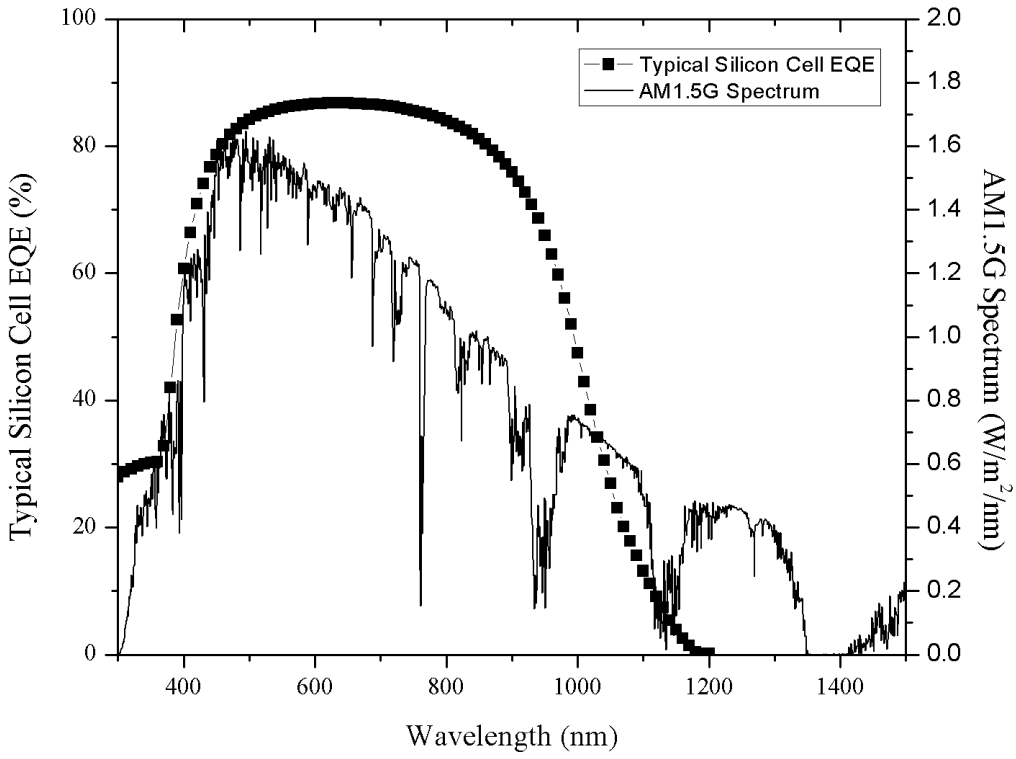

Figure 1.3: External Quantum Efficiency (EQE) for a typical single-junction silicon cell (squares); Air Mass 1.5G Spectrum (solid line), the energy from the sun that reaches the Earth's surface. A large portion of the energy within the AM1.5G spectrum falls under wavelengths corresponding to poor cell performance.

The long-wavelength, low-energy losses are introduced by a semiconductor material's lack of absorption of photons with sub-band gap energies. The material is essentially transparent to these photons, which therefore cannot contribute to the photocurrent. Short-wavelength, high-energy losses are due to two factors: thermalization and surface recombination [14]. The former is caused by the excess energy that a UV photon contains, given by $E_{excess} = E_{photon} - E_g$. This excess energy is rapidly thermalized and therefore wasted to heat as an electron excited by such a photon travels down to the conduction band edge. Photons with energy greater than twice the

solar cell's bandgap have enough energy to produce two charge carriers within the cell, and are therefore not being utilized effectively if thermalization occurs.

Surface recombination depends on the material quality, and is generally caused by defects or dangling bonds at the material's surface. These defects act as traps that induce non-radiative recombination, with a larger effect closer to the surface of the material, where high-energy photons are absorbed. These loss mechanisms are shown in Figure 1.4, along with the unavoidable and generally non-detrimental radiative losses.

The efficiency maximum of 32% for single-junction devices is seen at a band gap of 1.35 eV, as per the detailed balance limit described in Section 1.2. Approximately 30% of the incident energy loss is due to sub-band gap losses, and approximately 20% is due to thermalization losses. Note that this model does not account for surface recombination. Spectral engineering aims to mitigate these losses by moving the high-energy spectrum into a region where surface recombination and thermalization losses are reduced, and the low-energy spectrum into a region where photons have sufficient energy to excite carriers across the band gap. Specific processes that could potentially be used for spectral engineering will be discussed in Chapter 2.

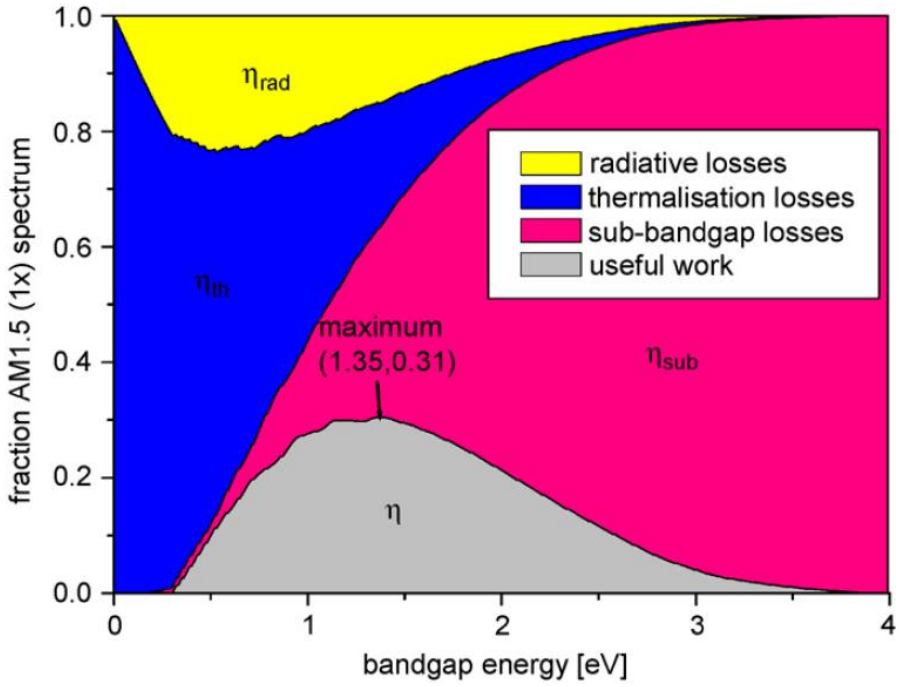

Figure 1.4: Fractional theoretical losses for the AM1.5 spectrum incident on a single-junction cell [14].

1.4 Chapter Summary

There is no question that a paradigm shift is needed in order to sustainably satisfy the energy requirements of the human population. Solar energy will undoubtedly play a large role in the future of energy production, however there is much work to be done on improving device efficiency and lowering manufacturing costs. The fundamental limit of traditional single-junction photovoltaic devices is approximately 32%, however third generation photovoltaics aims to surpass this limit while maintaining cost-effectiveness.

This work focuses on improving device efficiency by using the photoluminescence from silicon nanocrystals to alter the solar spectrum before it is incident on a cell. This process is known as down-shifting, one possible mechanism to achieve spectral engineering. The theoretical processes behind spectral engineering and silicon nanocrystal fabrication will be discussed in

Chapter 2, along with the theory behind ellipsometric measurements, a prominent characterization technique used in this work to determine the optical characteristics of thin films. Chapter 3 will focus on the method of measuring absolute photoluminescence quantum efficiency developed for this work. A discussion of the theory governing the integrating sphere used to take the quantum efficiency measurements will also be presented. Results from silicon nanocrystal fabrication and characterization will be presented in Chapter 4, starting with a calibration of the fabrication system, followed by a comparison of the photoluminescence from silicon nanocrystals grown on a silicon substrate with those grown on a fused silica substrate. The results from films of varying thicknesses will then be presented, as well as the photoluminescence quantum efficiencies from various nanocrystalline films. Chapter 5 will then provide suggestions for future improvements that can be made to the systems used in this work, and further work that can be done to better achieve the goal of an efficient spectral engineering material.

Chapter 2

Theory

This chapter will outline the theoretical knowledge that is requisite for this thesis. The subject matter is fairly multi-disciplined and independent, involving quantum mechanics, plasma physics, and optics. The theoretical scope was kept at a fairly high level in some cases, with more detail where the theory is well understood by the scientific community.

2.1 Down-Conversion and Down-Shifting

Down-conversion (DC) and down-shifting (DS) are both processes that convert high-energy photons into low-energy photons. The main difference between DC and DS is that DC processes conserve the energy of the original photon, while DS processes lose energy typically to thermalization. An illustration of each process is shown in Figure 2.1, showing high-energy photons being converted or shifted to low-energy photons. DC, also known as quantum-cutting or photon splitting, takes a photon with high energy E_λ as input, and outputs two photons, each typically with energy $E_\lambda/2$. DS, sometimes referred to as Luminescent Down-Shifting (LDS), takes a high-energy photon as input and outputs a single low energy photon, with energy $< E_\lambda$.

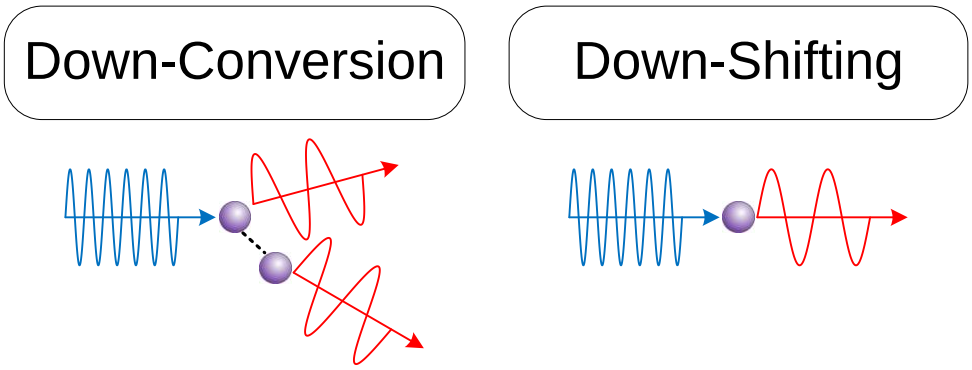

Figure 2.1: Illustration showing the down-conversion and down-shifting processes. The high-frequency waves represent high-energy photons, and the low-frequency waves represent low-energy photons.

The limiting efficiency of a solar cell with a perfect DC layer located on the top surface of the cell was calculated by Trupke et al. [15] to be 39.63% rather than the typical 30.9%. This result shows substantial improvement over the detailed balance limit discussed in Section 1.2. Richards' group has made significant progress in applying LDS layers to CdS/CdTe cells, improving their UV response by down-shifting photons that would have otherwise been absorbed by the CdS layer [16]; however, this process uses organic dyes that have unproven lifetimes. Finding an efficient DC material has been a much-researched topic [17], [18], [19], however currently, a stable and efficient conversion material still eludes the research community.

2.1.1 DC and DS from Silicon Nanocrystals

Since the discovery of optical emission from porous silicon made by Canham in 1990 [20], silicon has been pursued as a material for the opto-electronics and photons fields. Canham proposed that the visible photoluminescence (PL) originated due to quantum confinement effects that narrow the bandgap of silicon to the point where it becomes direct in nature. The need for phonon interaction in order for radiative recombination to take place is relaxed, making optical

emission much more likely. This is caused by *phonon confinement*, and occurs due to vibrational modes being spatially limited as a nanoparticle's dimension decreases [21].

Silicon nanocrystals (Si-NCs) have been shown to emit Gaussian-like luminescence, where the emission peak can be tuned from 750 nm to 950 nm [22], [23], [24], [25]. The emission peak depends on the size distribution of the nanocrystals, following the quantum confinement model. The model predicts that smaller nanocrystals will have larger band-gaps and therefore emit at shorter wavelengths than larger nanocrystals, which will have smaller band-gaps and emit at longer wavelengths [22].

Figure 2.2 shows a schematic diagram of DS (left) and DC (right) via Si-NCs. Both DS and DC processes initiate with the absorption of a high-energy photon, exciting an electron deep into the conduction band. This electron then transitions down to the conduction band edge. In the DS case, this excess energy is simply thermalized; however in the DC case, the energy is transferred to a neighbouring Si-NC, exciting a second electron into the conduction band. This energy transfer occurs through intraband Auger processes [26]. The excited electrons then radiatively recombine with holes in the valence band, emitting photons with lower energy than the original exciting photon. In order for this emission to be useful to a photovoltaic device, the bandgap of the Si-NCs must be at least equal to the bandgap of the semiconductor material used in the photovoltaic device.

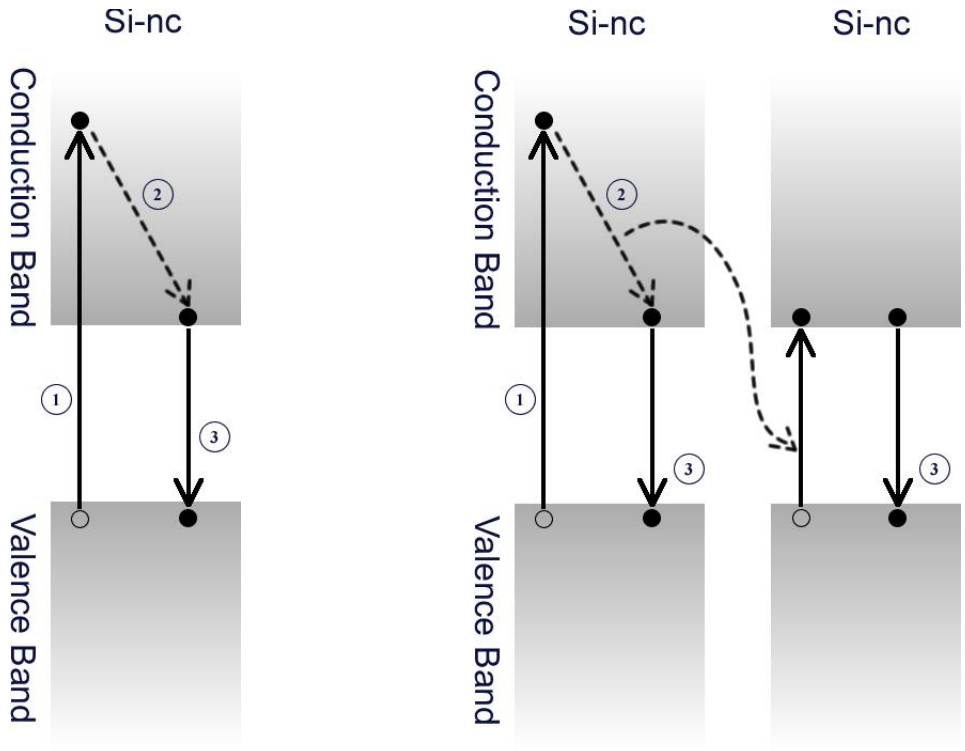

Figure 2.2: (Left) Down-shifting via silicon nanocrystal; (Right) Down-conversion via neighbouring silicon nanocrystals. A high-energy photon excites an electron into the conduction band (1); the excited electron thermalizes to the conduction band edge, and in the case of DC, excites a neighbouring silicon nanocrystal through intraband Auger processes (2); the electron(s) radiatively recombine, emitting photons with lower energy than the original exciting photon (3) [26].

Radiative emission from silicon nanocrystals is generally believed to originate from quantum confinement [24]; however it has been argued that emission actually comes from interface states between the Si-NCs and their host matrix [27], or possibly a combination of the two. A recent paper [28] suggests that core states are actually responsible for efficient emission from Si-NCs, and that quantum confinement does not in fact occur to the extent previously thought. Another study found that the absorption cross-section of Si-NCs implies that their bandgap is indeed indirect [29].

The typical absorption and emission profiles of Si-NCs coincide very well with the requirement for a down-conversion or down-shifting material to be applied to a single-junction silicon cell. This is illustrated in Figure 2.3, which shows a typical silicon cell EQE plotted over the typical absorption and emission profile of Si-NCs. It is clear that Si-NCs absorb at short wavelengths where the cell operates inefficiently, with absorption strength actually increasing into the UV as cell EQE decreases. The emission of the Si-NCs takes place around 800 nm, where the cell EQE is still at its highest.

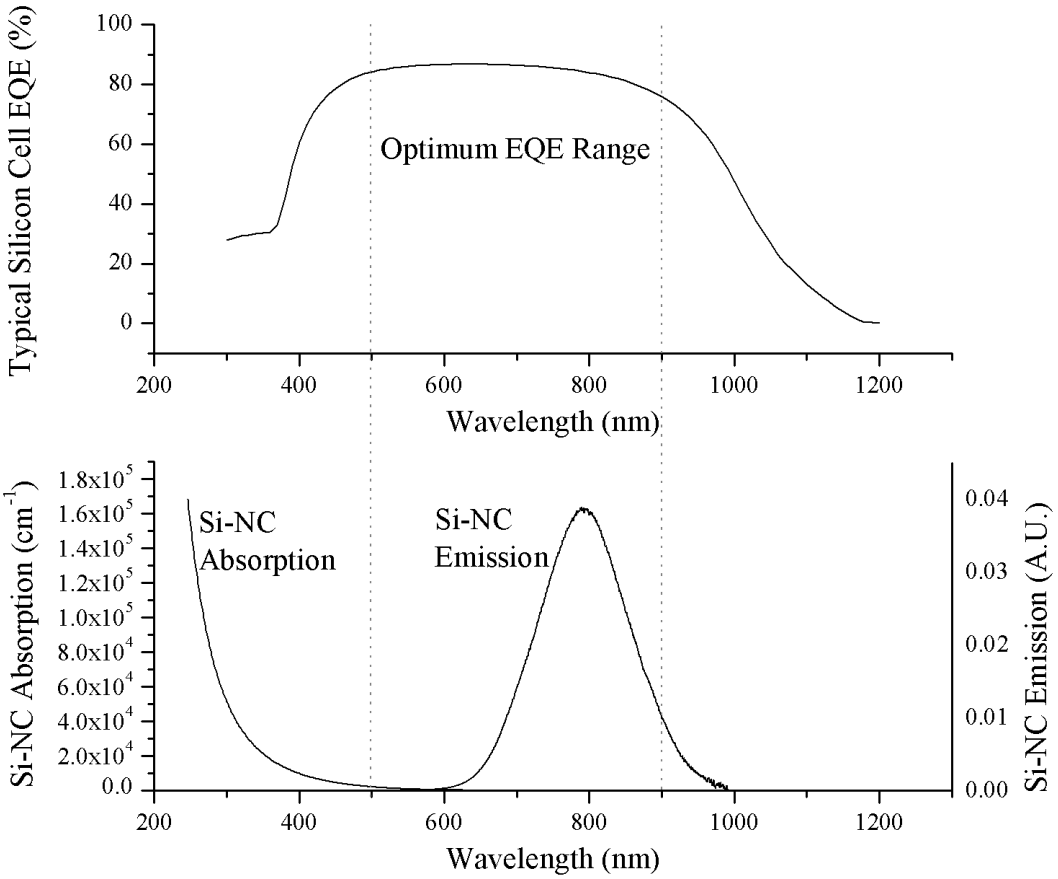

Figure 2.3: Typical single-junction silicon cell EQE plotted over typical absorption and emission values for Si-NCs.

This shows that Si-NCs are theoretically very good candidates for spectral engineering. However, quantum efficiencies of Si-NC emission are typically too low to improve cell performance unless the Si-NCs are fabricated in an oxygen-free environment and passivated with organic ligands [30], a condition which may hinder the commercialization process. Until emission efficiencies of stable Si-NCs are vastly improved, they may not alone be good candidates for a high-efficiency process such as DC.

2.1.2 DC and DS From Rare-Earth Ions

Rare-earth (RE) doping for optical emission tuning has been a topic of interest since the beginning of the 20th century, when sharp luminescence bands were discovered from the lanthanide elements. Dieke's comprehensive study [31] nicely documents the lanthanide energy levels. Erbium has specifically been a major research area in the telecommunications field due to the coincidence of the Er^{3+} emission band around 1535 nm and the corresponding low-absorption spectrum of silica optical fibres [32]. RE elements have a partially filled 4f shell, and RE ions are often formed by losing both 6s electrons and one 4f electron. Luminescence from these ions originates from intra-4f or 5d-4f transitions, the former being unaffected by external forces due to shielding from the 5d orbital [33]. This causes the emission wavelength to be independent of the host material, which is a very desirable feature for spectral engineering applications in photovoltaics.

Down-conversion can theoretically achieved doping semiconductor or ceramic substrates with single or double RE ions. These ions contain well-defined and separated energy levels that can be used for multiple radiative transitions within a single ion [18], as shown in Figure 2.4 (a). An electron excites the ion to its high-energy state, where it can experience two radiative relaxations to the middle and ground states sequentially. DC on single RE ions was first reported

with praseodymium (Pr^{3+}) in 1974, using an YF_4 host lattice to transfer energy to the RE ions [34].

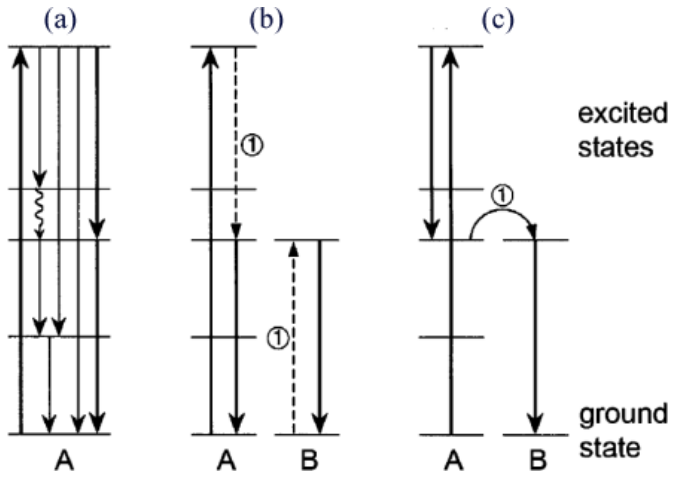

Figure 2.4: Theoretical mechanisms for down-conversion in rare-earth ions; (a) a single ion emits two photons through multiple radiative transitions; (b) ion pairs emit two photons by cross-relaxation from ion A to ion B; (c) energy transfer occurs from ion A to ion B, followed by radiative emission from both ions. Adapted from [18].

DC can also theoretically occur between two neighbouring RE ions that physically interact with each other, as shown in Figure 2.4 (b) and (c). Through either cross-relaxation as shown in (b), or energy transfer as shown in (c), excitation energy is transferred from the sensitizer ion A to the emitter ion B. If the total energy of the excited sensitizer ion is transferred to two neighbouring emitter ions either through cross-relaxation or energy transfer, DC will occur if the emitter ions relax radiatively [18]. DC has been shown in Er^{3+}-Yb^{3+} co-doped materials based in a PbF_2 matrix [35], as well as Eu^{2+}-Yb^{3+} doped CaF_2 [36].

2.2 Silicon Nanocrystal Growth via ECR-PECVD

An Electron Cyclotron Resonance (ECR) Plasma-Enhanced Chemical Vapour Deposition (PECVD) system was used in conjunction with a quartz tube furnace to create silicon nanocrystals on (100) silicon and fused silica substrates. Thin silicon-rich silicon-oxide films were deposited with specific stoichiometric properties and then annealed to form nanocrystals. The particular system and method used has been shown to create nanocrystals using silicon oxide and silicon nitride thin films [33], [37], [38], [39].

ECR is a phenomenon caused by the rotational motion of electrons in a static magnetic field due to the Lorentz force. ECR was observed by Dresselhaus, Kip, and Kittel in the 1950's within germanium and silicon solids in experiments used to measure effective masses of holes and electrons in crystals [40], [41]. The ECR phenomena can be used to generate plasma by impinging microwaves on electrons in a static magnetic field. The electrons have a rotational frequency ω_c given by

$$\omega_c = eB/m, \tag{2.1}$$

where *B* is the magnetic field strength, *e* is the electronic charge, and *m* the electronic mass. The microwave frequency is set specifically to match ω_c, satisfying the resonance condition and providing kinetic energy to the electrons. A gas is then introduced into the ECR chamber, where the gas molecules are ionized by the energized electrons, creating plasma. The ECR condition from Equation (2.1) is met when B = 875 Gauss, and the microwave source is a magnetron with a frequency of 2.45 GHz.

A schematic diagram of the ECR-PECVD system is shown in Figure 2.5, and images of the PECVD chamber and control systems is shown in Figure 2.6 The right image in Figure 2.5 was taken through an open port during chamber maintenance and cleaning, and shows the lower silane (SiH_4) dispersion ring. The plasma source gas in the system is a mixture of Ar and O_2, with varying ratio depending on the specific deposition parameters. Silicon is obtained through a gaseous silane precursor that is injected into the main chamber through the lower dispersion ring underneath the ECR zone. The silane dissociates in the plasma leaving free Si atoms to bond to the substrate. The substrate is attached to a heated stage to improve and control deposition rates and film quality.

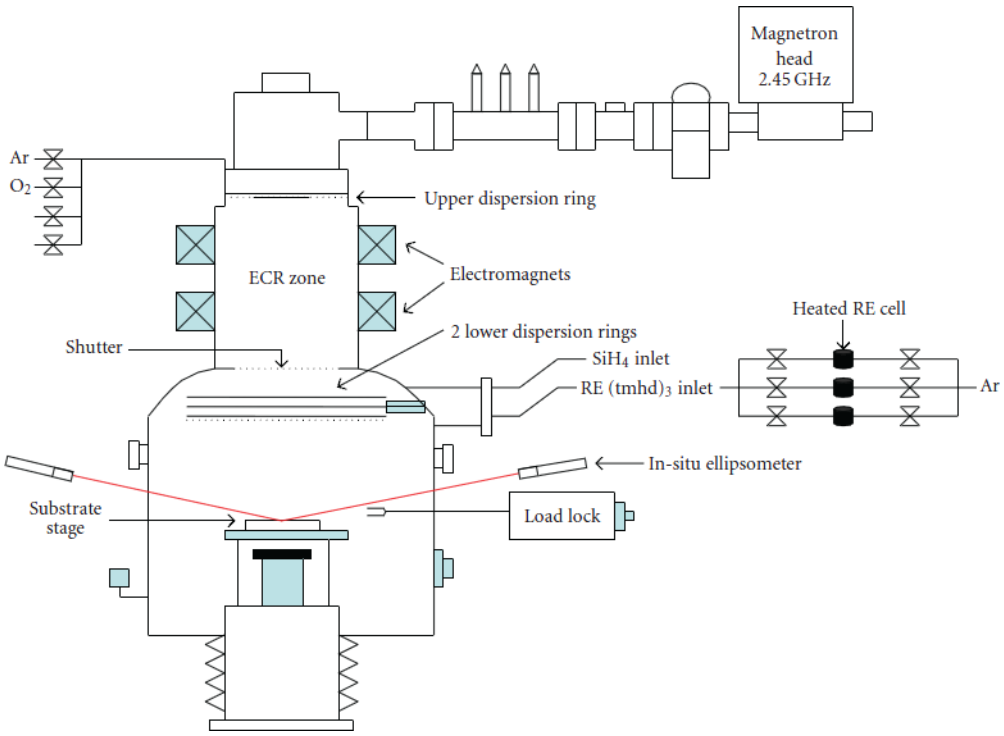

Figure 2.5: The ECR-PECVD system used to create Si-NCs [33].

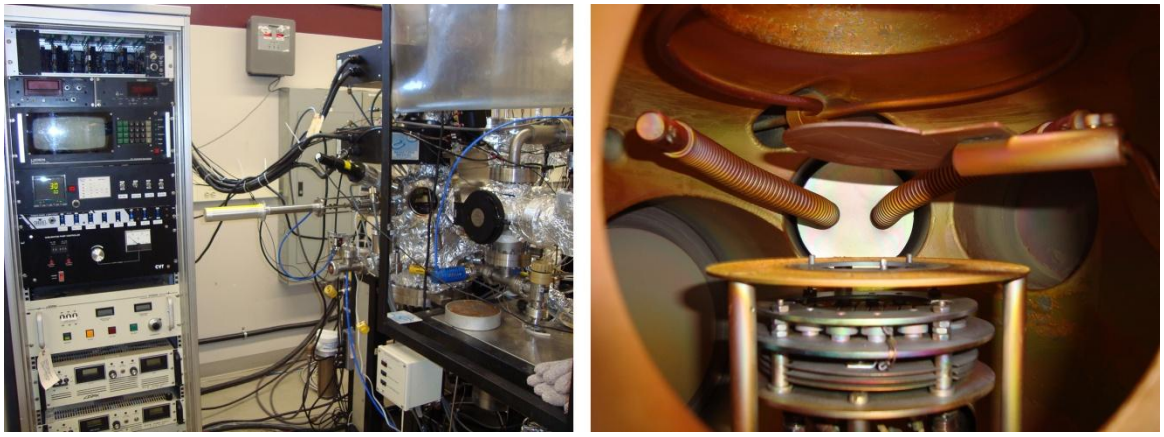

Figure 2.6: The ECR-PECVD system used in this work, including control systems, main chamber, and load lock (left); a close-up of the main chamber showing the lower dispersion ring, shutter, and heated sample stage (right).

ECR-PECVD was used to deposit thin films composed of silicon-rich silicon oxide (SRSO), with different Si:O ratios depending on the deposition parameters. The Si:O ratio was typically controlled by varying the O_2 flow rate, since varying the SiH_4 flow drastically affects the overall deposition rate. Since the plasma strength and deposition pressure depend on the O_2 flow, the Ar flow was varied to compensate for increasing or decreasing amounts of O_2. This is known as argon-compensated deposition.

Once the SRSO was deposited, the film was essentially an amorphous mix of Si and O with a high number of defects. High-temperature treatment in a quartz tube furnace was required to remove argon and oxygen-related defects from the film, as well as form the Si-NCs. The tube furnaces used in this work are shown in Figure 2.7. During high-temperature annealing (above 1000˚C), the excess silicon in the film clustered together and eventually crystallized. Annealing was performed in flowing H_2 (5%) N_2 (95%), which has been shown to improve luminescence intensity due to Si-NC surface passivation [38].

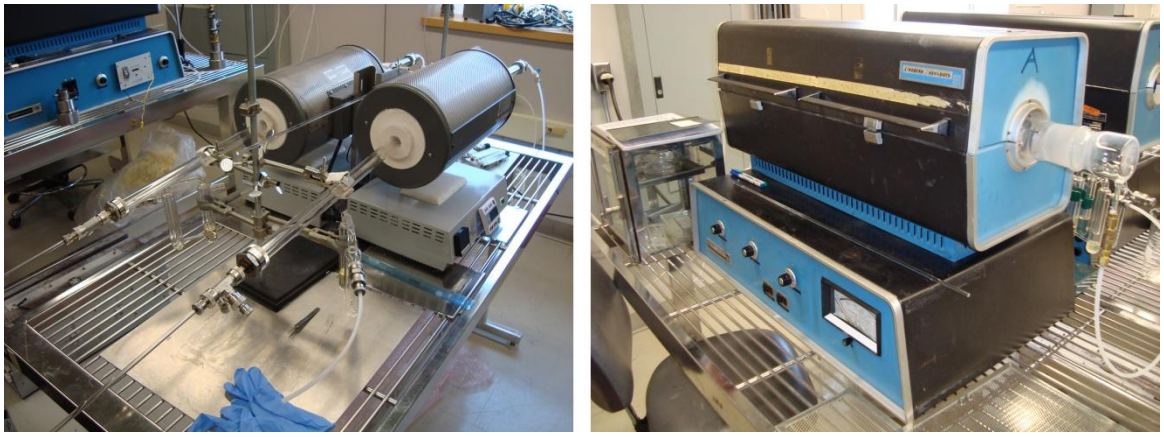

Figure 2.7: The two quartz tube furnaces used in this work to anneal silicon-rich thin films up to 1200˚C in flowing H_2 (5%) N_2 (95%).

The stoichiometry of the film ultimately governed the overall size of the Si-NCs, such that more silicon-rich films yielded larger nanocrystals. Specific deposition parameters and the properties of the resulting Si-NCs are discussed in Chapter 4. Due to the main goals of this project, a large variety of deposition parameters was not studied in this work; however the thesis entitled "SiO_xN_y Waveguides Deposited by Electron Cyclotron Resonance Chemical Vapour Deposition" by Marcel Boudreau discusses the effects of varying multiple deposition parameters.

2.3 Ellipsometry

Ellipsometry is a very useful and reliable technique for optically characterizing materials by measuring changes in polarization of light reflecting off of or transmitted through the film. Typically the polarized light is incident on the sample at the Brewster angle, where the measurement sensitivity is maximized [42], though some ellipsometers have variable-angle capability. Figure 2.8 shows an incident beam with electric field vectors E_{is} and E_{ip}, corresponding to the incident s- and p-polarized components, respectively. E_{rs} and E_{rp}, correspond to the

reflected s- and p- polarized components, respectively. Note that s-polarized vectors are perpendicular to the plane of the page.

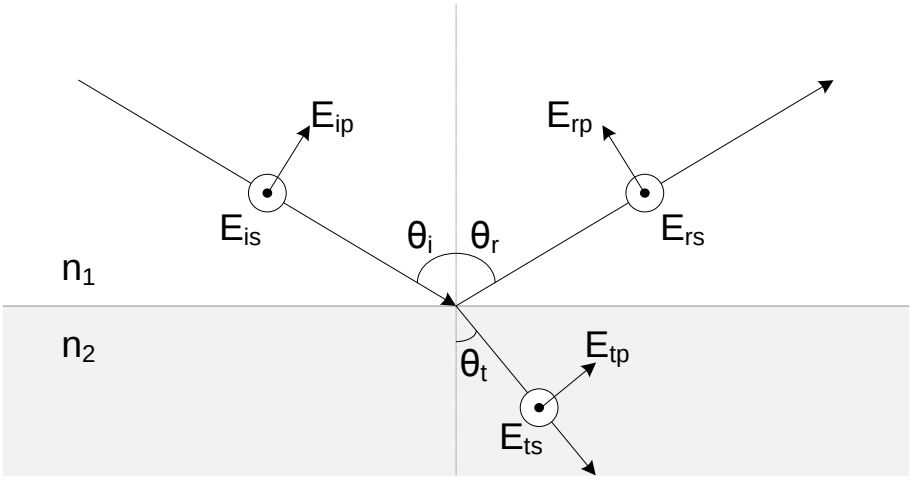

Figure 2.8: Incident, transmitted, and reflected s- and p-polarized light interacting at an interface between two mediums with refractive indexes n_1 and n_2.

The beam is incident on the sample at angle θ_i, reflected at θ_r and transmitted at θ_t, in accordance with Snell's laws. The amplitude reflection coefficients for s and p components are defined by:

$$r_s = \frac{E_{rs}}{E_{is}} \tag{2.2}$$

$$r_p = \frac{E_{rp}}{E_{ip}} \tag{2.3}$$

Figure 2.9 shows the basic principle behind an ellipsometric measurement, where the incident light is linearly polarized, thus E_{is} and E_{ip} have equal amplitudes and zero phase

difference. Since s- and p-polarized light interacts with electric dipoles at different angles, their reflection coefficients are very different around the Brewster angle, where ellipsometric measurements are taken. This creates different changes in amplitude and phase in each reflected s and p component, and causes the reflected light to be elliptically polarized. Ellipsometry measures this difference in amplitude and phase using two parameters: the amplitude ratio ψ and the phase difference Δ [42].

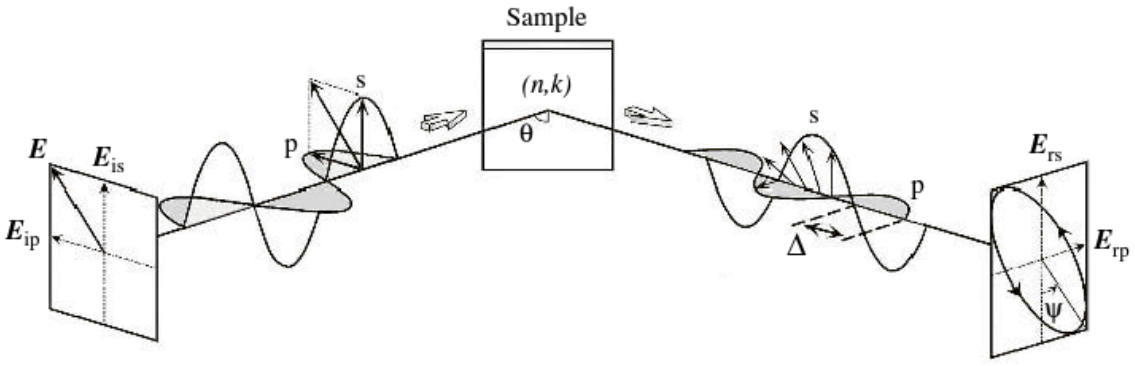

Figure 2.9: Schematic diagram showing an ellipsometry measurement with linearly-polarized incident light [42].

The parameters ψ and Δ are defined from the ratio of amplitude reflection coefficients defined in Equations (2.2) and (2.3):

$$\rho = \tan\psi e^{i\Delta} = \frac{r_p}{r_s} = \frac{E_{rp}}{E_{ip}} \Big/ \frac{E_{rs}}{E_{is}} = \frac{E_{rp}}{E_{rs}} \qquad \textbf{(2.4)}$$

Note that the last simplification in Equation (2.4) is due to the linear polarization of the incident beam, since $E_{ip}=E_{is}$, as previously mentioned. Representing Equation (2.4) using polar coordinates gives:

$$\tan\psi = \frac{|r_p|}{|r_s|}, \ \Delta = \delta_{rp} - \delta_{rs} \tag{2.5}$$

The optical constants can then be determined using the following relations [43]:

$$\varepsilon_1 + i\varepsilon_2 = (n+ik)^2 = \sin(\phi)^2\left[1+\tan(\phi)^2\cdot\left(\frac{1-\rho}{1+\rho}\right)^2\right], \tag{2.6}$$

Once an ellipsometric measurement has been taken, the experimental values of ψ and Δ are compared with predicted values from a model in the form of Equation (2.6) in order to get optical constants and film thickness. The amount of uncertainty in the comparison is measured as a Mean Square Error (MSE) value. Low MSE values indicate that the measured values are close to the predicted values, however it is important to ensure that optical constants are sensible even for low MSE models.

In this work, two ellipsometers were used: a single-wavelength Philips SD ellipsometer operating at 632.8 nm, and a JA Woollam M2000UI variable-angle spectroscopic ellipsometer, both shown in Figure 2.10.

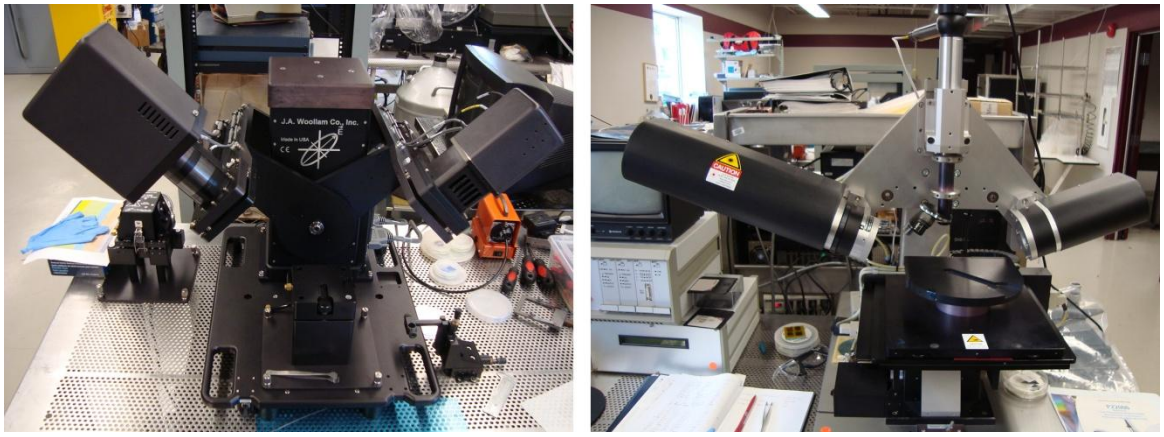

Figure 2.10: J.A. Woolam M2000UI variable-angle spectroscopic ellipsometer (left) and Philips PZ2000 single-wavelength ellipsometer (right) used in this work.

Chapter 3

Absolute Photoluminescence Quantum Efficiency Measurement

One of the main goals of this project was to design and implement a system for measuring photoluminescence quantum efficiency, also known as quantum yield. This chapter will outline the methods and calculations required to determine the PL quantum efficiency.

The implemented setup was roughly based on [45], however other methods of measuring PL quantum efficiency were found in the literature in [46] and [47]. Figure 3.1 shows a schematic diagram of the PL quantum efficiency measurement setup.

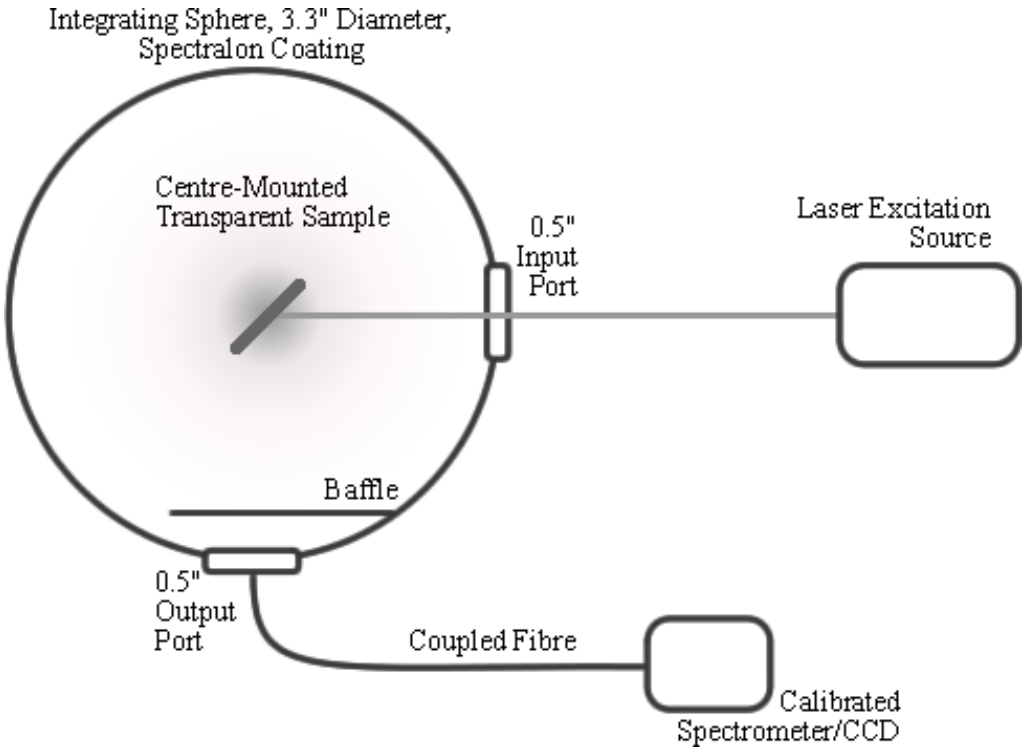

Figure 3.1: Schematic diagram of the absolute photoluminescence quantum efficiency measurement setup.

This setup was implemented using a custom-designed integrating sphere from LabSphere, and a spectrometer/CCD from Ocean Optics (USB2000+). The laser used for excitation was a 405 nm solid state laser operating at approximately 16 mW. This laser was used in lieu of the more common 325 nm HeCd laser due to its higher power, resulting in stronger emission from luminescent samples.

3.1 Integrating Sphere Theory

An integrating sphere is used to spatially integrate an optical flux while maintaining low amounts of loss [43]. The throughput of the sphere determines the radiant flux at the output port or coupled optical fibre relative to the input flux, and depends on many geometric and responsive parameters. This section will provide the necessary calculations for obtaining the sphere response, R_s, assuming a sphere with two ports: an input and exit port.

The radiance of a diffuse surface with area A and reflectance ρ being illuminated with a flux Φ_{in} is determined by [43]:

$$L = \frac{\Phi_{in}\rho}{\pi A} \tag{3.1}$$

The port fraction, f, which depends on the areas of the input and exit ports, A_i and A_e, respectively, and the total surface area of the sphere, A_s, determines how much of the light inside the sphere is lost to the port openings:

$$f = \frac{A_i + A_e}{A_s} \tag{3.2}$$

The amount of light on the interior surface of the sphere can then be written as:

$$L = \Phi_{in}\rho(1-f) \tag{3.3}$$

Equation (3.3) considers the fraction of the sphere's surface area that is open due to the layout of the ports on the sphere. The light inside the sphere will continue to reflect off the sphere walls, creating an infinite power series that simplifies to:

$$L = \frac{\Phi_{in}\rho(1-f)}{1-\rho(1-f)} \tag{3.4}$$

and the total surface radiance from within the sphere is determined to be:

$$L = \frac{\Phi_{in}}{\pi A_s}\frac{\rho}{1-\rho(1-f)} \tag{3.5}$$

Now the optical conditions at the exit port need to be considered for the sphere response. To determine the throughput of an open port, T_{port}, the port area A_p and the projected solid angle Ω need to be considered:

$$T_{port} = L \cdot A_{port}\Omega = \frac{\Phi_{in}}{\pi A_s} \frac{\rho}{1-\rho(1-f)} \cdot A_{port}\Omega \quad \textbf{(3.6)}$$

The solid angle of the port can be approximated by π for a fully open port [44]. When considering coupling from the exit port to an optical fibre with effective core diameter A_{fibre}, the final sphere response can be determined:

$$R_s(\lambda) = \frac{A_{fibre} \cdot (1-R) \cdot \Omega \cdot \rho}{\pi A_s \cdot (1-\rho(1-f))} \quad \textbf{(3.7)}$$

where R is the facial reflectivity of the fibre, and the solid angle Ω can be estimated as $\Omega = \pi \cdot (NA)^2$, NA being the numerical aperture of the fibre.

Figure 3.2 shows a plot of the sphere response used in this work as a function of wavelength. The sphere response is a step function due to low resolution of the reflectivity data, given in Appendix A, Table A.1. The fitted curve in Figure 3.2 is a smooth approximation of the sphere response using a 3rd order polynomial fit. The decrease in the sphere response from 700-850 nm is due to a slight decrease in the reflectance of the material coating the inside of the sphere in that particular wavelength range.

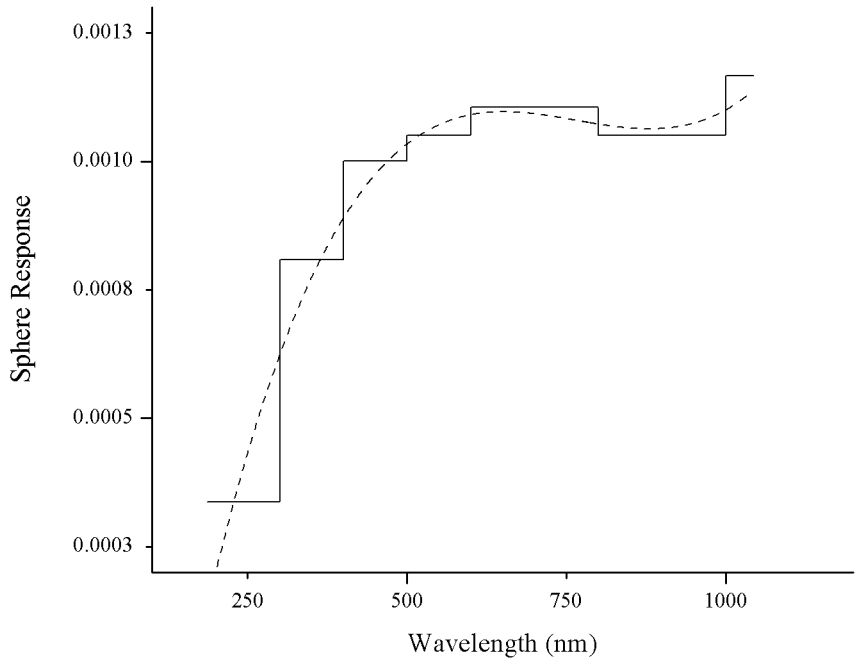

Figure 3.2: The integrating sphere response, R_s, plotted as a function of wavelength and fitted with a 3rd order polynomial.

The sphere response was used as a correction parameter for measurements taken within the sphere, and is a function of the reflectivity of the sphere coating, and therefore a function of wavelength. It corrected for any losses within the sphere or inefficient fibre-coupling from the sphere when taking measurements. The sphere response is unitless, but essentially shows the throughput of the sphere under measurement conditions when the total input power is 1 Watt. A measured spectrum is divided by the sphere response to obtain the corrected spectrum.

3.2 CCD Calibration

Since the ultimate goal of the photoluminescence quantum efficiency measurement was to measure the total number of photons entering and exiting the integrating sphere, the detector needed to be calibrated to measure units of absolute irradiance ($W/m^2/nm$) which could then be used to determine the corresponding photon flux. The calibration was done using an Ocean Optics LS-1-CAL lamp, designed for such absolute irradiance calibrations. The calibration lamp contained a data sheet consisting of the lamp's known irradiance as a function of wavelength. The data acquisition software, Spectrasuite, was used to create a calibration file while the calibration lamp was fibre-coupled directly into the CCD/Spectrometer. This calibration file contains the number of Watts per unit area per count, converting the raw data acquired by the detector (counts) into an absolute irradiance measurement. Absolute irradiance units could then be converted into a photon flux which gives the number of photons entering and exiting the sphere as a function of wavelength.

3.3 Measurements and Calculations

This section will describe the measurement method and calculations that were involved in determining the photoluminescence quantum efficiency of a light-emitting sample. The process is documented specifically regarding Si-NC samples deposited on fused silica, however could be applied to any light-emitting material.

3.3.1 Photoluminescence EQE

Photoluminescence external quantum efficiency (PL EQE) is defined by the ratio between incident and emitted photon flux, given by:

$$EQE = \frac{\phi_{emitted}}{\phi_{incident}} \tag{3.8}$$

where ϕ represents a photon flux in units of photons/m^2/s. The PL EQE is a measure of the overall luminescence efficiency without accounting for reflection, transmission or absorption within the material.

Measuring PL EQE first required an absolute irradiance measurement of the incident excitation source, in this case a 405 nm laser. The laser was directed into the empty sphere, where it was uniformly scattered with minimal absorption, and then coupled through the output port into a fibre leading to the calibrated CCD. The integration time on the CCD was generally short (~30 ms), to avoid saturating the detector. This measurement gave the absolute irradiance of the excitation laser, $I_{laser}(\lambda)$, which could be corrected for integrating sphere-related losses, converted to a spectral photon flux and then integrated to obtain the total photon flux that is incident on the sample:

$$\phi_{incident} = \int_0^\infty \frac{I_{laser}(\lambda) \cdot R_s(\lambda)^{-1}}{hc/\lambda} \cdot d\lambda \tag{3.9}$$

The hc/λ term in Equation (3.9), where h is Planck's constant and c is the speed of light, is the amount of energy in Joules per photon at wavelength λ. Including this term converts Watts (Joules/second) into photons/second, giving a photon flux. The $R_s(\lambda)$ term is the sphere response, calculated in Section 3.1 and shown in Figure 3.2, and corrected for any losses present due to the sphere geometry and non-ideal reflectivity.

Obtaining the emission spectrum was done by placing the luminescent sample in the centre of the sphere directly in the path of the excitation laser. The photoluminescence was collected by the sphere and coupled into the CCD through a fibre. A low-pass filter was used to block the laser light from entering the fibre in order to avoid saturating the detector, and the integration time was generally long (~30 s), since the PL signal tended to be relatively weak. Once the absolute irradiance of the PL, I_{PL}, was collected from within the sphere, it was converted to a photon flux similarly to Equation (3.9):

$$\phi_{emitted} = \int_0^{\infty} \frac{I_{PL}(\lambda) \cdot R_s(\lambda)^{-1} \cdot}{hc/\lambda} d\lambda \qquad \textbf{(3.10)}$$

Once the emitted and the incident photo fluxes were measured and corrected, the EQE could be calculated as per Equation (3.8).

3.3.2 Photoluminescence IQE

Photoluminescence internal quantum efficiency (PL IQE) accounts for reflection and transmission when considering the efficiency of light-emitting samples. The internal quantum efficiency is defined as the ratio of emitted to absorbed photons, given by:

$$IQE = \frac{\phi_{emitted}}{\phi_{absorbed}} \qquad \textbf{(3.11)}$$

There are two perspectives when measuring PL IQE, one that considers the entire converter and the other that only considers the active material, in this case, Si-NCs. The former

considers the substrate that the active material is deposited on, for example fused silica, which will ultimately absorb some of the light and therefore affect the IQE.

In order to calculate IQE, the emitted photon flux was measured as described in Section 3.3.1, Equation (3.10). The absorbed photon flux was obtained by measuring the effect of the sample on the laser intensity measured from within the sphere. In the case of measuring the IQE of the entire converter, this was done by first measuring the photon flux from the laser incident on the empty integrating sphere, $\phi_{reference}$. In the case of measuring the IQE of only the Si-NCs (or any other active material), $\phi_{reference}$ was measured with a blank piece of the substrate used when growing the sample mounted in the centre of the sphere. The photon flux of the laser was then measured with the desired luminescent sample mounted in the centre of the sphere, giving ϕ_{sample}. The photon fluxes $\phi_{reference}$ and ϕ_{sample} were determined from their corresponding absolute irradiance measurements using the methods previously outlined. The absorbed photon flux is then obtained by taking the difference of the laser photon flux with and without the converter or active material:

$$\phi_{absorbed} = \phi_{reference} - \phi_{sample} \quad \textbf{(3.12)}$$

Once the absorbed photon flux of either the active material or the entire converter was measured, the PL IQE could then be determined based on Equation (3.11).

Chapter 4

Results and Discussion

This section will outline the main results obtained in this work. The initial calibration of the PECVD system for Si-NC growth is presented and discussed, followed by a study of the effects of modifying the film thickness. Finally, the photoluminescence quantum efficiency of various Si-NC samples is presented.

4.1 Calibration for Silicon Nanocrystal Growth

Si-NCs were grown in a silicon-rich silicon oxide thin-film using the PECVD system and method described in Section 2.2. An initial calibration of the system was done to obtain optimal growth parameters for Si-NCs, followed by a fine-tuning of parameters to obtain size variation in the Si-NCs. Calibration films were grown on a silicon substrate with varying oxygen gas flows. By controlling the O_2:SiH_4 gas flow ratio, the final silicon composition and therefore also the size of the Si-NCs could be controlled.

Table 4.1 shows the deposition parameters for the calibration films. All films were grown at a deposition pressure of 2.1 mTorr, with the substrate heated to 120˚C. The base pressure of the system was in the 10^{-7} to 10^{-8} mTorr range, and magnetron power was set such that the forward power minus the reflected power, or the effective forward power was 500 W (typically forward power was 505 W and reflected power was 5 W). Gas flows are in units of standard cubic centimeter per minute (sccm), and all calibration films were deposited for 20 minutes. Films were allowed one hour after deposition to cool before removing them from the PECVD chamber. All films were annealed in a quartz tube furnace for 1 hour in 5 sccm of H_2 (5%) N_2 (95%).

Table 4.1: Deposition parameters for calibration films, including gas flows (sccm) and partial pressures (mTorr). The error for all gas flow values is ±2.5 sccm.

Sample Id	Ar + SiH_4 Flow (sccm)	Ar + SiH_4 PP (mTorr)	Ar + O_2 Flow (sccm)	Ar + O_2 PP (mTorr)	Ar Flow (sccm)	Ar PP (mTorr)
Cal-1	2.50	0.24	25.00	1.86	0.0	0.00
Cal-2	2.50	0.23	8.00	0.69	15.5	1.18
Cal-3	2.50	0.22	6.00	0.52	18.0	1.36
Cal-4	2.50	0.23	4.00	0.35	19.5	1.52
Cal-5	2.50	0.22	5.00	0.43	19.2	1.45
Cal-7	2.50	0.22	4.90	0.43	19.5	1.45
Cal-8	2.50	0.22	5.30	0.45	19.3	1.43

The average deposition rate was approximately 62 Angstroms per minute. It is also apparent that increasing the oxygen flow increased the deposition rate slightly, though increasing the silane flow had a much more drastic effect on overall deposition rate. One film (not shown) deposited with double the silane flow (5.0 sccm) had approximately double the deposition rate as the other films and was far too silicon rich to yield Si-NCs.

The calibration allowed the determination of the stoichiometric range corresponding to the formation of Si-NCs, as well as the deposition rate corresponding to the specific gas flows and deposition temperature. The stoichiometry of the films was estimated by measuring the refractive index through single-wavelength ellipsometry. Stoichiometric SiO_2 has an index of 1.46 at 632.8 nm, while excess silicon in the film increases the index exponentially.

Figure 4.1 shows the relation between oxygen flows used for SRSO deposition, and the resulting refractive index of the as-deposited films, measured at 632.8 nm. This data was measured using the single-wavelength Philips PZ2000 ellipsometer shown in Section 2.3, Figure

2.10. It can be seen that the refractive index decreases as the oxygen flow increases, indicating lower silicon content. The oxygen flow directly correlates with the Si:O ratio in the film, meaning that lower oxygen flows will yield more silicon-rich films and therefore higher refractive indexes.

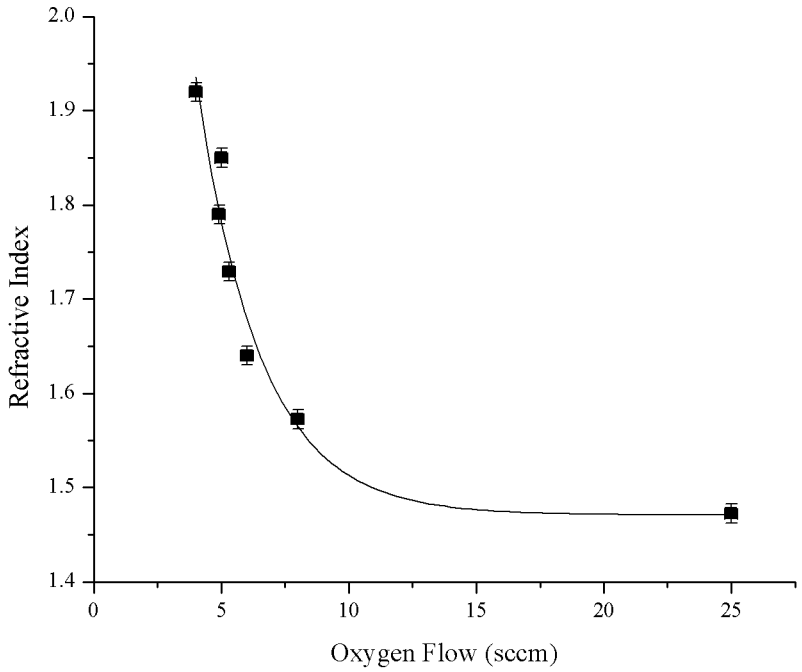

Figure 4.1: A plot of the refractive index of as deposited films measured at 632.8 nm vs. oxygen flow during deposition.

The results of the calibration, shown in the next section, showed that Si-NCs form in films with stoichiometry corresponding to a refractive index in the range of 1.7 – 1.9. As shown in Figure 4.1, there is a sharp increase in refractive index below 10 sccm O_2, and a very narrow region of about 4 to 6 sccm O_2 where the refractive index is in the range of Si-NC formation. These samples include a finer calibration that was done to tune the PL based on the Si-NC size, whereby larger Si-NCs created by having more silicon in the film yielded a more red-shifted PL

peak. Error bars were calculated based on the mass flow controller specifications, and experimentally determined uncertainty in the ellipsometric measurement.

4.1.1 Photoluminescence Spectra

Photoluminescence for all films was obtained using a room-temperature PL spectroscopy system previously designed and built by Zalloum et al. [48], and shown schematically in Figure 4.2. A 325 nm laser beam was directed onto a sample mounted on an x-y-z stage, and the PL normal to the sample was collected by front-end optics and coupled into a 600 μm fibre. A USB2000+ CCD/Spectrometer was used in place of the QP600-2 quoted in [48], using Spectrasuite as the acquisition software. The CCD was calibrated as described in Section 3.2.

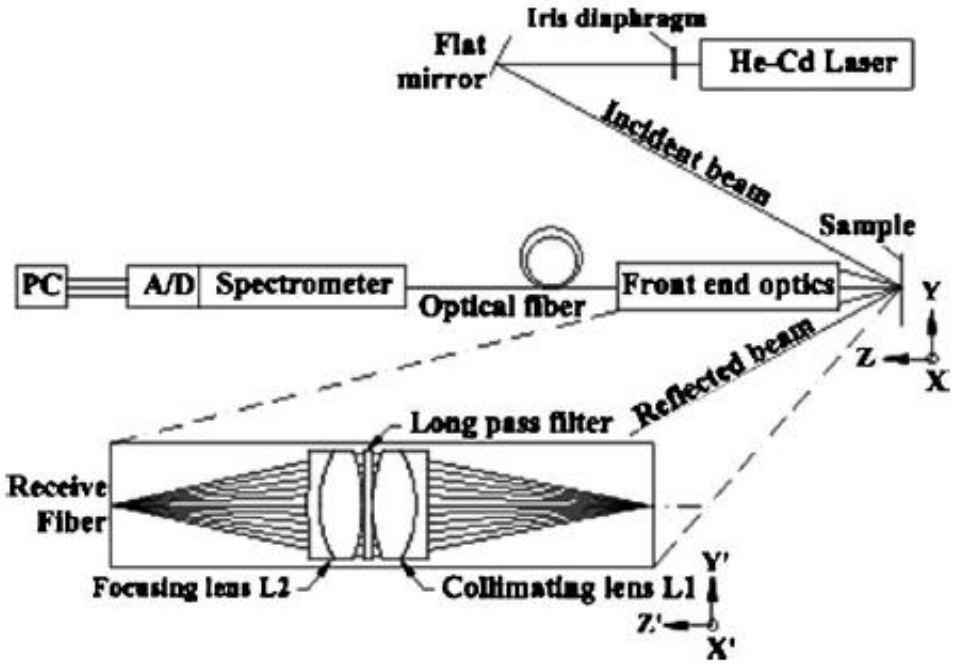

Figure 4.2: Schematic diagram of the photoluminescence spectroscopy system [48].

Figure 4.3 shows the photoluminescence spectra of all calibration samples after high-temperature annealing at 1100˚C - 1150˚C. Cal-1 had negligible PL after annealing, and the intensity of both Cal-2 and Cal-3 PL decreased after annealing, as shown in Figure 4.4, Figure 4.5, and Figure 4.6, respectively. This was due to the high number of oxygen-related defects present in the films, and insufficient excess silicon to form Si-NCs. Cal-1 specifically was close to stoichiometric SiO_2, and therefore the lack of PL after annealing was expected and characteristic. The PL peak wavelength of Cal-2 and Cal-3 indicated defect-related luminescence, since it did not change with annealing temperature, and was centered in the visible range of the spectrum [49], [50]. Since these particular films were deposited using the highest oxygen flows, a larger number of oxygen defects was present in these compared to the other calibration films. During the annealing process, these defects are either repaired or evaporated, and the defect-related luminescence decreases or disappears altogether.

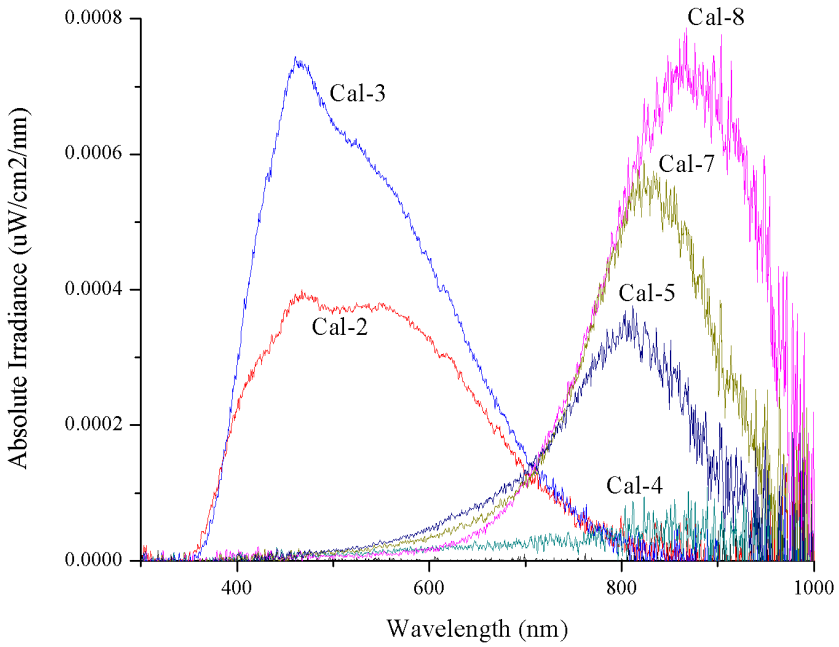

Figure 4.3: Photoluminescence spectra of calibration films after annealing at 1100˚C. Cal-2 and 3 show defect luminescence, while Cal-4, 5, 7 and 8 show luminescence from Si-NCs. Cal-1 had no luminescence after annealing.

The first calibration film showing signs of Si-NC luminescence was Cal-4, with PL shown in Figure 4.7. Though the PL intensity was small, it was centered around 780 nm, which is indicative of Si-NCs. Cal-5, 7 and 8 showed strong signs of Si-NC formation since characteristic PL occurred after annealing at 1100˚C, as seen in Figure 4.8, Figure 4.9, and Figure 4.10, respectively. A redshift can also be seen, most clearly in Figure 4.10 (Cal-7) with higher annealing temperatures. This is likely due to larger Si-NCs forming at higher temperatures, and therefore emitting longer-wavelength photons.

The defect-related emission intensities are comparable and in some cases higher than the Si-NC emission intensities. This indicates that defect states can be relatively efficient emitters,

however the reproducibility and stability of these luminescent materials has yet to be studied. Since the Si-NC films were all approximately the same thickness, the emission intensities did not drastically vary between samples.

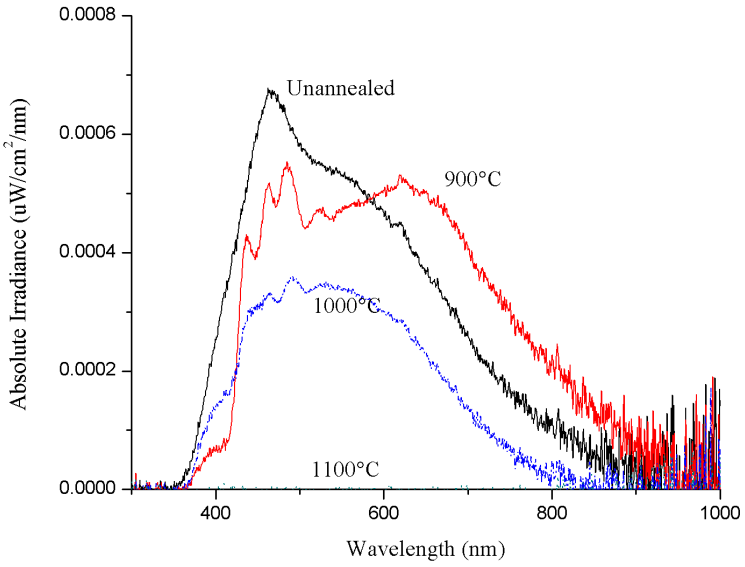

Figure 4.4: Photoluminescence from Cal-1. PL is likely caused by defect states since the PL intensity decreased with annealing temperature, and the peak wavelength did not shift significantly.

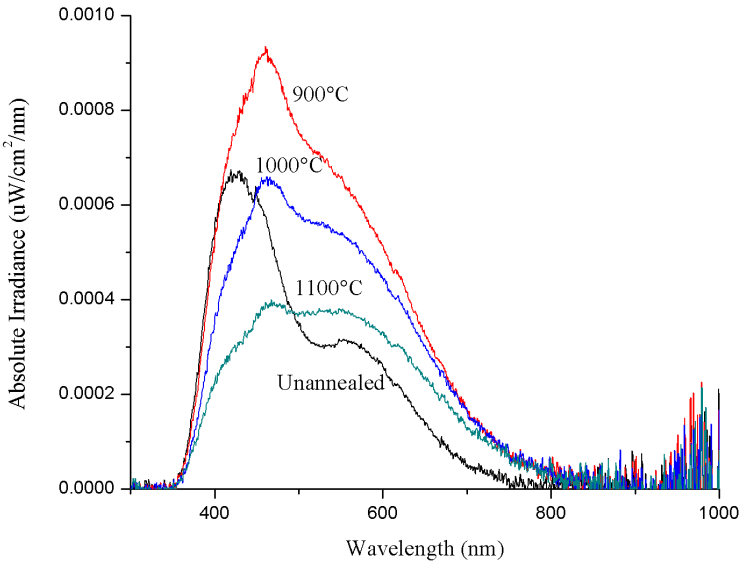

Figure 4.5: Photoluminescence from Cal-2. PL is likely caused by defect states since the PL intensity decreased with annealing temperature, and the peak wavelength did not shift significantly.

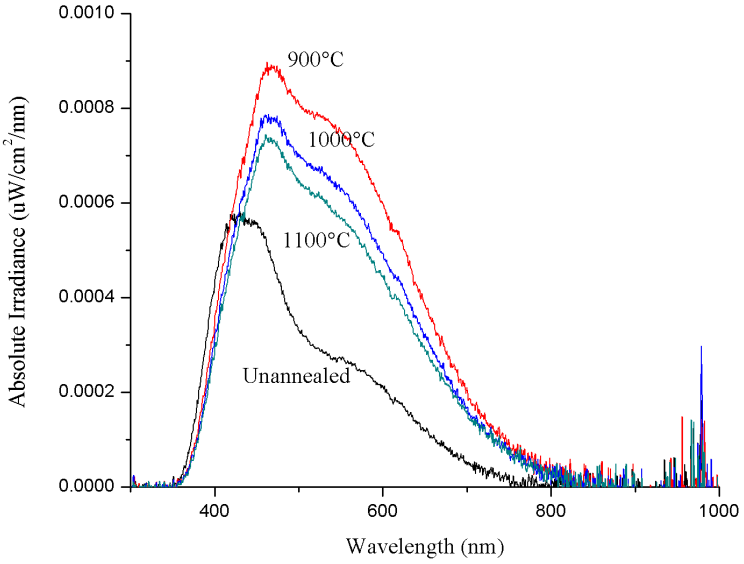

Figure 4.6: Photoluminescence from Cal-3. PL is caused by defect states due to the decreasing intensity with annealing temperature, and unchanging peak wavelength.

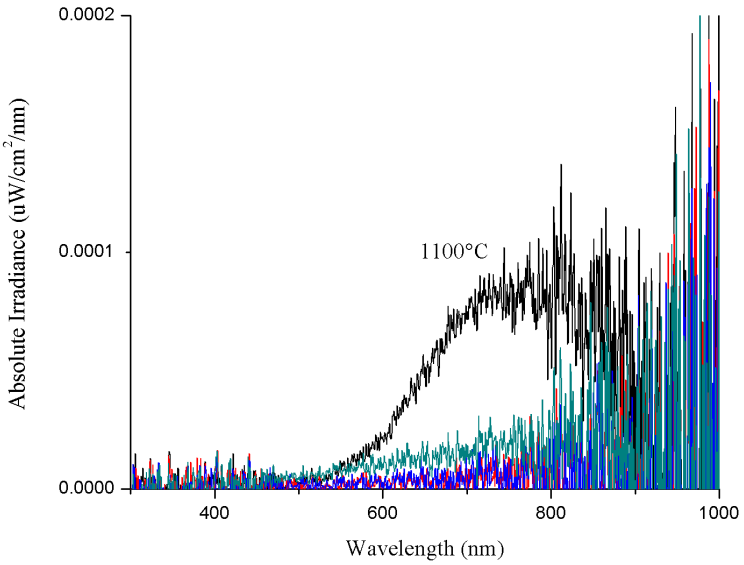

Figure 4.7: Photoluminescence from Cal-4. PL may be occurring from Si-NCs formed after an 1100˚C anneal.

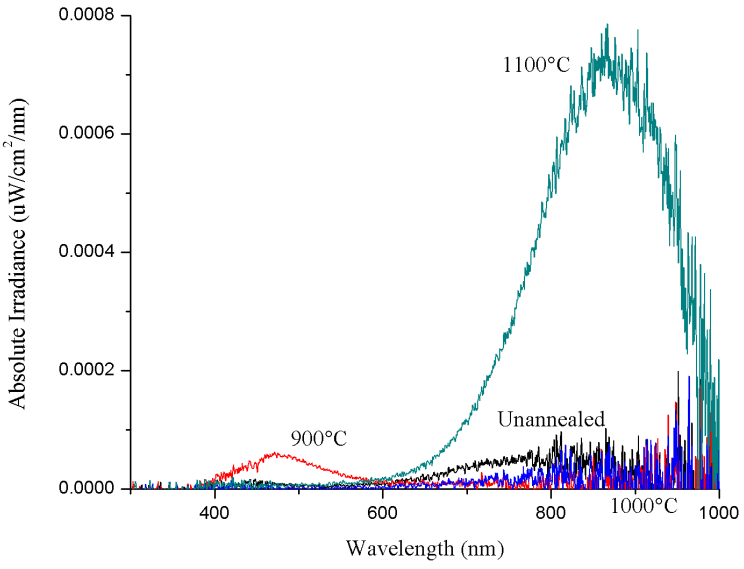

Figure 4.8: Photoluminescence from Cal-5. PL is likely due to Si-NCs formed after annealing at 1100˚C.

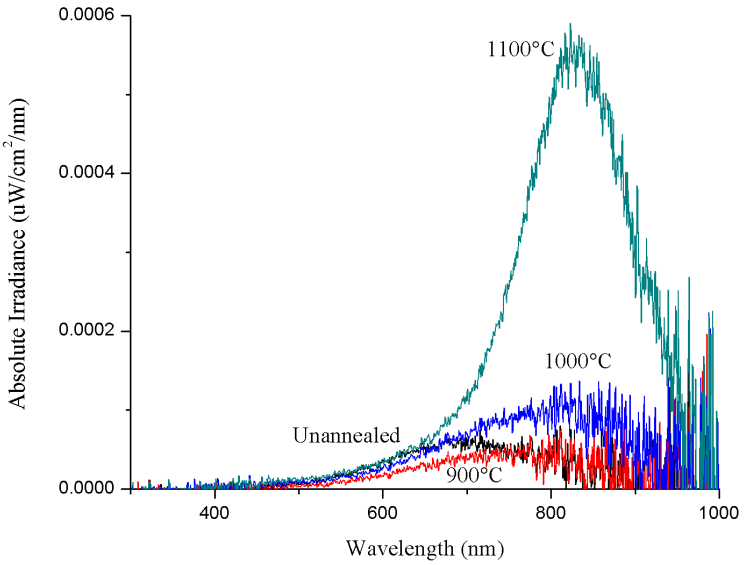

Figure 4.9: Photoluminescence from Cal-7. PL is likely due to Si-NCs formed after annealing at 1100˚C.

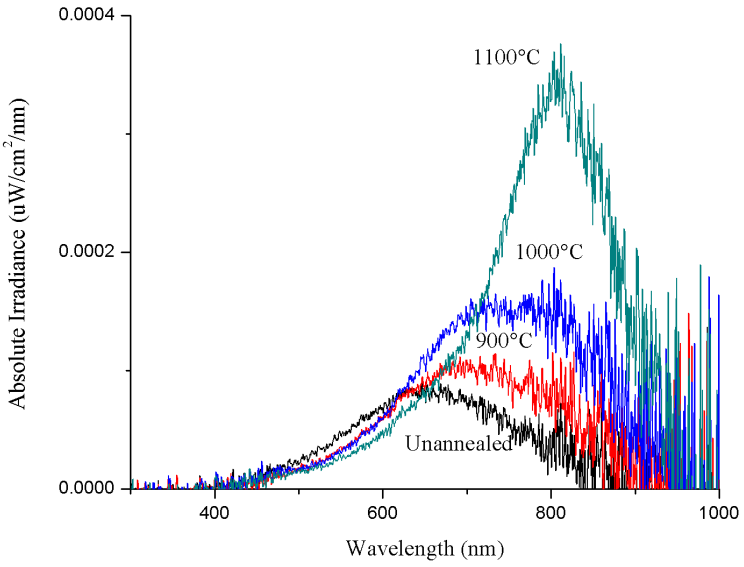

Figure 4.10: Photoluminescence from Cal-8. PL is likely due to Si-NCs formed after annealing at 1100˚C.

It can also be seen from the above PL spectra that Si-NCs grown with lower oxygen flows have a more red-shifted PL peak wavelength than films grown with higher oxygen flows. For example, comparing Cal-5 and Cal-7, which were grown with oxygen flows of 5.0 and 4.9 sccm, respectively, have more red-shifted PL than Cal-8, which was grown with an oxygen flow of 5.3 sccm. This is due to the increased incorporation of silicon into films grown with lower oxygen flows, thus creating larger Si-NCs and ultimately red-shifting the luminescence peak.

4.1.2 Spectroscopic Ellipsometry

Single-wavelength ellipsometry results showing the refractive index of calibration films have been shown in Figure 4.1, however more advanced ellipsometry was performed on the same films using a JA Woollam M2000UI variable-angle spectroscopic ellipsometer. A simple Cauchy model was used to model Cal-1, Cal-2, and Cal-3, however this model was insufficient to generate physical optical constants for Si-NC samples due to their increased absorption and more complex optical constants. A Tauc-Lorentz oscillator model [51] was instead used to determine optical constants for Si-NC samples.

Figure 4.11 shows the optical constants of Cal-1 for the as-deposited film, and after annealing at 900˚C, 1000˚C, and 1100˚C. A decrease in refractive index as well as extinction coefficient with high annealing temperatures indicates that the defect density in the film is decreasing as the film becomes pure SiO_2. This is confirmed by the characteristic SiO_2 refractive index after annealing at 1100˚C.

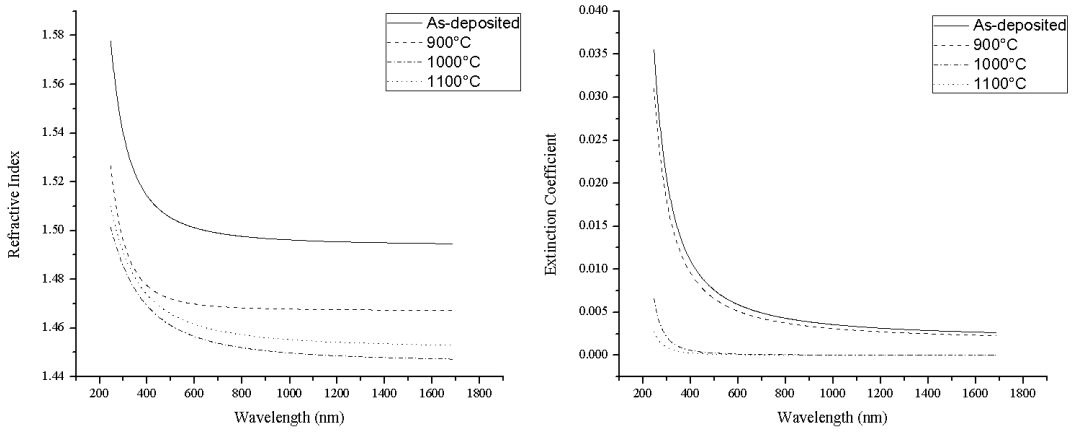

Figure 4.11: (Left) Refractive index of Cal-1 after annealing at different temperatures. A decrease in refractive index can be seen after high-temperature annealing; (Right) Extinction coefficient of Cal-1 after annealing at different temperatures. Since Cal-1 is essentially stoichiometric SiO_2, absorption decreases after high-temperature annealing.

The extinction coefficient of Cal-1 shows very small amounts of UV absorption after annealing at 1100˚C, which is again characteristic of SiO_2. This is in contrast to the optical constants of Cal-2, shown in Figure 4.12. This sample was slightly silicon-rich, and therefore shows an increase in absorption at higher annealing temperatures. The refractive index of Cal-2 still decreases with annealing temperature, however not as drastically as Cal-1.

The optical constants for Cal-3 are shown in Figure 4.13, where the refractive index begins to increase with annealing temperature. This could be due to vacancy defects in the film settling during the annealing process combined with the excess amounts of silicon in the film. The extinction coefficient again shows an increase in absorption after high-temperature annealing.

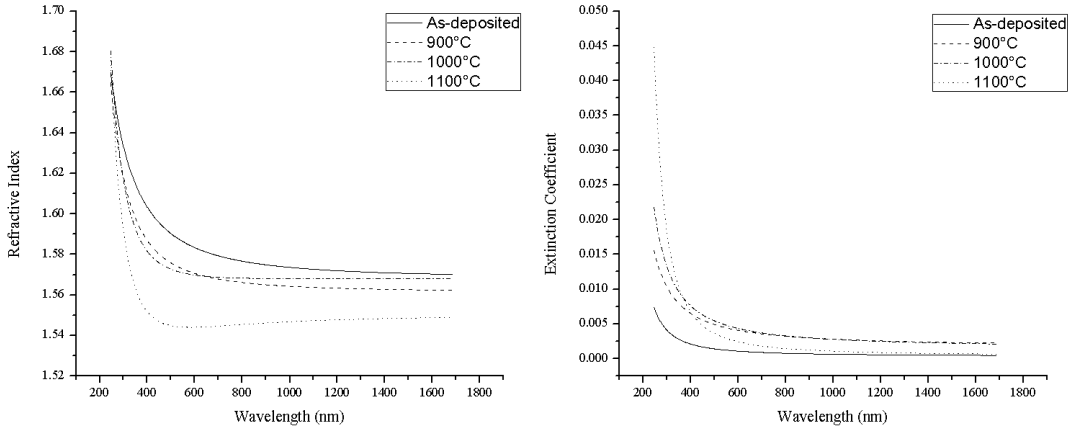

Figure 4.12: (Left) Refractive index of Cal-2 after annealing at different temperatures. A decrease in refractive index can be seen after high-temperature annealing; (Right) Extinction coefficient of Cal-2 after annealing at different temperatures. A slight increase in absorption is seen after high-temperature annealing.

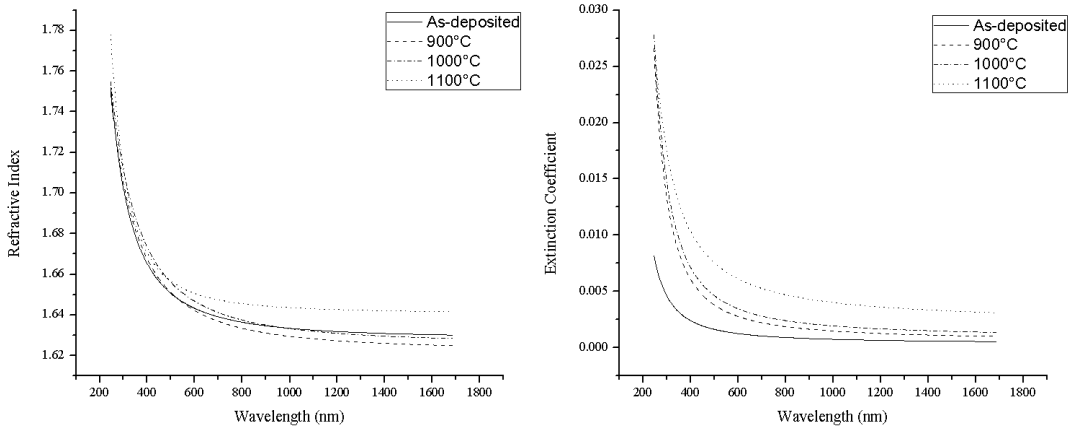

Figure 4.13: (Left) Refractive index of Cal-3 after annealing at different temperatures. An increase in refractive index can be seen after high-temperature annealing; (Right) Extinction coefficient of Cal-3 after annealing at different temperatures. An increase in absorption is seen after high-temperature annealing.

Figure 4.14 shows the optical constants of Cal-4, which had the lowest O_2 flow of all the calibration samples. The refractive index has a distinctly different wavelength dependence than the previous samples, corresponding more to the shape of silicon than silicon dioxide, as shown in

Appendix B. The refractive index still increased with high-temperature annealing, however annealing had little effect on the extinction coefficient of Cal-4. This indicates that the sample was perhaps too silicon-rich to form distinct nanocrystals separated by the silicon oxide matrix. In addition, the Cauchy model used on the previously mentioned calibration samples was unable to fit the ellipsometric data for Cal-4. Instead, a Tauc-Lorentz oscillator model was used to calculate optical constants. The Tauc-Lorentz oscillator model shows no absorption for wavelengths above approximately 600 nm, indicated by an extinction coefficient value of zero. This is likely more accurate than the Cauchy model, which shows a non-zero value for the extinction coefficient well into the near-infrared (NIR).

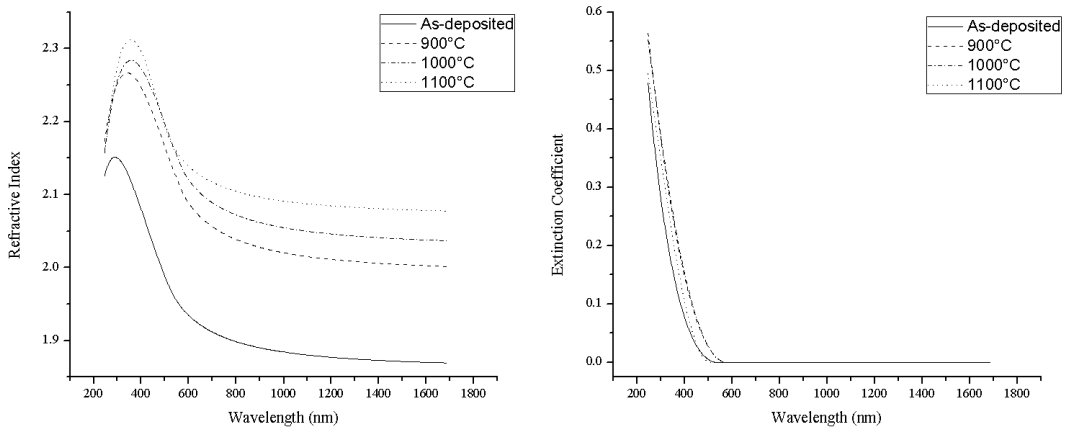

Figure 4.14: (Left) Refractive index of Cal-4 after annealing at different temperatures. An increase in refractive index can be seen after high-temperature annealing; (Right) Extinction coefficient of Cal-4 after annealing at different temperatures. No substantial increase in absorption is seen after high-temperature annealing.

Figure 4.15 shows optical constants for Cal-5, which contained Si-NCs according to the photoluminescence shown in Figure 4.8. Again, the refractive index increased after annealing, and

had a characteristic Si-NC shape of wavelength dependence [51]. The extinction coefficient shows strong absorption in the UV, with a slight increase after annealing above 900˚C.

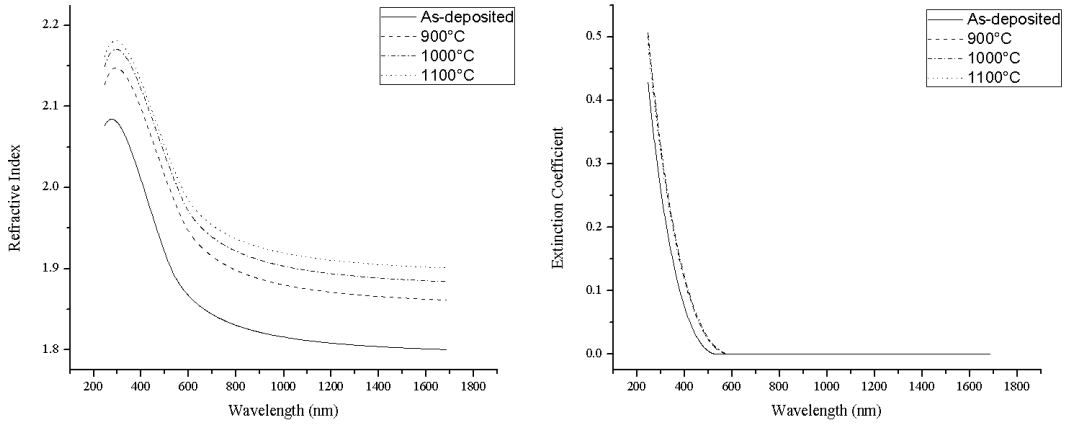

Figure 4.15: (Left) Refractive index of Cal-5 after annealing at different temperatures. An increase in refractive index can be seen after high-temperature annealing; (Right) Extinction coefficient of Cal-4 after annealing at different temperatures. No substantial increase in absorption is seen after high-temperature annealing.

Once a deposition recipe was obtained for successfully growing Si-NCs, the size of the Si-NCs, and therefore the peak PL wavelength could be tuned by slightly varying the silicon content of the film. Cal-7 and Cal-8 were attempts to blue-shift the peak PL wavelength from that of Cal-5, since the latter's PL was relatively far into the NIR. Figure 4.16 and Figure 4.17 show optical constants for Cal-7 and Cal-8, respectively. The refractive index for each sample shows a similar trend as Cal-5with regards to annealing temperature, however Cal-7 and more so Cal-8 show lower refractive indexes, indicating lower silicon content in each of these films.

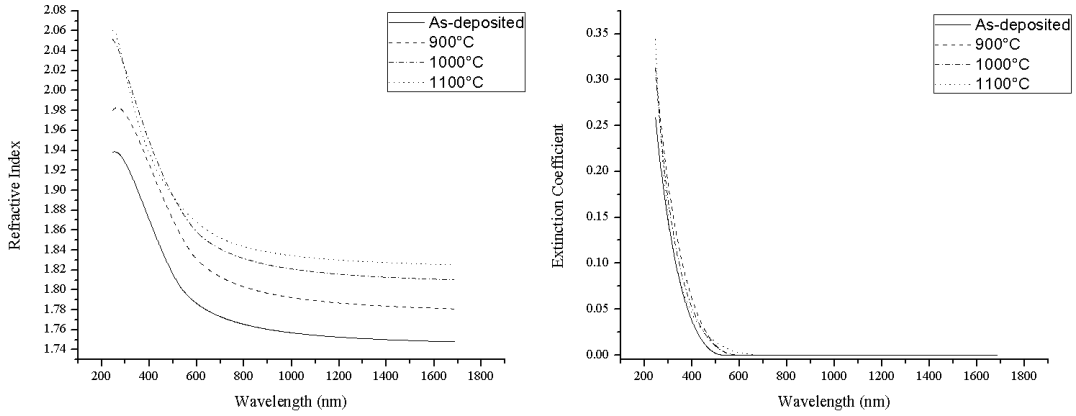

Figure 4.16: (Left) Refractive index of Cal-7 after annealing at different temperatures. An increase in refractive index can be seen after high-temperature annealing; (Right) Extinction coefficient of Cal-7 after annealing at different temperatures. No substantial increase in absorption is seen after high-temperature annealing.

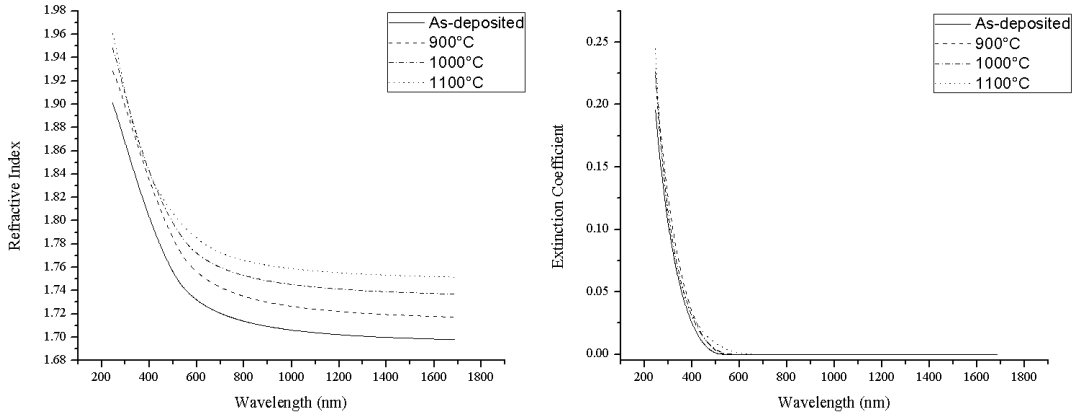

Figure 4.17: (Left) Refractive index of Cal-8 after annealing at different temperatures. An increase in refractive index can be seen after high-temperature annealing. (Right) Extinction coefficient of Cal-8 after annealing at different temperatures. No substantial increase in absorption is seen after high-temperature annealing.

The extinction coefficients from Si-NC samples give an indication of the cutoff energy, and therefore the optical band-gap of the material. Shown in Figure 4.18 is a log plot of the k values from Cal-5, 7 and 8, and it is evident that Cal-5 has the lowest-energy or longest-

wavelength bandgap, giving further evidence of larger Si-NCs. Samples Cal-7 and Cal-8 have comparable k values which are slightly lower until the cutoff energy. The conversion of Cal-7 and Cal-8 with Cal-5 around 550 nm could be a result of a different size distribution in the two samples.

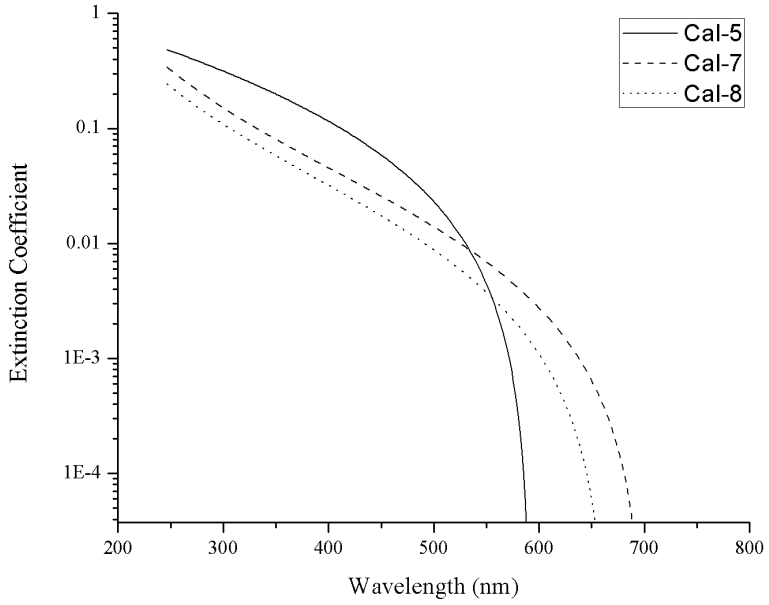

Figure 4.18: Log plot of the extinction coefficients from Si-NC samples after 1100˚C anneal.

4.1.3 Alternate Ellipsometric Models

The MSE values for the calibration ellipsometric models were generally low, and the optical constants output by the models were physical and sensible, however adding a gradient to the modeled material layer did improve the model's accuracy. This indicates that the Si:O ratio was not uniform within the films, but rather varied as a function of depth.

Figure 4.19 shows the graded refractive index values for Cal-5 at different annealing temperatures. The lower curve at each temperature corresponds to the top of the film, while the higher values correspond to the bottom of the film close to the substrate. This indicates that the film is more silicon-rich near the substrate, and gradually becomes less silicon-rich near the surface. As seen in the inset of Figure 4.19, the gradation decreases at higher annealing temperatures, indicating that annealing increases the uniformity of the film. This could be due to non-uniform defects in the film that persist until annealing temperatures reach approximately 1000˚C.

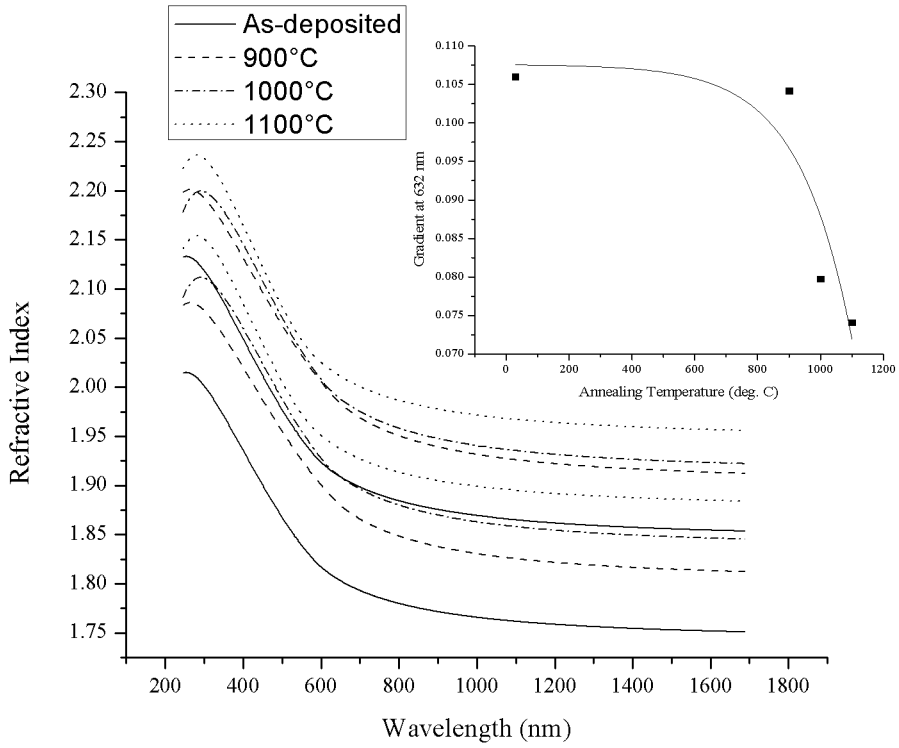

Figure 4.19: Graded refractive index shown for different annealing temperatures for Cal-5. The inset shows the difference between top and bottom n values at 632 nm, following an exponential curve.

4.2 Deposition on Fused Silica

Once deposition parameters corresponding to repeatable Si-NC formation had been determined, similar films were grown on fused silica substrates. Specifically, 0.5 mm thick UV fused silica Spectrosil® 2000 UV coverslips (CFS-2525) from UQG Optics were used as substrates for transparent samples. The fused silica substrates were cleaned using acetone and methanol prior to deposition. The films were deposited on both silicon and fused silica simultaneously to achieve identical layers on both substrates. Figure 4.20 and Figure 4.21 show PL from two such Si-NC films, where the effect of substrate on PL intensity is evident. The films grown on fused silica have approximately twice the PL intensity as the same films grown on silicon.

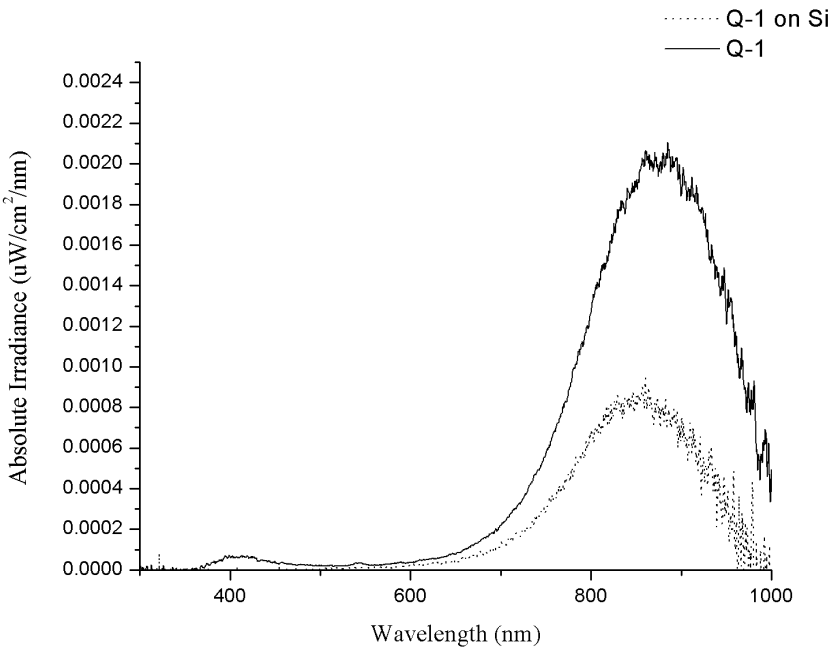

Figure 4.20: A comparison of a Si-NC film on silicon with the same film on fused silica.

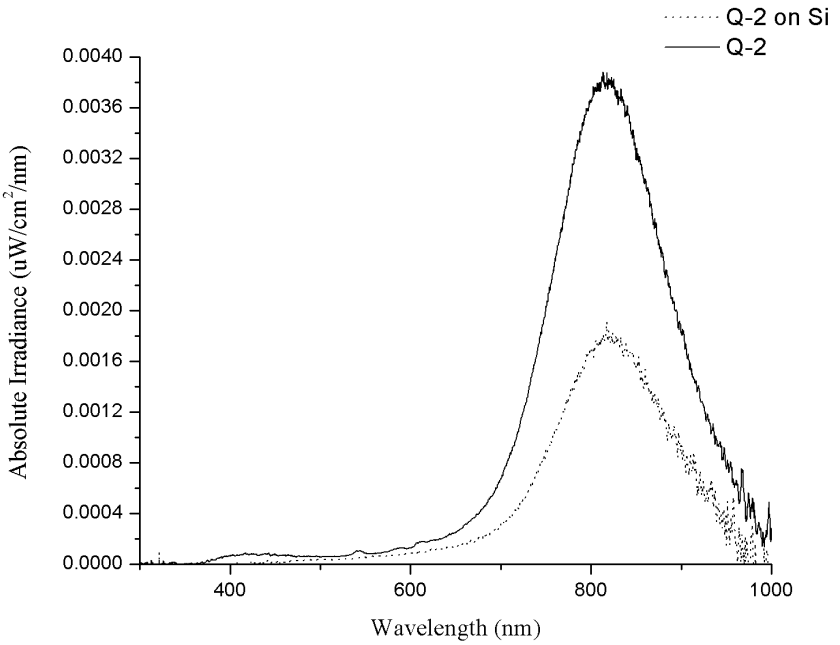

Figure 4.21: A comparison of a Si-NC film on silicon with the same film on fused silica.

The increase in PL intensity from the same film on fused silica as opposed to silicon could be due to several factors. Foremost, a silicon substrate has stronger absorption than a fused silica substrate, which is essentially transparent at the emission wavelength of the Si-NCs. This absorption would largely result in non-radiative recombination and therefore optical loss within the silicon substrate, due to the indirect nature of silicon's energy band. The index of refraction of the substrate would also affect the amount of reflection that occurs at the film-substrate interface. A lower index substrate, such as fused silica, would create more reflection at the film-substrate interface than a higher index substrate, such as silicon, following the Fresnel equation for reflection coefficient. This increased reflectance could account for more light being emitted from the sample.

4.3 Effect of Varying the Film Thickness

The calibration samples discussed in Section 4.1 were deposited at a standard thickness of approximately 120 nm. An experiment was done to see the effect of varying the film thickness on photoluminescence and absorption. A total of nine samples were deposited at thicknesses increasing in increments of approximately 80 nm. At one point during the experiment, the main chamber on the ECR system was contaminated due to a leak, resulting in several of the samples being compromised.

During all depositions, the partial pressure of each gas was maintained as constant as possible, in order to have constant stoichiometry between films. The base pressure of the system at the time of this experiment was on the order of 10^{-7} mTorr. The thermocouple attached to the stage heater was malfunctioning, so a test deposition was done to conclude that setting the heater power to 45% during deposition maintained an approximate temperature of 120˚C after stabilization. The deposition time was the only parameter varied in order to achieve different film thicknesses. All films were deposited on silicon and fused silica simultaneously, and then annealed in a quartz tube furnace at 900˚C, 1000˚C, 1100˚C, and 1135˚C in flowing H_2 (5%) N_2 (95%). Table 4.2 shows the gas flows and partial pressures of all films in this experiment, and all other deposition parameters were the same as discussed in Section 4.1.

Table 4.2: Deposition parameters for films of varying thicknesses, including gas flows (sccm) and partial pressures (PP) (mTorr). Depositions in *italics* were contaminated by a leak in the system. The error for all gas flow values is ±2.5 sccm.

$Ar + SiH_4$ Flow (sccm)	$Ar + SiH_4$ PP (mTorr)	$Ar + O_2$ Flow (sccm)	$Ar + O_2$ PP (mTorr)	Ar Flow (sccm)	Ar PP (mTorr)
2.50	0.22	5.40	0.47	18.9	1.41

All uncontaminated films exhibited evidence of Si-NCs, characterized through PL, VASE, and finally two samples were viewed under a Transmission Electron Microscope (TEM) to confirm the presence of crystalline nanoparticles. Films that were contaminated were omitted from the results section, including Th-5, Th-6 which exhibited no signs of Si-NCs, and Th-4 and Th-7, which had lower PL intensity, presumably due to poor film quality.

4.3.1 Spectroscopic Ellipsometry

Films were characterized using the same ellipsometric method as discussed in Section 4.1.2. The VASE measurements were generally fit by a Tauc-Lorentz oscillator model, however some anomalies were seen when analyzing using this model.

Figure 4.22 shows the optical constants for Th-3, Th-8, and Th-9 after they had been annealed at 1135˚C. It can be seen that the two thicker films, Th-8 and Th-9, have slightly higher refractive indexes, indicating that they are slightly more silicon-rich. The thicker films also show slightly higher levels of absorption, and Th-8 has the lowest cutoff energy or higher cutoff wavelength, indicating larger Si-NCs.

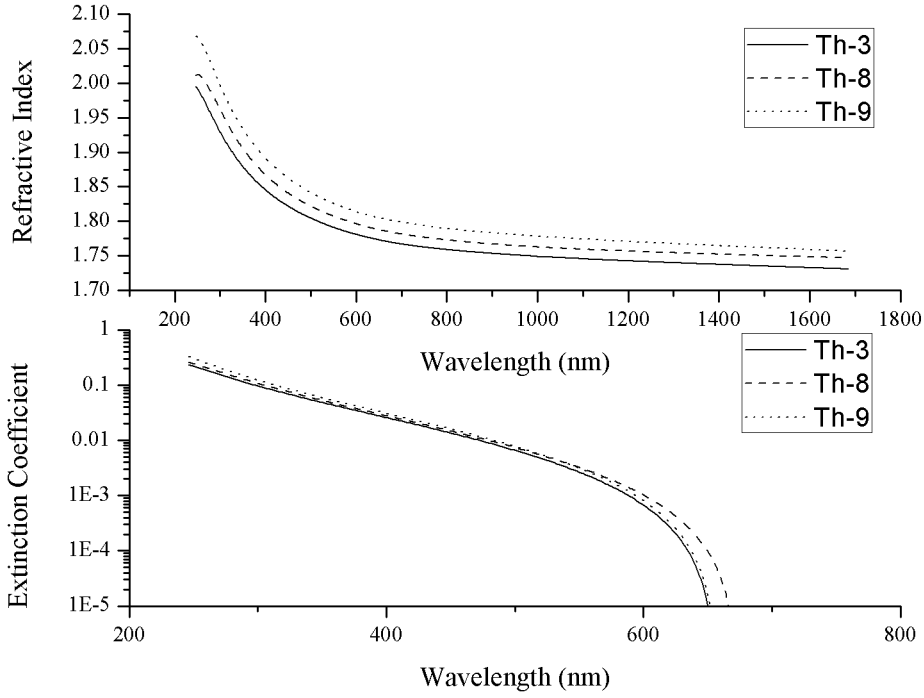

Figure 4.22: Optical constants of Th-3, Th-8, and Th-9 after annealing at 1135˚C.

Figure 4.23 shows the optical constants for the thinnest films, Th-1 and Th-2 after they were annealed at 1135˚C. The wavelength dependence of the refractive indexes was somewhat different for each film, with a slightly lower tail in the IR. Again the thicker film, Th-2, had a higher refractive index, indicating higher silicon content.

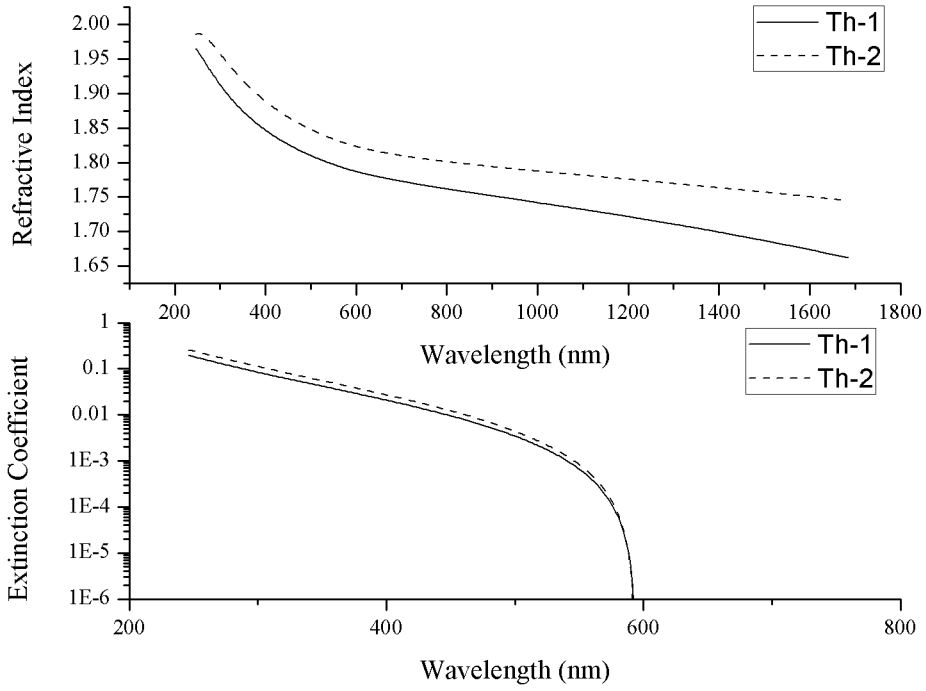

Figure 4.23: Optical constants of Th-1, and Th-2 after annealing at 1135˚C.

The extinction coefficients of Th-1 and Th-2 show drastically lower cutoff energies or longer wavelengths than the thicker films, below 600 nm. The initial indication of the lower cutoff energies is that the thinner films contain smaller nanocrystals; however, it may be that the thickness of the film affects the effective bandgap of the material.

The relationship between film thickness and deposition time can be seen in Figure 4.24, which shows very good linear correlation. This negates the possibility of the deposition rate changing as films grow thicker with certainty until 0.5μm of film thickness. It is possible that when growing very thick films, deposition rates will begin to change due to the top of the film

growing closer to the dispersion ring and plasma source. Significant thicknesses would be needed to see such effects, however, perhaps on the order of millimeters.

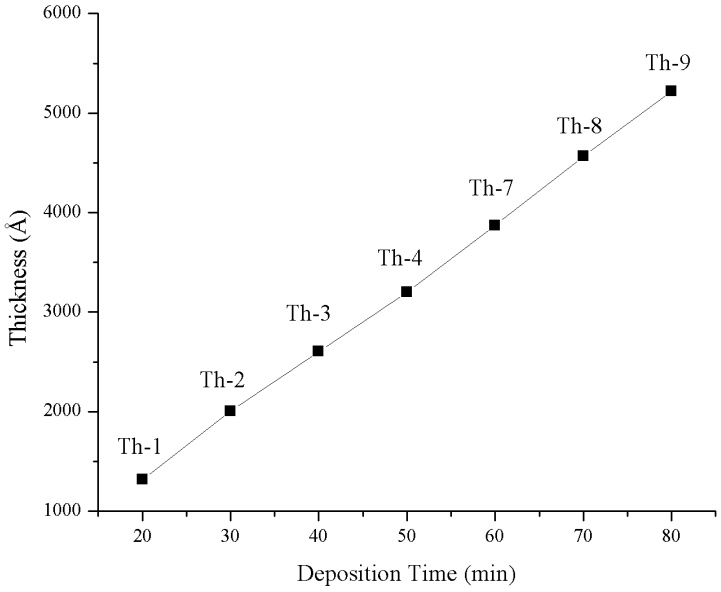

Figure 4.24: Film thickness as a function of deposition time. Errors in the thickness are contained within the data points.

A decrease in thickness was seen after high-temperature annealing, as shown in Figure 4.25. This is likely due to vacancy defects being removed during annealing, and therefore a relaxation or settling of the film. This relaxation causes the amorphous material to compress and therefore reduces the overall thickness of the film and causes an increase in the refractive index due to the densification of silicon within the film. This effect was also seen in calibration films.

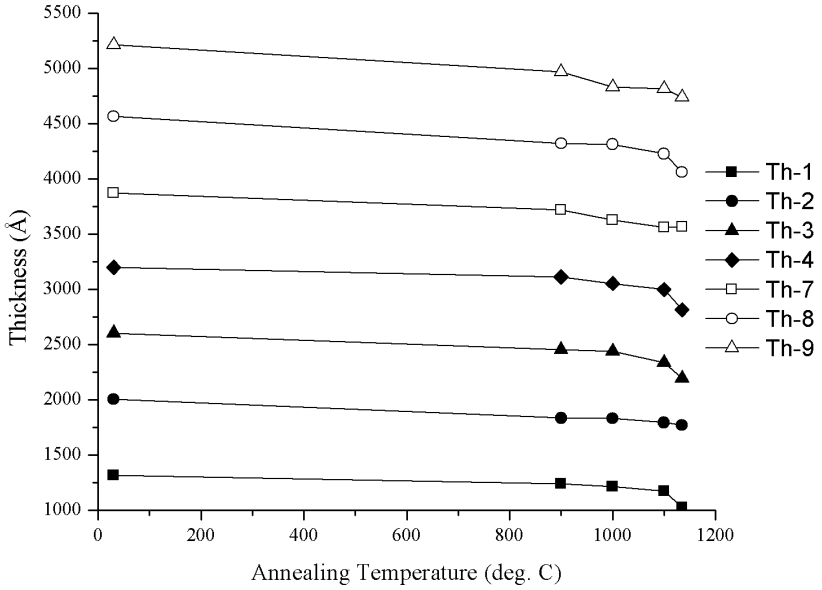

Figure 4.25: Film thickness as a function of annealing temperature.

This section showed optical constants of films after 1135˚C annealing, when Si-NCs were present. For detailed information on the optical constants for all films in this experimental set, please refer to Appendix C.

4.3.2 Photoluminescence Spectra

Photoluminescence was measured under identical conditions as discussed in Section 4.1.1, and is shown in Figure 4.26 for uncontaminated films deposited on fused silica. As with previously discussed calibration samples, and shown in Figure 4.27, significant PL was not seen until annealing at 1000˚C or higher, showing that Si-NCs do not form until high-temperature processing. Annealing was done at 1200˚C to determine whether PL intensity continued to increase, however a slight drop in intensity was observed. Upon removing the samples from the

tube furnace after the 1200˚C anneal, a visible contamination or re-crystallization was seen in the form of a white coating on the films. This had been observed in other tube furnaces after 1200˚C processing, and is thought to be due to contaminants on the surface of the quartz tube that are released at this temperature. It is probable that annealing at 1200˚C will indeed form Si-NCs and perhaps yield higher PL intensity than lower temperatures, however contamination would need to be mitigated in order to do so.

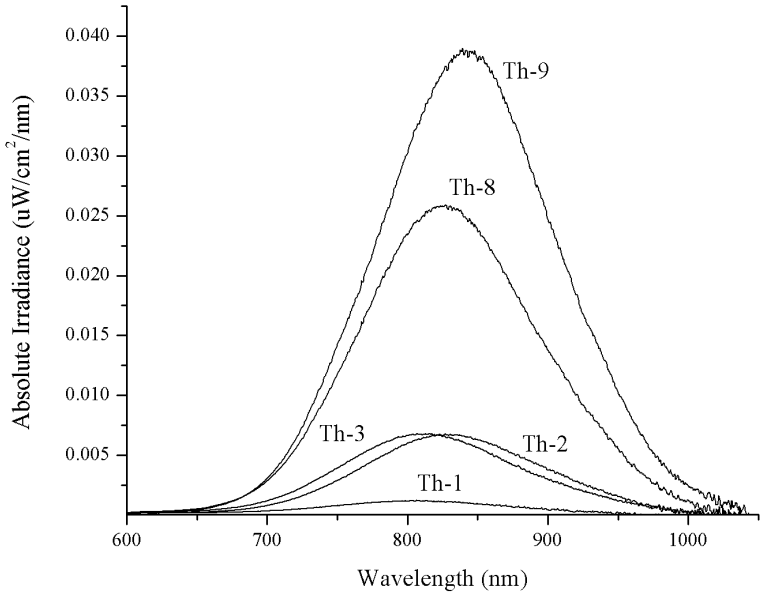

Figure 4.26: PL spectra of Si-NC films of varying thicknesses deposited on fused silica. PL intensity increased as a function of thickness, and a slight red-shift was seen in thicker films.

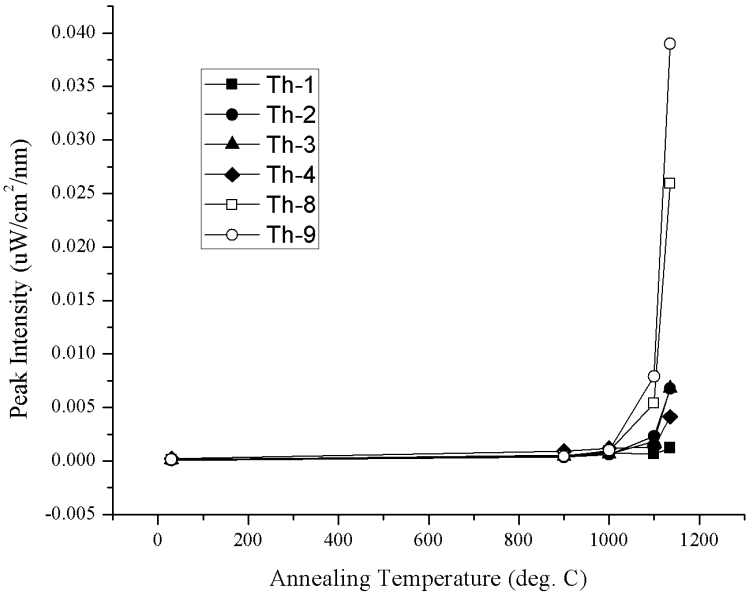

Figure 4.27: PL intensity as a function annealing temperature for films of different thicknesses.

It is clear from Figure 4.28 that PL intensity increases in thicker films, likely due to the larger number of Si-NCs that are present. A slight red-shift is apparent as film thickness increases, indicating that thicker films incorporate more silicon, or less oxygen, and therefore have larger Si-NCs. This is consistent with the higher refractive indexes of thicker films, shown in Section 4.3.1. A red shift is also seen with increasing annealing temperatures, as shown in Figure 4.29, with the peak wavelengths converging after annealing at 1000˚C. Most films show a drastic red shift after 900˚C, due to vacancy defects being removed and excess silicon clustering together. The peak wavelength continues to shift at higher temperatures, simply due to Si-NCs forming with larger diameters. A few of the films required annealing at 1000˚C to exhibit PL from silicon nanoclusters, indicating that these films either have a larger density of vacancies, or are less

silicon rich. These films therefore needed higher annealing temperatures to form nanoclusters and to remove vacancy-related luminescence.

In addition, films deposited on fused silica had approximately twice the PL intensity as identical films deposited on silicon, for reasons discussed in Section 4.2.

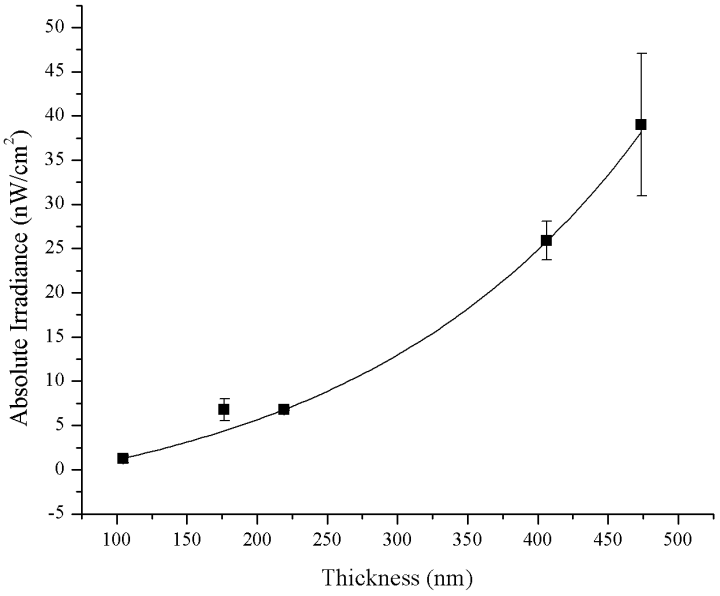

Figure 4.28: PL intensity as a function of film thickness for films containing Si-NCs.

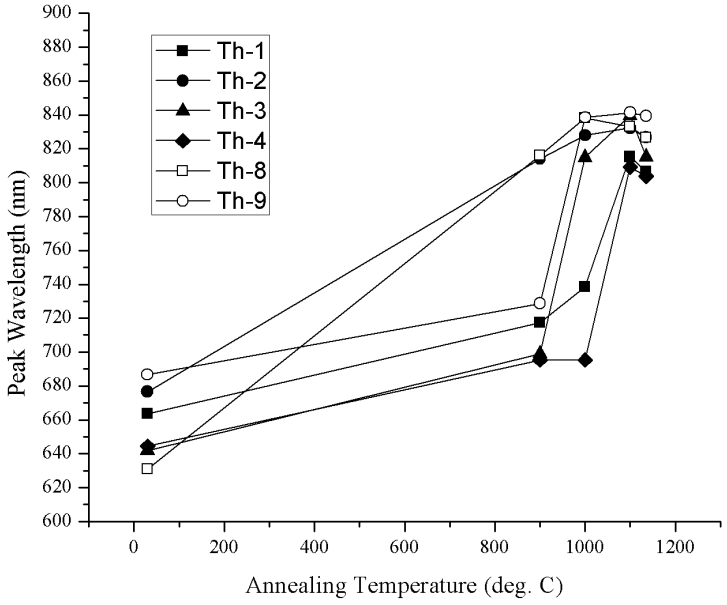

Figure 4.29: Peak PL wavelength as a function of annealing temperature for films of different thicknesses.

4.3.3 Transmission Electron Microscopy

High-resolution Transmission Electron Microscopy (HR-TEM) was used to view Si-NCs, specifically the FEI Titan 80-300 Cryo at the Canadian Centre for Electron Microscopy. Films Th-2 and Th-9 were viewed from a cross-sectional perspective, showing the distribution of Si-NCs throughout the film. Dark-field (DF) imaging was used to highlight the crystalline regions of the film in some of the images.

Figure 4.30 shows a HR-TEM image of Si-NCs in Th-2. The Si-NCs have an average size of about 4 nm, and can be clearly seen as circular regions of ordered material amidst amorphous SiO_2. Circles have been drawn to clearly identify the nanocrystalline regions.

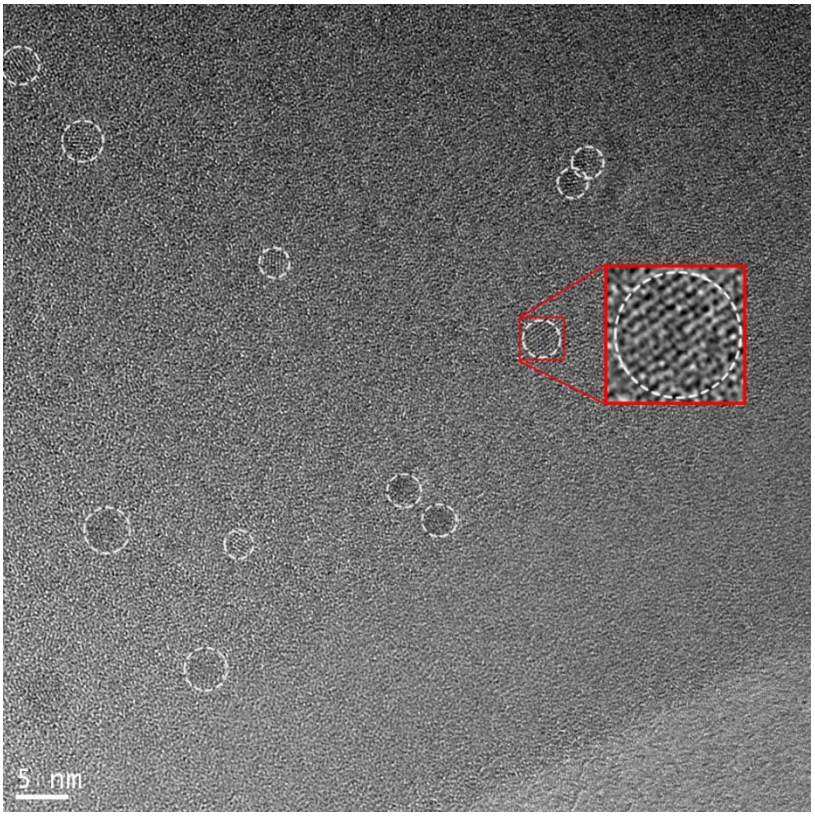

Figure 4.30: HR-TEM image of Si-NCs in Th-2 showing crystalline regions embedded in an amorphous material.

Since the images are two-dimensional cross-sections, only those Si-NCs whose crystallographic orientation is perpendicular to the field of view will be visible as crystalline. Si-NCs with orientations that are not aligned this way will either appear as dark spots, or not at all. Considering that the orientation of the Si-NCs is random within the film, the readily apparent number of Si-NCs in the HR-TEM images is relatively high when comparing to other TEM images of PECVD Si-NCs in the literature [33], [52]. Looking at the DF-TEM images in Figure 4.31 further shows the density and distribution of the Si-NCs throughout the film. The left image in Figure 4.31 shows a high-magnification view of the Si-NCs, a few of which have been circled to indicate the nanocrystal's diameter. The right image shows the entire film with Si-NCs

scattered throughout. The bright region at the top left of this image is the substrate, and the bottom right is the edge of the film. It seems from this image that there is a higher density of large Si-NCs near the surface of the film, and less near the substrate. This could mean that the nanocrystals form more quickly near the surface due to a temperature gradient during the annealing process and therefore have more time to grow in this region.

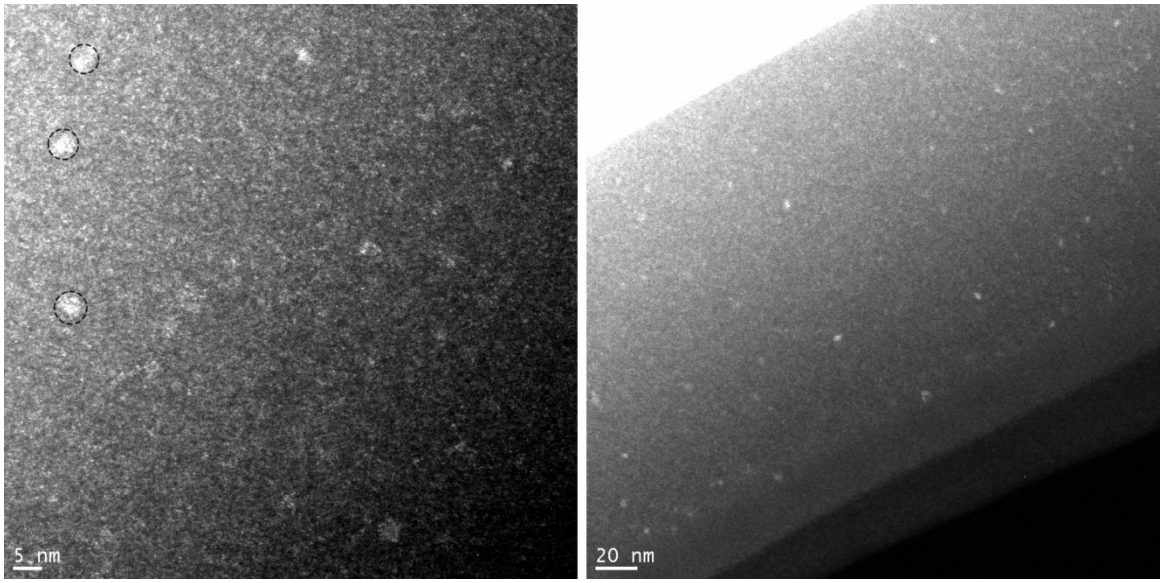

Figure 4.31: Dark field HR-TEM image of Si-NCs showing NC diameter (left), and distribution throughout the film (right) for Th-2.

Figure 4.32 shows an HR-TEM image of Si-NCs from Th-9, some of which have again been circled for clear identification. The nanocrystal diameter is approximately the same as for Th-2, though the image is not quite as clear as for the previous sample. This is due to the sample not being ion-milled thin enough during TEM preparation. Figure 4.33 shows two DF TEM images of Th-9, showing a large density of Si-NCs throughout the film. Again it seems that larger

nanocrystals tend to form closer to the surface of the film, which is at the bottom left of the images.

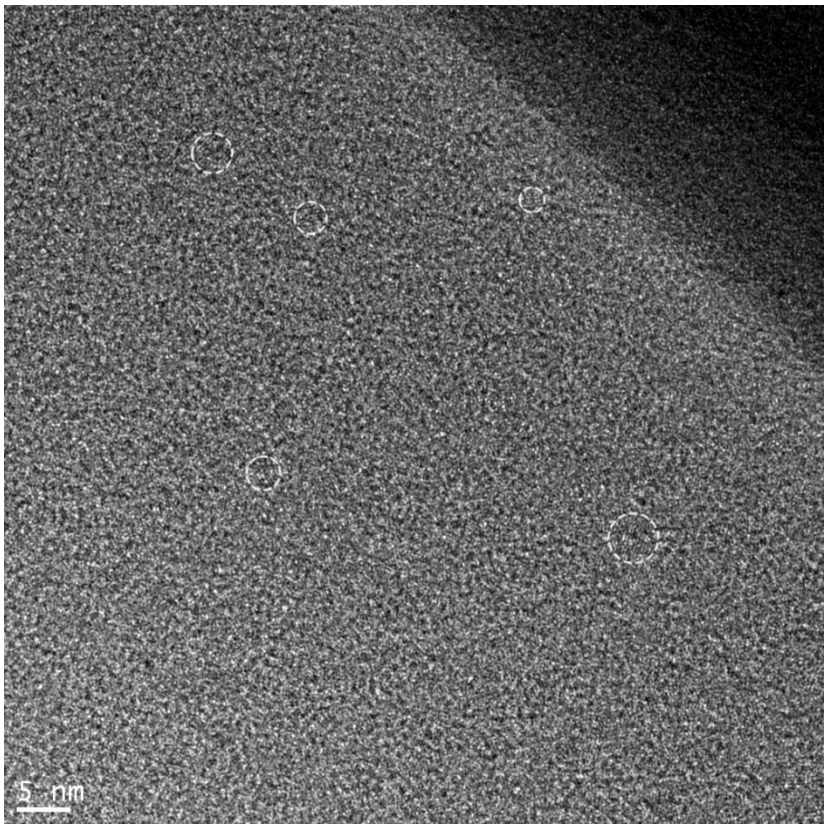

Figure 4.32: HR-TEM image of Si-NCs in Th-9 showing crystalline regions embedded in an amorphous material.

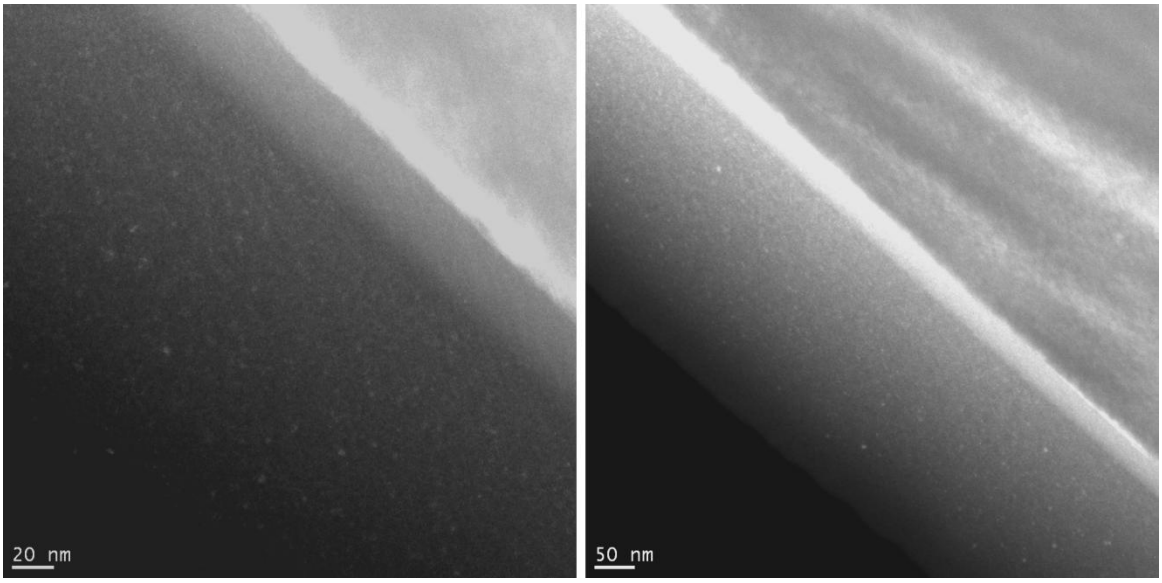

Figure 4.33: Dark field HR-TEM images of Si-NCs showing the distribution throughout the film for Th-9.

It was observed in Th-9 and is shown in Figure 4.34 that a 30 nm oxide layer formed between the surface of the silicon substrate and the film. This oxide is void of Si-NCs, however is too thick to be a native oxide. Therefore, it either formed during deposition within the PECVD chamber, or existed on the substrate prior to deposition through means other than native oxide formation, such as a thermally grown oxide.

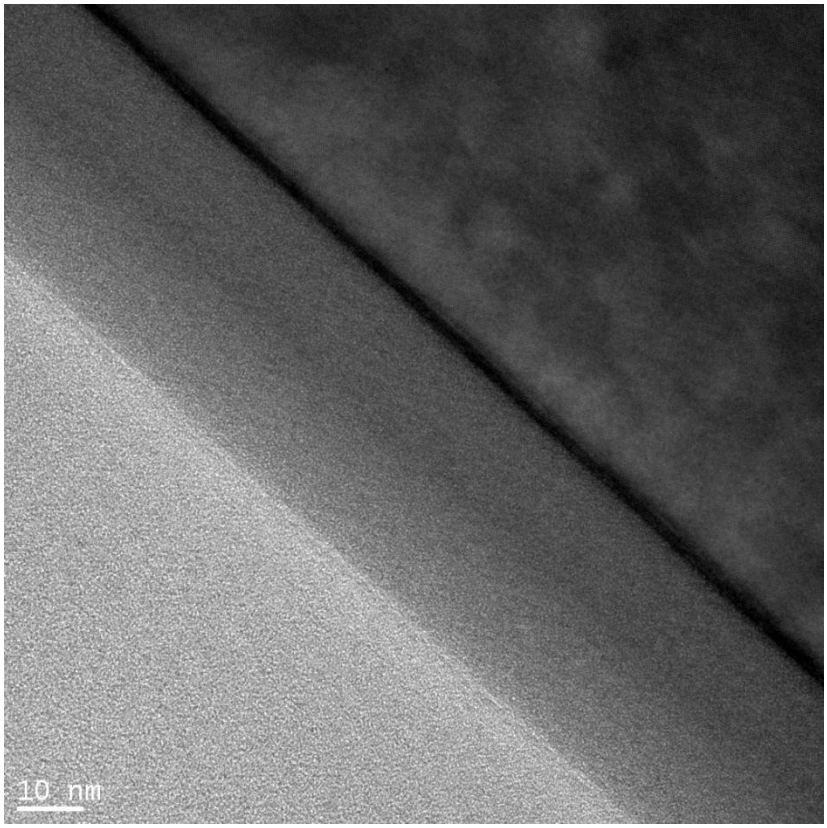

Figure 4.34: HR-TEM image of a 30 nm oxide layer between the film and the substrate of Th-9.

To approximate the volumetric density of Si-NCs within the film, the HR-TEM and DF-TEM images from Th-2 were use to determine an average cross-sectional density of 1536 nanocrystals per square micron. This cross-section was assumed to repeat through the film in 10 nm intervals, giving a volumetric density on the order of magnitude of 10^5 nanocrystals per cubic micron. A similar calculation was not done with the lower-quality images of sample Th-9 since these images may not have reflected the actual Si-NC density throughout the film.

4.3.4 Transmission and Absorption Spectra

Transmission spectra were measured using the JA Woollam M2000UI variable-angle spectroscopic ellipsometer set in transmission mode. The ellipsometer arms are rotated to 90˚ from the normal, directly aligning the light and the detector. The sample was mounted in the beam path and the transmission was measured against a baseline measurement performed with no sample present. The results are shown in Figure 4.35 for all films of varying thickness. It is clear that as the films increase in thickness, interference effects begin to emerge. For the thinnest film, Th-1, which is approximately 100 nm thick, the interference effects are negligible since the film thickness is not comparable to the wavelength of light passing through. The thicker films, which range from approximately 180 nm to 500 nm do create interference effects due to multiple reflections of light at the interface between the film and the substrate, and the film and the environment. In addition, the overall transmission decreases as film thickness increases. This is due to the increased number of Si-NCs and therefore absorption centres in thicker films.

Using the extinction coefficient data obtained in section 4.3.1, the absorption coefficient could be calculated, giving information on the depth of light penetration within various films. The calculation uses the following equation:

$$a = \frac{4\pi k}{\lambda}, \tag{4.1}$$

where λ is the wavelength, and k is the extinction coefficient. The absorption coefficient for Th-1 as deposited and after annealing at 1135˚C is shown in Figure 4.36. A drastic and characteristic increase in absorption can be seen after annealing, coinciding with the formation of

Si-NCs. The absorption cutoff is also given by the absorption coefficient, and in the case of Th-1 is approximately 590 nm, though absorption past 500 nm is fairly low and perhaps insignificant.

Shown in Figure 4.37 are the absorption coefficients of all films of varying thicknesses after annealing at 1135˚C and Si-NC formation. It is apparent that there are higher levels of absorption for thicker films, and therefore longer cutoff wavelengths for thicker films. The increased absorption levels in thicker films are due to a larger number of Si-NC absorption centres, and the increased cutoff wavelengths could be due to larger Si-NCs that exist in thicker films.

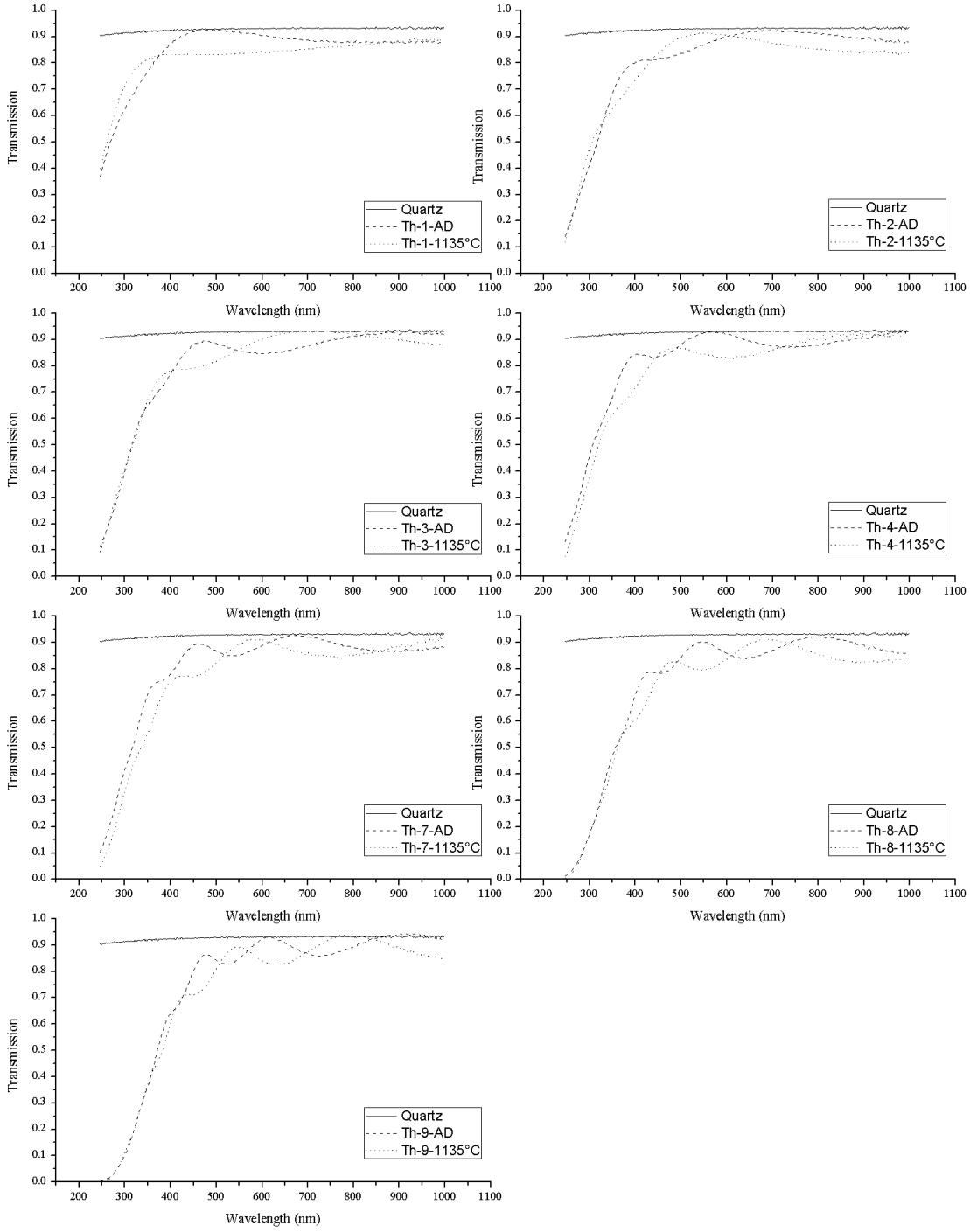

Figure 4.35: Transmission spectra for as-deposited SRSO films of increasing thickness. Films were deposited on fused-silica, and shown as-deposited (AD) or after being annealed at 1135°C.

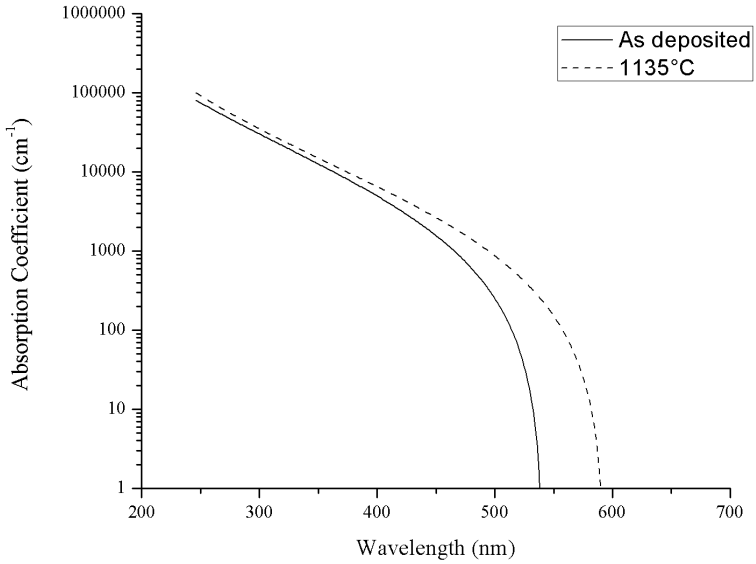

Figure 4.36: Absorption coefficient for Th-1 as-deposited and after annealing at 1135˚C.

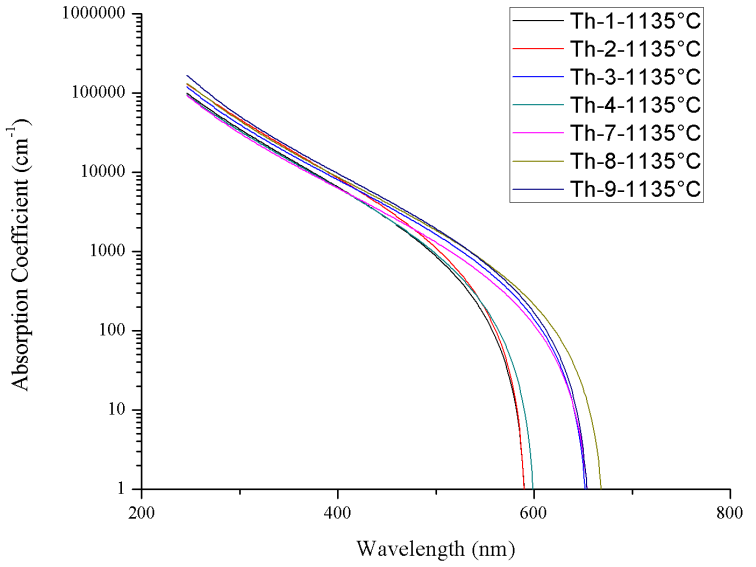

Figure 4.37: Absorption coefficient for films of varying thicknesses containing Si-NCs.

Using the extinction coefficient, the depth at which a certain photon flux reaches a specific attenuation can be determined. When considering a spectral engineering layer for single-junction silicon cells, photons below 500 nm would be targeted for absorption, since those are approximately half the silicon bandgap. One of these or higher-energy photons could therefore be converted into two low-energy yet useful photons for a silicon cell thus increasing the cell performance at the given wavelength. To determine the optimal film thickness for a conversion layer, it is useful to know the transmitted power intensity, I, as a function of penetration depth, x. This can be calculated using the Beer-Lambert law:

$$I = e^{-ax}, \tag{4.2}$$

where a is the absorption coefficient at a given wavelength. The power intensity is shown as a function of photon penetration depth for 500 nm photons in Figure 4.38 for as-deposited Th-9, as well as Th-9 annealed at 1000˚C and 1135˚C.

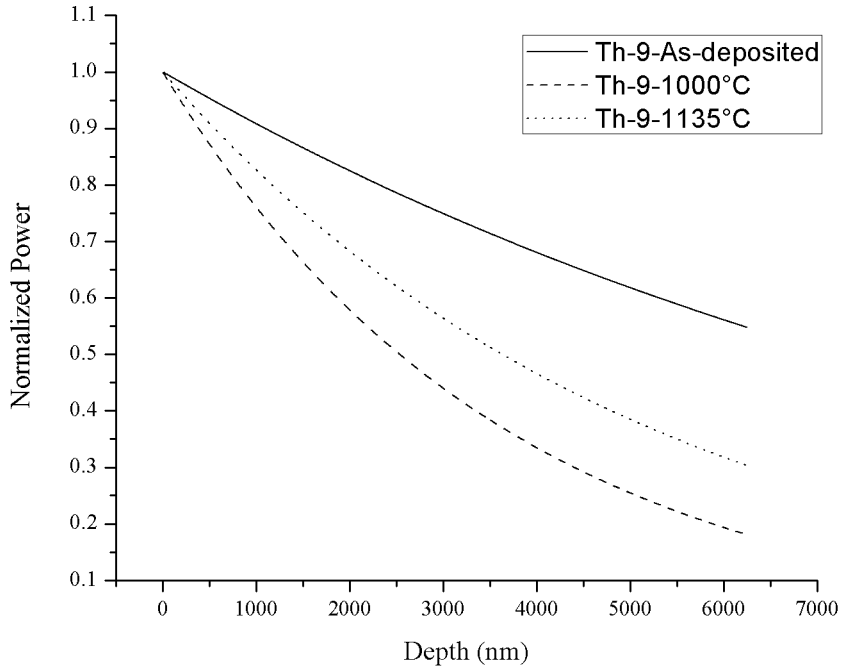

Figure 4.38: Power intensity as a function of photon penetration depth for 500 nm photons through Th-9, following the Beer-Lambert Law.

The as-deposited film shows the slowest decline in power intensity, due to the low absorption compared to films with Si-NCs. The film that was annealed at 1000˚C shows the strongest attenuation, perhaps because there are nanoclusters of silicon that have formed, however large defect densities still remain and therefore hinder the transmission of light. Figure 4.38 shows that for a Si-NC film of with the properties of Th-9 after annealing at 1135˚C, a photon flux composed of 500 nm photons will reach 50% power attenuation at approximately 4 microns.

4.4 Absolute PL Quantum Efficiency of Silicon Nanocrystals

The photoluminescence internal and external quantum efficiencies of various Si-NC samples were measured using the method described in Chapter 3. The samples deposited on fused silica, mentioned in Section 4.2, were the first samples measured. These samples were difficult to measure due to a high signal-to-noise ratio, however measurements were finally completed.

First, the absorption of each sample was measured by comparing the laser intensity with and without samples present inside the integrating sphere. The difference between the laser intensity with and without a sample present was taken to be the absorption at the laser wavelength of 405 nm. Figure 4.39 shows the laser intensity measured with no sample, with a blank piece of fused silica, and both samples mounted at the centre of the sphere. Reflection off each sample was directed back into the sphere and therefore would not be considered absorption. Peaks in the laser line are due to the low-resolution of the calibration, and are not significant features.

After correcting for the sphere response and converting into a photon flux, the laser intensity was integrated from 395 nm to 410 nm to get the total number of photons from the laser under each condition. Table 4.3 shows the measurement results for each condition.

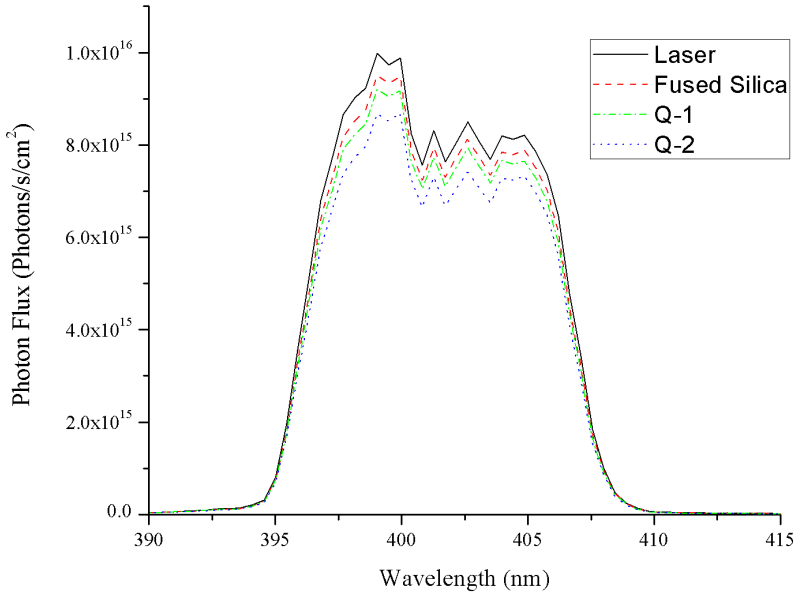

Figure 4.39: Laser line measured with and without Si-NC samples present within the integrating sphere. The difference between the laser intensity with and without samples was taken to be the absorption. Peaks in the laser line are simply due to the low-resolution calibration and are not significant features.

Table 4.3: Absorption measurements at 405 nm of fused silica and Si-NC samples Q-1 and Q-2.

Measurement	Integrated Photon Flux (Photons/s/cm^2)	Total Absorption (Photons/s/cm^2)	Si-NC Absorption (Photons/s/cm^2)
Laser	2.07×10^{17}		
Fused Silica	1.97×10^{17}	1.03×10^{16} (5.23%)	
Q-1	1.91×10^{17}	1.63×10^{16} (7.87%)	6.01×10^{15} (3.06%)
Q-2	1.80×10^{17}	2.69×10^{16} (13.01%)	1.67×10^{16} (8.46%)

It is important to note the difference between the total absorption and the Si-NC absorption. The total absorption is the absorption of the Si-NCs as well as the fused silica substrate, calculated by taking the difference between the laser line with no sample present, and with a Si-NC on fused silica sample present. The Si-NC absorption represents the absorption of the NC only, calculated by taking the difference between the laser line with a blank piece of fused

silica present, and with a Si-NC sample on fused silica present. The total absorption was used for calculating the IQE of the converter, while the Si-NC absorption was used to calculate the IQE of the Si-NC.

Figure 4.40 shows the photon flux corresponding to the PL curve for each of the Si-NC samples on fused silica measured inside the integrating sphere. These measurements were taken with the long integration time of at least 30 seconds, and then manually smoothed, corrected using the integrating sphere response and converted into a photon flux. The large amounts of noise in the NIR are due to the calibration curve of the LS-1-CAL lamp used for CCD calibration. Table 4.4 shows the photon flux of each luminescent sample integrated from 500 nm to 1000 nm, as well as the external quantum efficiency of each Si-NC sample, and internal quantum efficiency of the entire converter and the Si-NCs.

Table 4.4: Integrated photon flux and calculated quantum efficiencies of Si-NC samples Q-1 and Q-2.

Sample	Integrated photon flux	EQE	IQE of Converter	IQE of Si-NC
Q-1	1.11×10^{14}	0.054%	0.68%	1.84%
Q-2	1.71×10^{14}	0.083%	0.64%	1.03%

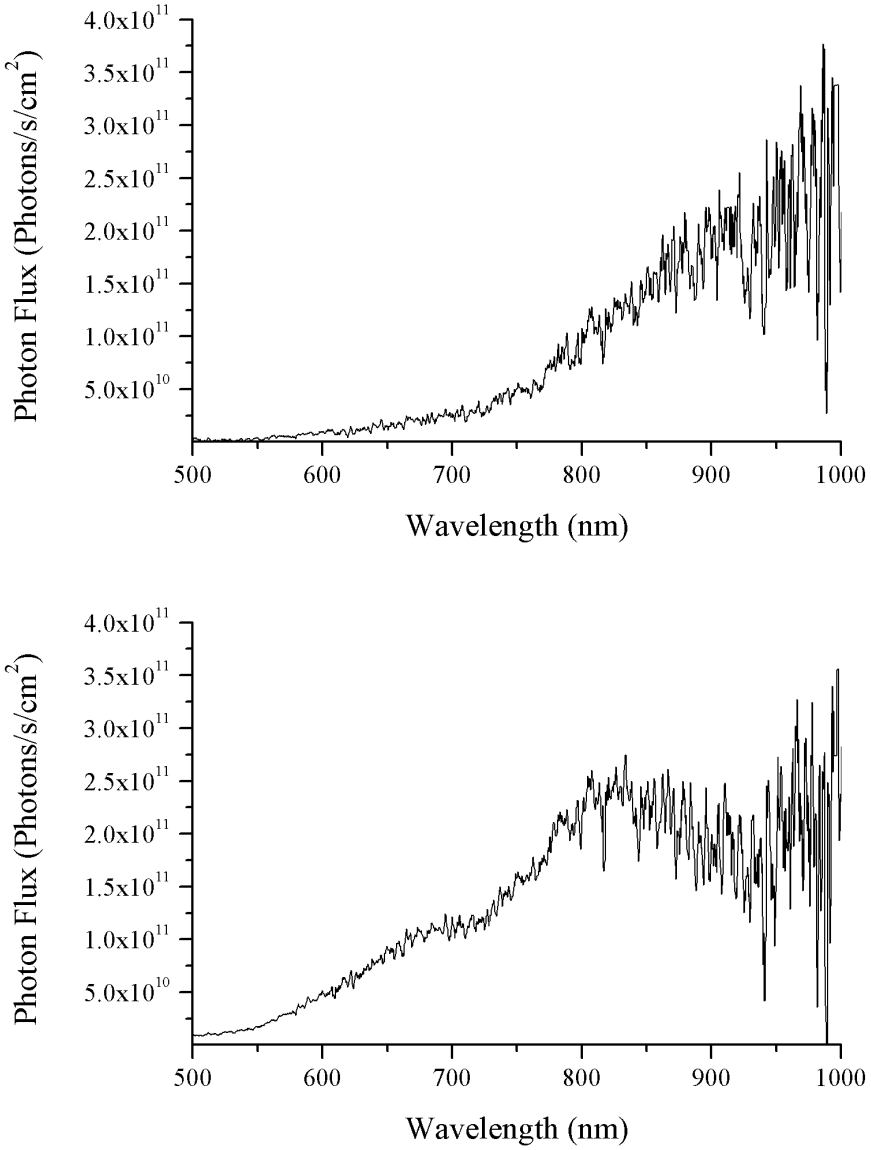

Figure 4.40: Photon flux for luminescent Si-NC samples Q-1 and Q-2 measured inside an integrating sphere.

The same measurement was completed for Si-NC samples of increasing film thickness. Figure 4.41 shows the absorption measurements for all samples, with a clear increase in absorption correlating with increasing sample thickness. The laser line looks smoother than in

Figure 4.39 due to a second CCD calibration that was done with higher signal averaging levels. The peak seen at 400 nm is due to the calibration curve, and therefore should not be taken as a significant feature.

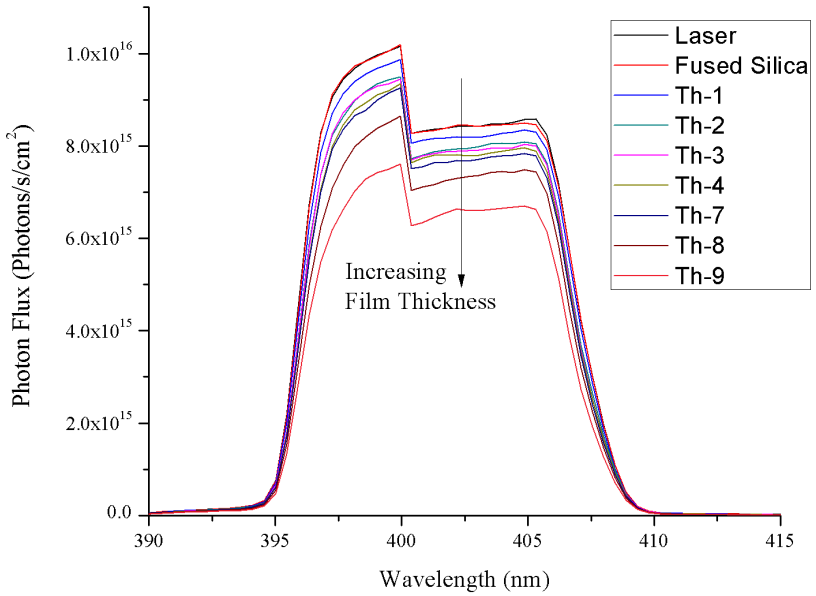

Figure 4.41: Laser line measured with and without Si-NC samples present within the integrating sphere. The difference between the laser intensity with and without samples was taken to be the absorption. The peak around 400 nm is a result of the calibration curve, and not a significant feature.

The absorption of each sample was calculated as previously discussed in this section, and is shown in Table 4.5. Again, a clear correlation in the absorption values and film thickness can be seen, such that thicker films have higher rates of absorption. This trend is shown in Figure 4.42, which plots percent absorption as a function of film thickness.

Table 4.5: Absorption measurements at 405 nm of fused silica and Si-NC samples Q-1 and Q-2.

Measurement	Integrated Photon Flux (Photons/s/cm^2)	Total Absorption (Photons/s/cm^2)	Si-NC Absorption (Photons/s/cm^2)
Laser	2.27×10^{17}		
Fused Silica	2.26×10^{17}	6.51×10^{14} (0.29%)	
Th-1	2.19×10^{17}	7.77×10^{15} (3.43%)	7.12×10^{15} (3.15%)
Th-2	2.10×10^{17}	1.71×10^{16} (7.54%)	1.65×10^{16} (7.27%)
Th-3	1.85×10^{16}	1.85×10^{16} (8.17%)	1.79×10^{16} (7.91%)
Th-4	2.05×10^{17}	2.22×10^{16} (9.80%)	2.16×10^{16} (9.54%)
Th-7	2.01×10^{17}	2.54×10^{16} (11.19%)	2.47×10^{16} (10.93%)
Th-8	1.88×10^{17}	3.85×10^{16} (16.98%)	3.79×10^{16} (16.74%)
Th-9	1.67×10^{17}	6.00×10^{16} (26.46%)	5.94×10^{16} (26.25%)

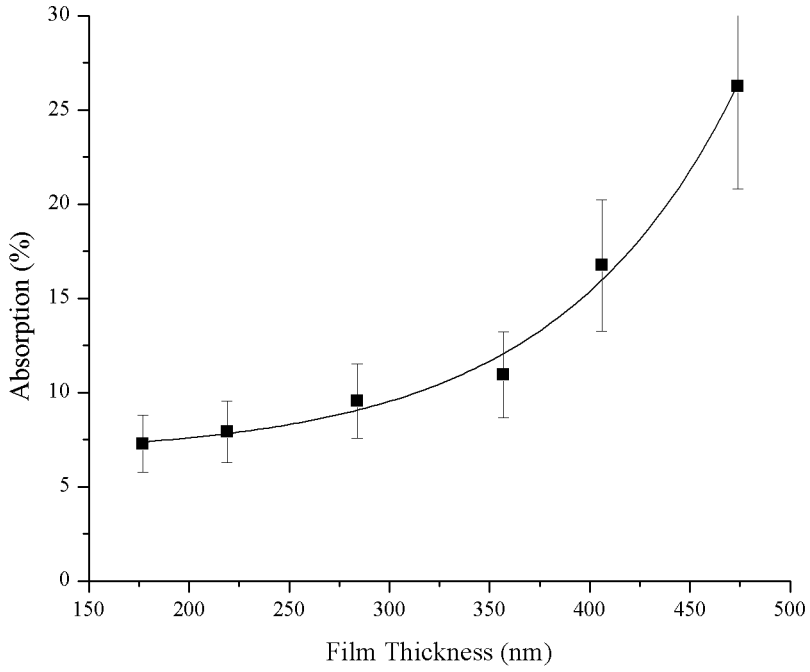

Figure 4.42: Absorption as a function of film thickness. Increased absorption is thought to be due to a larger number of Si-NCs in thicker films.

The increase in absorption in thicker films is due to the increased number of Si-NCs that are present in thicker films, as previously discussed in Section 4.3. The PL from the films was then measured inside the integrating sphere, manually smoothed, corrected for the sphere response, and converted into a photon flux. The resulting spectral photon fluxes are shown in Figure 4.43. It is clear that thicker samples show more Si-NC luminescence. These measurements were then used to calculate the quantum efficiencies of each sample, shown in Table 4.6.

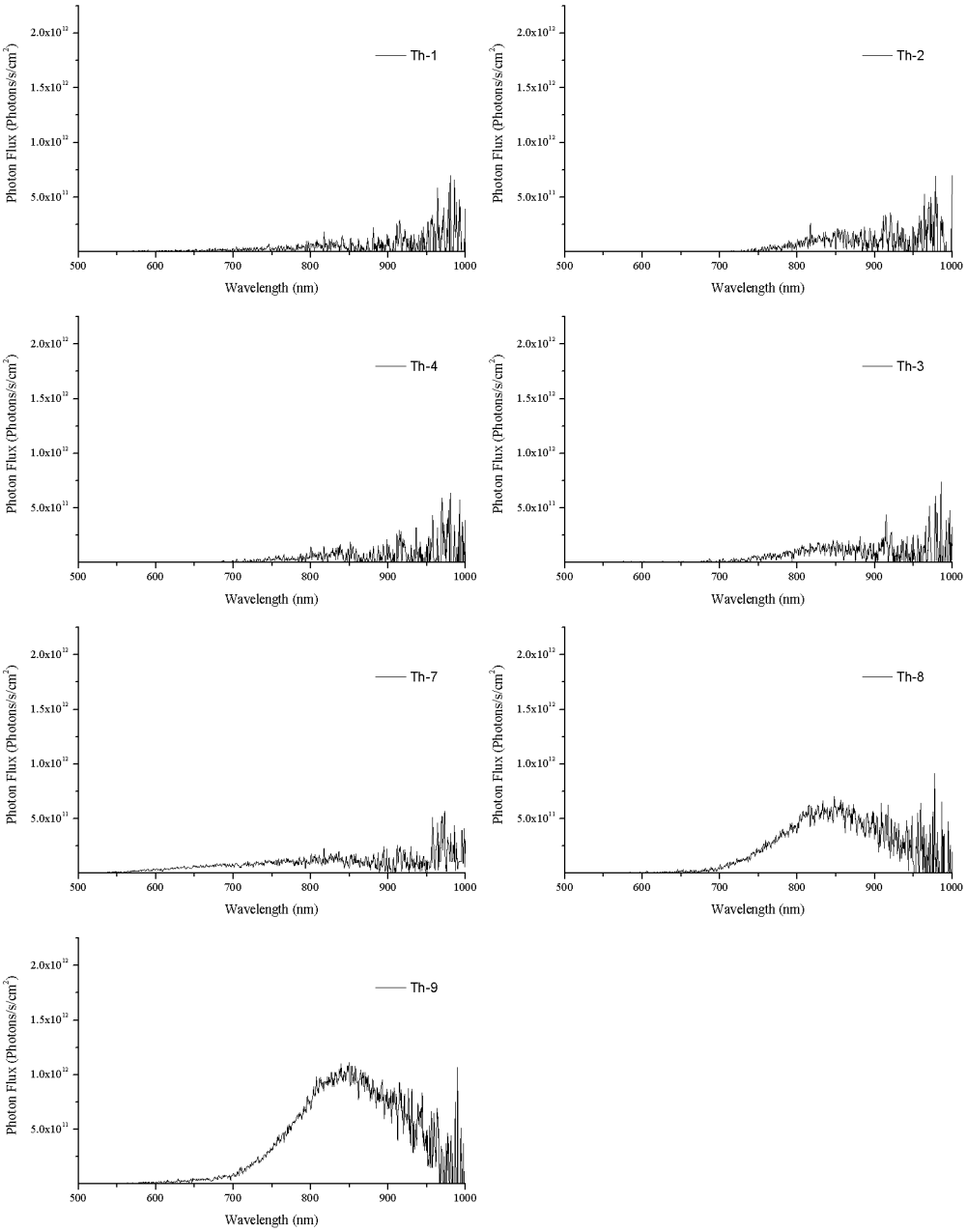

Figure 4.43: Photon flux for luminescent Si-NC samples of different film thicknesses measured inside an integrating sphere. A clear increase in signal strength is seen for thicker samples.

Table 4.6: Integrated photon flux and calculated quantum efficiencies of Si-NC samples of varying thicknesses.

Sample	Integrated photon flux	EQE	IQE of Converter	IQE of Si-NC	Thickness ±10 (nm)
Th-1	4.72×10^{13}	0.021%	0.61%	0.66%	102
Th-2	5.31×10^{13}	0.023%	0.31%	0.32%	180
Th-3	6.97×10^{13}	0.031%	0.38%	0.38%	238
Th-4	4.06×10^{13}	0.018%	0.18%	0.19%	307
Th-7	1.09×10^{14}	0.045%	0.43%	0.44%	364
Th-8	2.47×10^{14}	0.11%	0.64%	0.65%	430
Th-9	4.32×10^{14}	0.19%	0.72%	0.73%	484

When looking at the correlation between quantum efficiency and film thickness, trends begin to emerge. For EQE, there is a clear increase with increasing film thickness that is exponential in nature, as shown in Figure 4.44. This increase in EQE is due to the fact that thicker films emit stronger PL, and that PL EQE is defined as the ratio between emitted photons and incident photons.

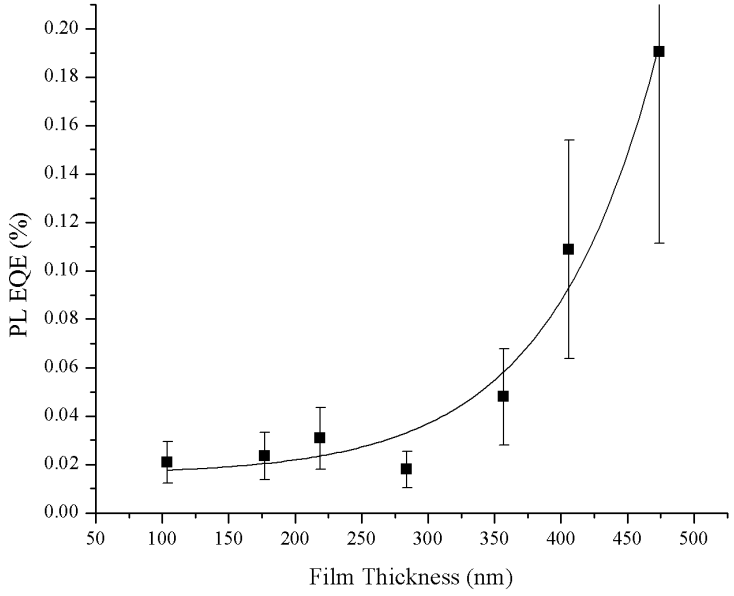

Figure 4.44: The relationship between photoluminescence external quantum efficiency and film thickness. A clear increase in EQE is seen for thicker films, following an exponential correlation.

Conversely, the correlation between PL IQE and film thickness does not seem to show a significant increase. As shown in the top of Figure 4.45, PL IQE stays relatively flat for films of different thicknesses. The outlying low QE values corresponding to Th-4 in Figure 4.44 and the top image of Figure 4.45 is likely due to contamination in the film that caused a degradation of the quantum efficiency.

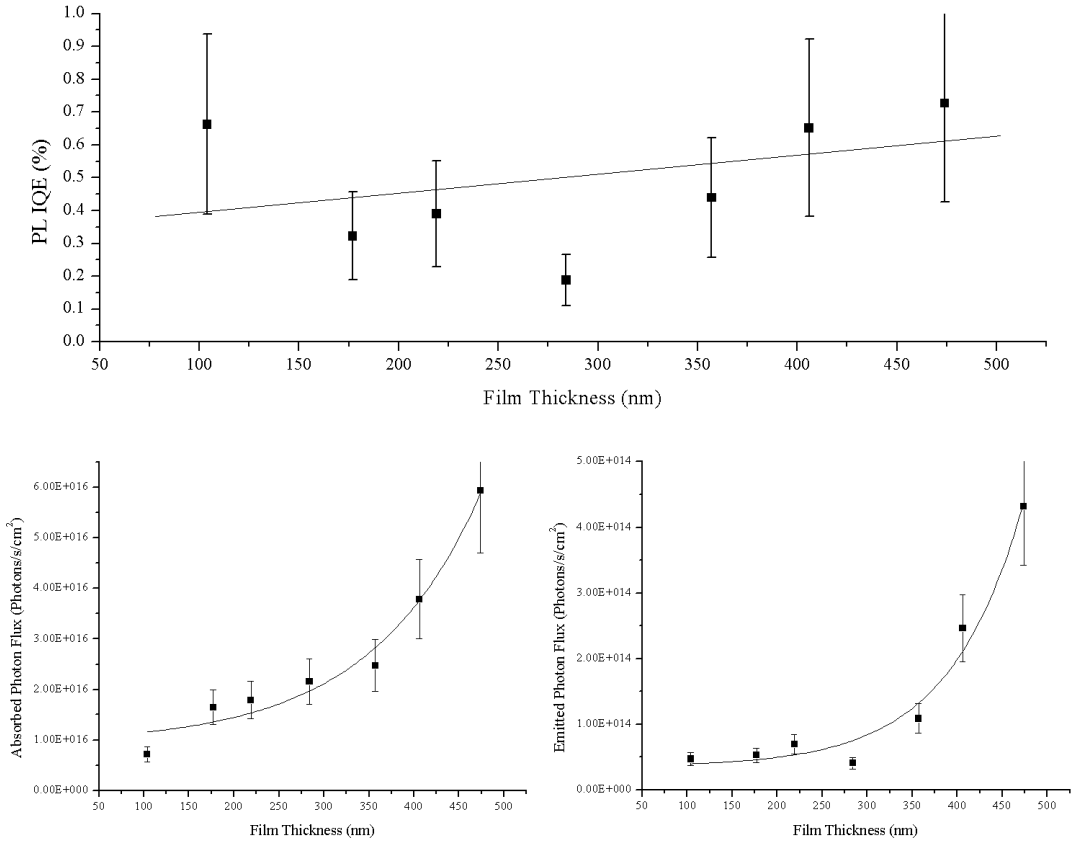

Figure 4.45: The relationship between photoluminescence internal quantum efficiency and film thickness (top); The integrated photon flux as a function of film thickness (bottom left), and the relationship between absorption and film thickness (bottom right). Negligible increase in IQE as a function of film thickness is seen.

The bottom of Figure 4.45 shows both the increase in emitted photon flux and absorbed photon flux with increasing film thickness. Since PL IQE is defined as the ratio between these two values, the IQE does not increase significantly. In order for the IQE to increase, the emitted photon flux would need to increase with respect to film thickness at a much higher rate than the absorbed photon flux. There is some evidence of this occurring, since the general trend of IQE versus film thickness is gradually increasing, however it is not apparent whether this is

coincidental or an actual trend. The error in QE measurements was determined using propagation of error on the EQE and IQE calculation processes.

4.5 Summary and Discussion

As a result of the experiments discussed in this chapter, silicon nanocrystals were successfully grown on silicon and fused silica substrates using ECR-PECVD. Initially, a calibration was done to determine optimal deposition parameters for Si-NC formation, and to determine ranges for tuning Si-NC emission. Calibration samples were characterized using variable-angle spectroscopic ellipsometry, and photoluminescence spectroscopy. Once Si-NCs were inferred through characteristic photoluminescence emission, films were deposited on fused silica substrates and similarly characterized. It was found that emission from a Si-NC film on a fused silica substrate was approximately twice as strong as emission from the same film on a silicon substrate. The photoluminescence internal and external quantum efficiencies were then measured using an integrating sphere setup. Efficiency results were on par with those in the literature for comparable materials.

Once deposition parameters for growing Si-NCs were obtained and reproduced, an experiment was done to determine the effect of varying the film thickness on optical parameters, photoluminescence, and photoluminescence quantum efficiency. Nine films were grown on silicon and fused silica substrates, however at least two films were contaminated by a leak in the PECVD system. The seven uncontaminated films were then characterized using the same methods as the calibration films, and it was seen that photoluminescence intensity and therefore EQE increased with increasing film thickness. Due to both the increased emission and absorption of the thicker films IQE did not show significant increases with respect to film thickness. Finally,

a transmission electron microscope was used to confirm the presence and size of the Si-NCs, as well as obtain information about the distribution of the Si-NCs throughout the film.

The presence of defects in the calibration films were observed for films that were not silicon-rich enough to form Si-NCs. These defects had intense visible photoluminescence that is unlikely to be easily reproducible or stable over time. The photoluminescence intensity decreased with high-temperature annealing proportionally to the amount of oxygen in the film. The defects resulted in a luminescence peak at about 2.2 eV, or 560 nm, and have been attributed to non-bridging oxygen-hole centres and oxygen vacancies [49], as well as self-trapped excitons in amorphous silicon dioxide [53].

Photoluminescence wavelength peaks from Si-NCs tended to be very sensitive to deposition parameters. It was observed that slight variations in oxygen flow or partial pressure resulted in drastic red or blue shifts in the photoluminescence peak of the resulting Si-NCs. In general, the Si-NCs grown were redder than is optimal for down-shifting applications, indicating that the Si-NCs were larger than intended. This could mean that the conditions required to form "small" Si-NCs on the order of 2-3 nm are much more rigid than the conditions for "large" Si-NCs on the order of 4-5 nm, such as those observed. In other words, there is likely a wider stoichiometry range for the formation of larger Si-NCs than for smaller Si-NCs. In thicker films, higher silicon content was observed through higher refractive indexes and red shifted photoluminescence peaks, though the deposition parameters were identical to thinner films with evidently lower silicon content. This indicates a correlation between film thickness and silicon incorporation, resulting in larger Si-NCs in thicker films. Since these thicker films also had stronger photoluminescence intensity and therefore higher EQE, deposition parameters would need to be adjusted based on the desired thickness.

For spectral engineering applications, these materials will need to be placed on the front or rear surface of a photovoltaic device. It is therefore important to understand how the materials behave from an optics perspective. Ellipsometry was used extensively to determine optical constants and measure transmission through semi-transparent samples deposited on fused silica. In most cases, a graded ellipsometric model resulted in more accurate results, indicating that excess silicon is not evenly distributed throughout the film. This was confirmed by TEM analysis, showing that nanocrystals near the surface of the film tend to be larger than those near the substrate. When modeled as an effective medium, such as the case in ellipsometry, this would result in an apparent decrease in silicon content near the surface of the film. The fact that the refractive index is graded with lower index near the surface and higher index near the substrate could be beneficial for photovoltaic applications. It has been shown that graded anti-reflection coatings (ARC) can be more effective than multi-layer ARCs [54], [55], [56] [57]. This provides potential for the spectral engineering layer to also act as an ARC for wavelengths that are not absorbed by the material.

Perhaps the most important metric when considering materials for down-conversion or down-shifting is the quantum efficiency of the photoluminescence process. This metric will determine whether enough photons are being re-emitted from the conversion material to improve the performance of an underlying photovoltaic device. Isolated and strictly oxygen-free Si-NCs passivated by organic ligands have been shown to have quantum efficiencies as high as 60% [30], however these efficient emitters are fabricated in very controlled laboratory conditions and are not feasible to be integrated into solar modules. The efficiency measured in this work was not extraordinarily high, however it did compare well with efficiencies in the literature for analogous materials. One of the main achievements of this work was the design and implementation of a measurement system for determining the quantum efficiency of photoluminescent materials.

Chapter 5

Conclusions and Future Work

This chapter will summarize the achievements pertaining to this work, and discuss problems that arose during research as well as future work that can be done to improve the results and reach the end goals of the project.

5.1 Conclusions

This work related to the objective of third-generation photovoltaics (PV): to achieve low-cost, high-efficiency devices. The broad goal was to study materials suitable for spectral engineering, a third-generation PV concept that aims to engineer the solar spectrum to better suit a PV device. This work specifically focused on down-shifting, the conversion of high-energy or ultraviolet (UV) photons, which are susceptible to high rates of surface recombination in semiconductor materials, into low-energy or visible photons which are more useful for a typical solar cell. Silicon nanocrystals (Si-NCs) fabricated using electron-cyclotron resonance plasma-enhanced chemical vapour deposition (ECR-PECVD) were studied as a down-shifting material for single-junction silicon cells. Silicon-rich silicon oxide thin films were deposited on silicon and fused silica substrates and then annealed at various temperatures up to 1150˚C for one hour in flowing H_2 (5%) N_2 (95%) to form Si-NCs. A calibration was initially done to determine optimal deposition parameters for Si-NC formation. An experiment was then done to determine the effect of film thickness on emission, optical properties, and photoluminescence quantum efficiencies.

Photoluminescence spectroscopy, excited at 325 nm and collected through a calibrated CCD, was used to characterize the emission of the Si-NCs, which was Gaussian in nature due to

the size distribution of the Si-NCs. The photoluminescence peaks varied depending on the stoichiometry of the films, ranging from approximately 790 nm to 850 nm. Variable-angle spectroscopic ellipsometry was used to determine the refractive indexes, extinction coefficients, and transmission properties of the Si-NC films. The absorption of the films was determined from the extinction coefficients, and showed strong absorption below 500 nm, ideal for a down-shifting material. The indexes of refraction were seen to be graded throughout each film, with a lower index near the surface of the film and higher index near the substrate. This indicated a non-uniform distribution of excess silicon throughout the films. Transmission Electron Microscopy (TEM) was used to determine the size, density, and distribution of Si-NCs in two of the films. Si-NCs were seen to have an average diameter of approximately 4 nm, with larger nanocrystals more common near the surface of the film, correlating with the graded refractive index previously mentioned. A density of approximately 10^5 nanocrystals per cubic micron was approximated from one of the TEM samples.

One of the major achievements of this work was the design and implementation of a photoluminescence quantum efficiency measurement system. This system used an integrating sphere to measure the absolute efficiency of Si-NC emission, and can be used similarly for any light-emitting material. The efficiencies of Si-NC thin films were measured, and found to range from 0.19% to 1.84% for internal quantum efficiency (IQE), and 0.021% to 0.19% for external quantum efficiency (EQE). The EQE was found to increase with thicker films due to more intense photoluminescence; however the IQE remained relatively independent of film thickness. Though these efficiencies were not very high, they are comparable to those found in the literature for similar materials. These results showed the difficulty in achieving highly-efficient light emission from silicon devices, however provided a benchmark for future work relating to down-shifting using Si-NCs.

5.1.1 PECVD System Maintenance

The ECR-PECVD system is complex and as with any high-vacuum system requires ongoing maintenance. One of the biggest challenges of this research was dealing with mechanical failures on the system that took weeks or months to repair. Issues with the diffusion and turbo pumps and motors that controlled the sample stage caused the system to be unusable for extended periods of time. In addition, the flange that was attached to the shutter appeared to be leaking air into the chamber. This likely caused a degradation of deposition pressure, as well as unwanted contaminants incorporating into the film. Improving the reliability of the system would go a long way in improving the quality of the materials produced. That being said, when the system was operational, it worked rather well and provided reproducible results. There was an in-situ ellipsometer attached to the system that was not operational, however would have provided an excellent way of tracking film composition and thickness in real time.

5.1.2 Quantum Efficiency Setup Improvements

The photoluminescence quantum efficiency measurement setup worked relatively well when considering the difficulty of such a measurement. Initially, a Teflon sample holder was designed and built by the machine shop at McMaster University, however due to the nature of the material and the design, the sample holder was bulky and likely absorbed or blocked some of the emission from the sample being held. As a fast and cheap alternative, a piece of wire was bent into shape such that it was able to suspend a sample of any size in the centre of the integrating sphere. This proved to work better than the Teflon sample holder, though it was susceptible to any movement or vibration. It would be a good investment to build a more rigid and stable sample holder that would work with different sized samples.

Noise was also a problem when measuring photoluminescence quantum efficiency. Because of the inefficient coupling of light out of the exit port of the sphere into an optical fibre, very long integration times were required for detecting even the slightest photoluminescence signals from the sphere. This could perhaps be improved by chopping the excitation source and adding a lock-in amplifier to the detection system.

In this work, quantum efficiency was only measured at a single wavelength, corresponding to the excitation laser which operated at 405 nm. It would be very useful to be able to calculate spectral quantum efficiency. Initially, a monochromator attached to a broadband mercury lamp was used in conjunction with the setup. It was found that the monochromated light intensity was not sufficient to excite photoluminescence from Si-NC samples. In addition, a stronger excitation source would yield a stronger photoluminescence signal and therefore higher signal-to-noise ratio. A tunable laser or strong broadband lamp such as a xenon arc lamp would suffice to provide intense monochromatic excitation power over the required wavelength range of approximately 250 nm to 550 nm. This would be particularly useful for spectral engineering since it is required to know the quantum efficiency of a converter over a range of absorbed wavelengths.

5.2 Future Work

5.2.1 Rare-Earth Doping

Rare-earths have the potential to be very efficient emitters, as well as down-converters. The next step of this research would be to dope Si-NC thin-films with rare-earth ions that emit light in the NIR, such as Ytterbium or Europium. Coupling two rare-earths together would also be a prudent step, to achieve energy transfer from a sensitizer ion to an emitter ion. Emission from rare-earth ions also has the potential to be more efficient than Si-NCs, since the emission occurs through a direct process. The PECVD system used in this work has the capability to deposit

multiple rare-earths, and could be utilized to calibrate and optimize rare-earth emission and even produce down-conversion.

5.2.2 Solar Cell Coupling

The ultimate goal of this work is to produce a material that will improve solar cell performance. Even if the photoluminescence efficiency is not high enough to increase solar cell efficiency, it could still be useful to incorporate the material on a solar cell to see how it affects the cell response. This would be particularly useful on cells that have poor response in the ultraviolet. Evidence of improvement could be seen if the quantum efficiency of the cell is improved at shorter wavelengths after applying even an inefficient conversion material. A good coupling method is needed to attach the conversion material to the cell. Directly depositing the material on the cell is not an option, since high-temperature annealing is required to form Si-NCs, and a typical cell would not withstand such temperatures. The converter could be incorporated into an encapsulation layer, or attached with an epoxy onto the top of an exposed cell. Care would need to be taken to ensure that intermediate refractive indexes of any layers on top of the cell are increasing towards the cell, otherwise losses from reflection could be problematic.

Bibliography

[1] D. Goodstein, Out of Gas: The End of the Age of Oil, New York: W. W. Norton & Company, 2004.

[2] D. J. MacKay, Sustainable Energy - without the hot air, Cambridge: UIT Cambridge Ltd., 2009.

[3] K. H. Solangi, M. R. Islam, R. Saidur, N. A. Rahim and H. Fayaz, "A review on solar energy policy," *Renewable and Sustainable Energy Reviews,* vol. 15, pp. 2149-2163, 2011.

[4] T. Weis and P. J. Partington, "Behind the Switch: Pricing Ontario Electricity Options," The Pembina Institute, Drayton Valley, Alberta, 2011.

[5] W. Shockley and H. Queisser, "Detailed balance limit of efficiency of p-n junction solar cells," *Journal of Applied Physics,* vol. 32, no. 3, p. 510, 1961.

[6] G. Conibeer, "Third Generation Photovoltaics," *Materials Today,* vol. 10, no. 11, pp. 42-50, 2007.

[7] M. Wolf, "Limitations and possibilities for improvement of photovoltaic solar energy converters," *Proceedings of the IRE,* vol. 48, p. 1246, 1960.

[8] L. Antonio and M. Antonio, "Increasing the efficiency of ideal solar cells by photon induced transitions at intermediate levels," *Physical Review Letters,* vol. 78, no. 26, p. 5014, 1997.

[9] C. Tablero, P. Palacios, J. J. Fernandez and P. Wahnon, "Properties of intermediate band materials," *Solar Energy Materials & Solar Cells,* vol. 87, pp. 323-331, 2005.

[10] I. Aguilera, P. Palacios and P. Wahnon, "Enhancement of optical absorption in Ga-chalcopyrite-based intermediate-band materials for high efficiency solar cells," *Solar Energy Materials & Solar Cells,* vol. 94, pp. 1903-1906, 2010.

[11] L. Cuadra, A. Marti and A. Luque, "Present status of intermediate band solar cell research," *Thin solid films,* Vols. 451-452, pp. 593-599, 2004.

[12] R. P. Raffaelle, S. L. Castro, A. F. Hepp and S. G. Bailey, "Quantum dot solar cells," *Progress in Photovoltaics: Research and Applications,* vol. 10, pp. 433-439, 2002.

[13] S. Jenks and R. Gilmore, "Quantum dot solar cells: Materials that produce two intermediate bands," *Journal of Renewable and Sustainable Energy,* vol. 2, p. 013111, 2010.

[14] A. Shalav, B. S. Richards and M. A. Green, "Luminescent layers for enhanced silicon solar cell performance: Up-conversion," *Sol. Energ. Mat. Sol. C.,* vol. 91, no. 9, pp. 829-842, 2007.

[15] T. Trupke, M. A. Green and P. Wurfel, "Improving solar cell efficiencies by down-conversion of high-energy photons," *Journal of Applied Physics,* vol. 92, no. 3, pp. 1668-1674, 2002.

[16] B. S. Richards and K. R. McIntosh, "Overcoming the poor short wavelength spectral response of CdS/CdTe photovoltaic modules via luminescence down-shifting," *Progress in Photovoltaics: Research and Applications,* vol. 15, p. 27, 2007.

[17] C. Strumpel, M. McCann, G. Beaucarne, V. Arkhipov, A. Slaoui, V. Svrcek, C. del Canizo and I. Tobias, "Modifying the solar spectrum to enhance silicon solar cell efficiency - an overview of available materials," *Solar Energy Materials and Solar Cells,* vol. 91, pp. 238-249, 2007.

[18] B. S. Richards, "Luminescent layers for enhanced silicon solar cell performance: down-conversion," *Sol. Energ. Mat. Sol. C.,* vol. 90, no. 9, pp. 1189-1207, 2006.

[19] H. Shpaisman, O. Niitsoo, I. Lubomirsky and D. Cahen, "Can up- and down-conversion and multi-exciton generation improve solar photovoltaics?," *Solar Energy Materials and Solar Cells,* vol. 92, pp. 1541-1546, 2008.

[20] L. Canham, "Silicon quantum wire array fabrication by electrochemical and chemical dissolution of wafers," *Applied Physics Letters,* vol. 57, p. 1046, 1990.

[21] S. J. Fonash, Solar Cell Device Physics, Burlington, MA: Academic Press, 2010.

[22] J. Heitmann, F. Muller, M. Zacharias and U. Gosele, "Silicon nanocrystals: size matters," *Advanced Materials,* vol. 17, no. 7, p. 795, 2005.

[23] L. Pavesi, L. Dal Negro, C. Mazzoleni, G. Franzo and F. Priolo, "Optical gain in silicon nanocrystals," *Nature,* vol. 408, p. 440, 2000.

[24] F. Iacona, G. Franzo and C. Spinella, "Correlation between luminescence and structural properties of Si nanocrystals," *Journal of Applied Physics,* vol. 87, no. 3, p. 1295, 2000.

[25] Y. Q. Wang, G. L. Kong, W. D. Chen, H. W. Diao, C. Y. Chen, S. B. Zhang and X. B. Liao, "Getting high-efficiency photoluminescence from Si nanocrystals in SiO2 matrix," *Appl. Phys. Lett.,* vol. 81, no. 22, p. 4174, 2002.

[26] D. Timmerman, I. Izeddin, P. Stallinga, I. N. Yassievich and T. Gregorkiewicz, "Space-separated quantum cutting with silicon nanocrystals for photovolatic applications," *Nature Photonics,* vol. 2, no. 2, pp. 105-109, 2008.

[27] L. Pavesi, L. Dal Negro, C. Mazzoleni, G. Franzo and F. Priolo, "Optical gain in silicon

nanocrystals," *Nature*, vol. 408, no. 6811, pp. 440-444, 2000.

[28] D. C. Hannah, J. Yang, P. Podsiadlo, M. K. Chan, A. Demortiere, D. J. Gosztola, V. B. Prakapenka, G. C. Schatz, U. R. Kortshagen and R. D. Schaller, "On the origin of photoluminescence in silicon nanocrystals: Pressure-dependent structural and optical studies," *Nano Letters*, 2012.

[29] D. Kovalev, J. Diener, H. Heckler, G. Polisski, N. Kunzner and F. Koch, "Optical absorption cross sections of si nanocrystals," *Physical Review B*, vol. 61, no. 7, p. 4485, 2000.

[30] D. Jurbergs, L. Rogojina, L. Mangolini and U. Kortshagen, "Silicon nanocrystals with ensemble quantum yields exceeding 60%," *Appl. Phys. Lett.*, vol. 88, p. 233116, 2006.

[31] G. Dieke and H. Crosswhite, "The spectra of the doubly and triply ionized rare earths," *Applied Optics*, vol. 2, no. 7, pp. 675-686, 1963.

[32] A. J. Kenyon, "Recent developments in rare-earth doped materials for optoelectronics," *Progress in Quantum Electronics*, vol. 26, pp. 225-284, 2002.

[33] J. Li, H. Y. Zalloum, T. Roschuk, C. L. Heng, J. Wojcik and P. Mascher, "Light emission from rare-earth doped silicon nanostructures," *Advances in Optical Technologies*, vol. 10, p. 295601, 2008.

[34] W. W. Piper, J. A. DeLuca and F. S. Ham, "Cascade fluorescent decay in Pr3+ doped fluorides," *Journal of Luminescence*, vol. 8, no. 4, pp. 344-348, 1974.

[35] V. D. Rodriguez, V. K. Tikhomirov, J. Mendez-Ramos, A. C. Yanes and V. V. Moshchalkov, "Towards broad range and highly efficient down-conversion of solar spectrum by Er3+-Yb3+ co-doped nano-structured glass-ceramics," *Solar Energy Materials and Solar Cells*, vol. 94, pp. 1612-1617, 2010.

[36] H. Lin, D. Chen, Y. Yu, Z. Shan, P. Huang, A. Yang and Y. Wang, "Broadband UV excitable near-infrared downconversion luminescence in Eu2+/Yb3+:CaF2 nanocyrstals embedded in glass ceramics," *Journal of Alloys and Compounds*, vol. 509, pp. 3363-3366, 2011.

[37] T. Roschuk, J. Wojcik, E. A. Irving, M. Flynn and P. Mascher, "Silicon nanocrystal formation in silicon rich silicon oxide thin films," *Proceedings of SPIE*, 2004.

[38] D. Comedi, O. H. Y. Zalloum, J. Wojcik and P. Mascher, "Light emission from hydrogenated and unhydrogenated Si-nanocrystals/Si dioxide composites based on PECVD-grown Si-rich Si-oxide films," *IEEE Journal of Selected Topics in Quantum Electronics*, vol. 12, no. 6, p. 1561, 2006.

[39] D. Comedi, O. H. Y. Zalloum, E. A. Irving, J. Wojcik, T. Roschuk, M. J. Flynn and P. Mascher, "X-ray diffraction study of crystalline Si nanocluster formation in annealed silicon-rich silicon oxides," *Journal of Applied Physics*, vol. 99, p. 023518, 2006.

[40] G. Dresselhaus, A. F. Kip and C. Kittel, "Observation of cyclotron resonance in germanium crystals," *Physical Review,* vol. 92, no. 3, p. 827, 1953.

[41] G. Dresselhaus, A. F. Kip and C. Kittel, "Cyclotron resonance of electrons and holes in silicon and germanium crystals," *Physical Review,* vol. 98, no. 2, p. 368, 1955.

[42] H. Fujiwara, Spectroscopic Ellipsometry: Principles and Applications, John Wiley & Sons Ltd., 2007.

[43] Labsphere, "A Guide to Integrating Sphere Theory and Applications," 2011.

[44] SphereOptics, "Integrating Sphere Design and Applications," SphereOptics L.L.C., 2007.

[45] A. Johnson, S. Lee, J. Klein and J. Kanicki, "Absolute photoluminescence quantum efficiency measurement of light-emitting thin films," *Rev. Sci. Instrum.*, vol. 78, no. 9, p. 096101, 2007.

[46] N. C. Greenham, I. W. Samuel, G. R. Hayes, R. T. Phillips, Y. Kessener, S. C. Moratti, A. B. Holmes and R. H. Friend, "Measurement of absolute photoluminescence quantum efficiencies in conjugated polymers," *Chemical Physics Letters,* vol. 241, pp. 89-96, 1995.

[47] K. Potrick, T. Schmidt, S. Bublitz, C. Muhlig, W. Paa and F. Huisken, "Determination of the photoluminescence quantum efficiency of silicon nanocrystals by laser-induced deflection," *Applied Physics Letters,* vol. 98, p. 083111, 2011.

[48] O. H. Y. Zalloum, M. Flynn, T. Roschuk, J. Wojcik, E. Irving and P. Mascher, "Laser photoluminescence spectrometer based on charge-coupled device detection for silicon-based photonics," *Reveiw of Scientific Instruments,* vol. 77, p. 023907, 2006.

[49] M. Zhu and Y. Han, "The origin of visible photoluminescence from silicon oxide films prepared by dual plasma chemical vapor deposition," *Journal of Applied Physics,* vol. 83, no. 10, p. 5386, 1998.

[50] A. J. Kenyon, P. F. Trwoga and C. W. Pitt., "The origin of photoluminescence from thin films of silicon-rich silica," *Journal of Applied Physics,* vol. 79, no. 12, p. 9291, 1996.

[51] D. Amans, S. Callard, A. Gagnaire and J. Joseph, "Ellipsometric study of silicon nanocrystal optical constants," *Journal of Applied Physics,* vol. 93, no. 7, p. 4173, 2003.

[52] C.-F. Lin, W.-T. Tseng and M. S. Feng, "Formation and characteristics of silicon nanocrystals in plasma-enhanced chemical-vapor-deposited silicon-rich oxide," *Journal of Applied Physics,* vol. 87, no. 6, p. 2808, 2000.

[53] W. C. Choi, M.-S. Lee, E. K. Kim, C. K. Kim and S.-K. Min, "Visible luminescence from thermally grown silicon dioxide thin films," *Applied Physics Letters,* vol. 69, no. 22, p. 3402, 1996.

[54] A. Mahdjoub and L. Zighed, "New designs for graded refractive index antireflection coatings," *Thin Solid Films,* vol. 478, pp. 299-304, 2005.

[55] S. Chhajed, M. F. Schubert, J. K. Kim and E. F. Schubert, "Nanostructured multilayer graded-index antireflection coating for Si solar cells with broadband and omnidirectional characteristics," *Applied Physics Letters,* vol. 93, p. 251108, 2008.

[56] C.-H. Sun, P. Jiang and B. Jiang, "Broadband moth-eye antireflection coatings on silicon," *Applied Physics Letters,* vol. 92, p. 061112, 2008.

[57] Y. Huang, S. Chattopadhyay and Y. Jen, "Improved broadband and quasi-omnidirectional anti-reflection properties with biomimetic silicon nanostructures," *Nature Nanotechnology,* vol. 2, p. 770, 2007.

Appendix A: Integrating Sphere Parameters

Table A.1: Spectral reflectance of the integrating sphere's interior coating (Spectralon).

Wavelength (nm)	Spectralon Reflectance (%)
250	0.95
300	0.985
400	0.99
500	0.991
600	0.992
700	0.992
800	0.991
900	0.991
1000	0.993
1100	0.993
1200	0.992
1300	0.992
1400	0.991
1500	0.991
1600	0.991
1700	0.988
1800	0.989
1900	0.981
2000	0.976
2100	0.953
2200	0.973
2300	0.972
2400	0.955
2500	0.95

Table A.2: Specific parameters for the integrating sphere that was used in this work.

Parameter	Value
Input port radius	0.25 inches
Output port radius	0.25 inches
Sphere radius	1.65 inches
Port fraction	0.01148
Fibre facial reflectivity	0.03
Fibre core diameter	7.87e-3 inches
Fibre numerical aperture (NA)	0.22

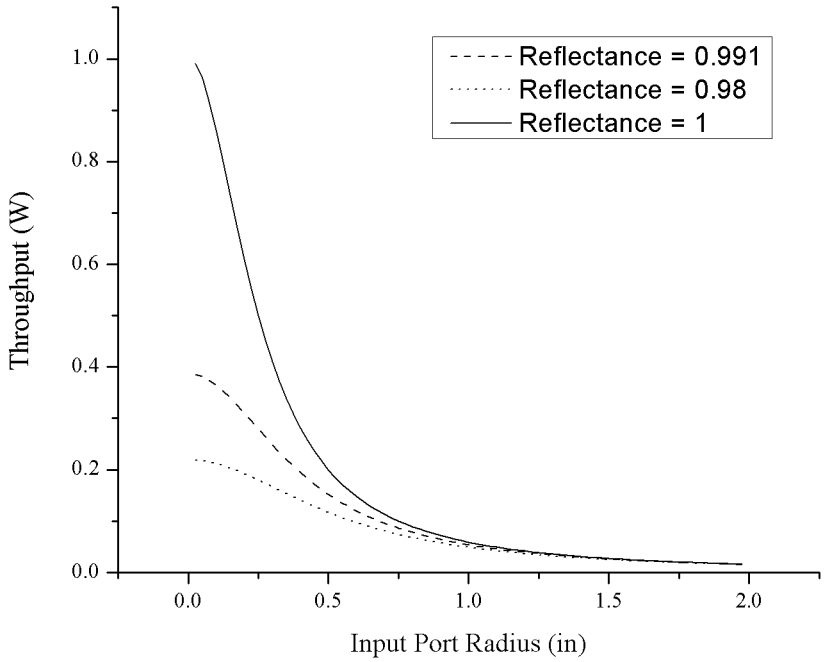

Figure A.1: Effect of interior wall reflectance and input port size on throughput at output port. Assumed input energy is 1 Watt. It can be seen that with perfect reflectance and an input port radius approaching zero, the throughput approaches 1 Watt, indicating no loss in the system.

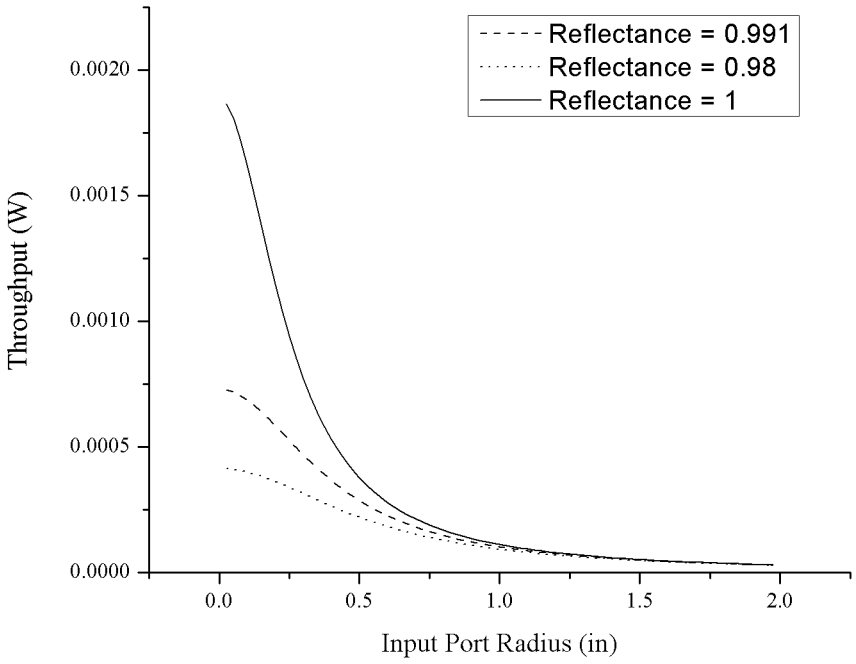

Figure A.2: Effect of interior wall reflectance and input port size on throughput using a coupled fibre. Assumed input energy is 1 Watt. Note that even with perfect reflectance and an input port radius approaching zero, there is still significant loss through in the system.

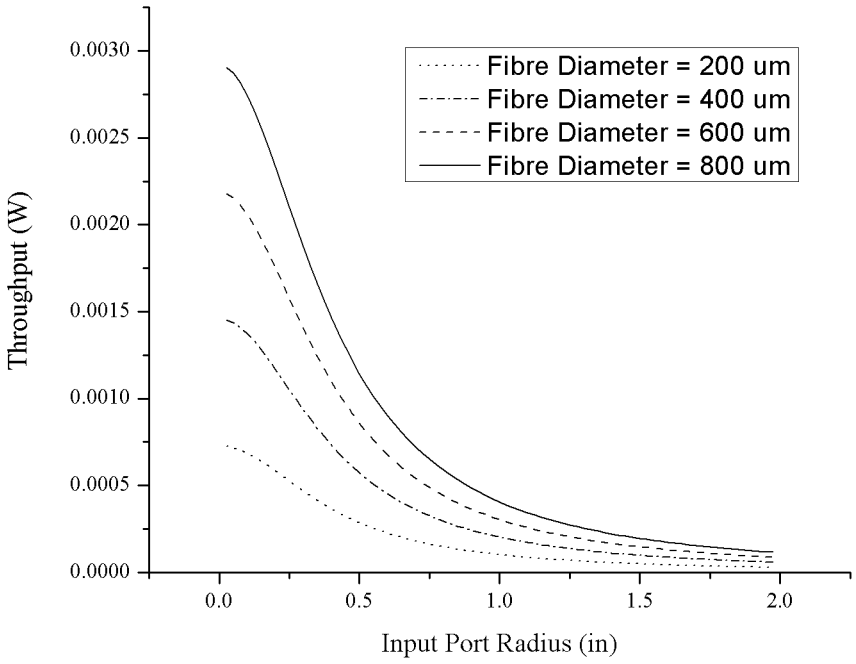

Figure A.3: Effect of fibre diameter on throughput as a function of input port radius.

Appendix B: Properties of Common Materials

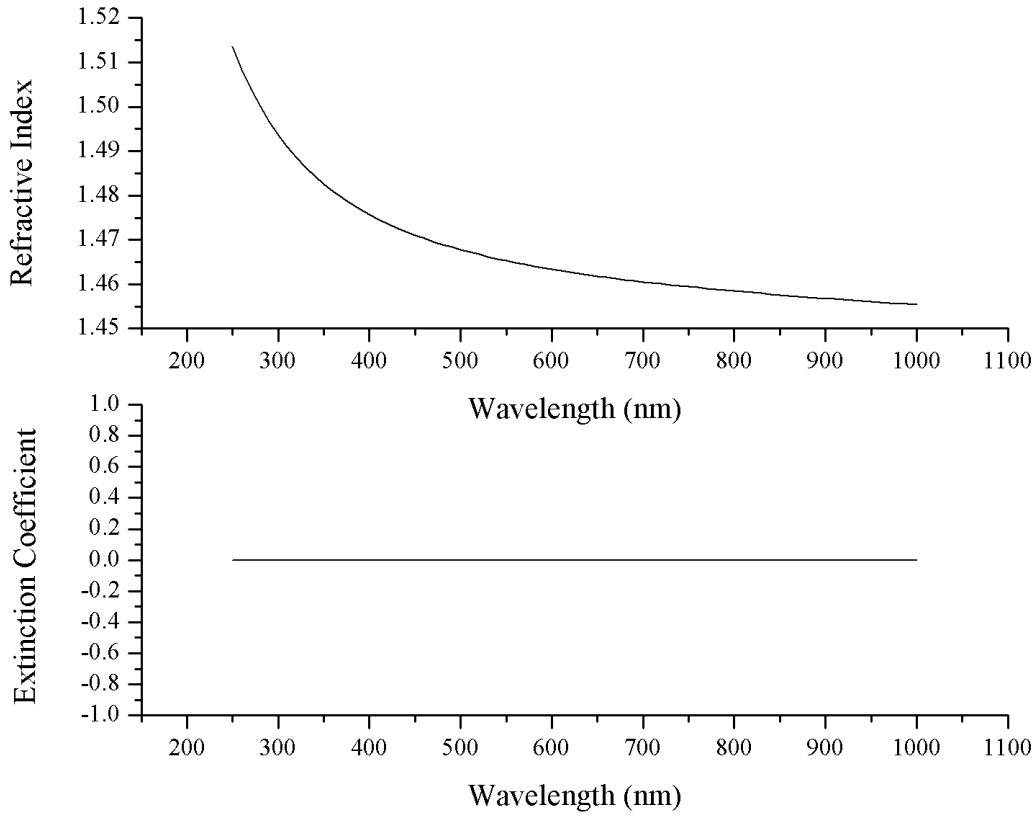

Figure B.1: Optical properties of silicon dioxide/ fused silica.

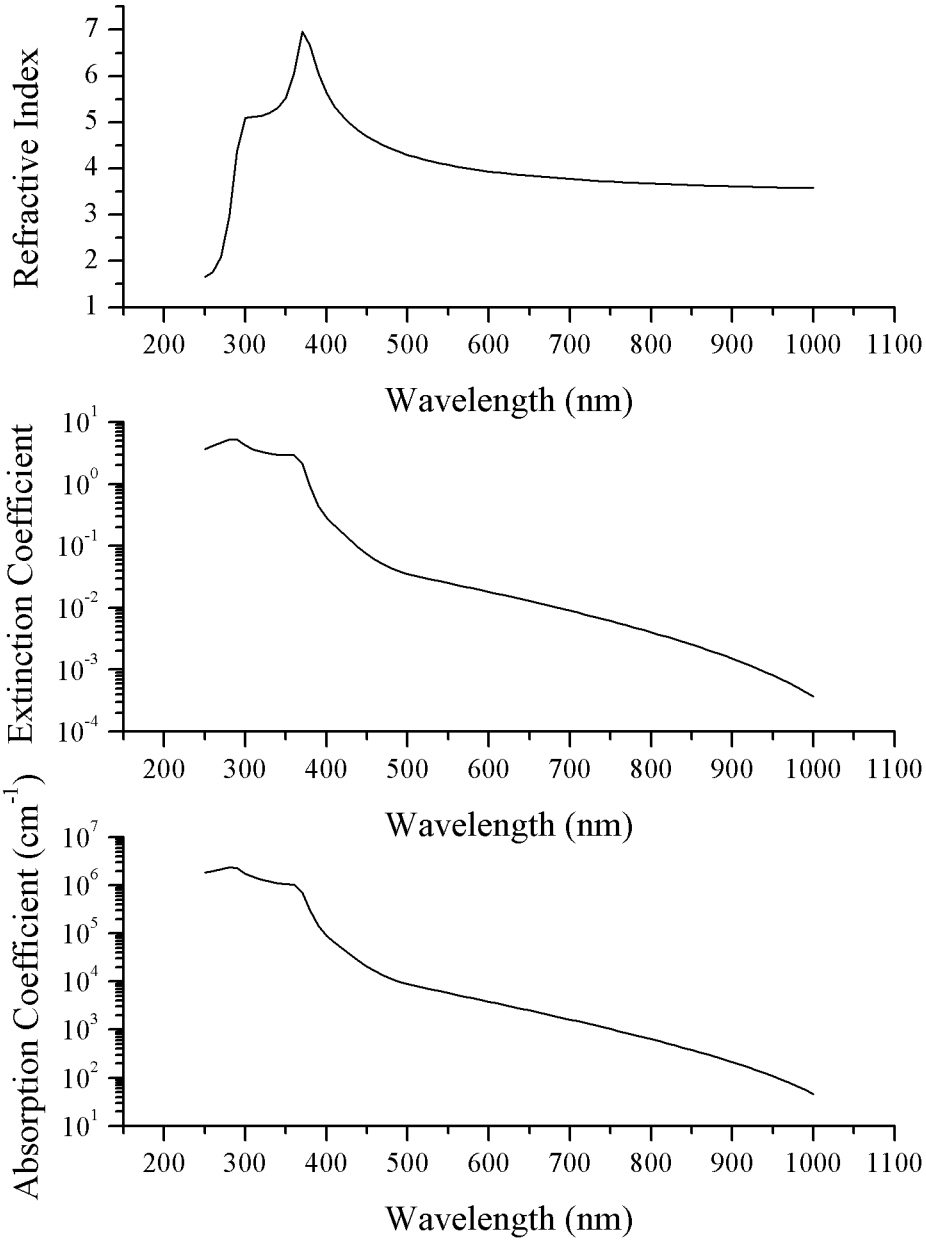

Figure B.2: Optical properties of silicon.

Appendix C: Optical Constants of Films of Varying Thicknesses

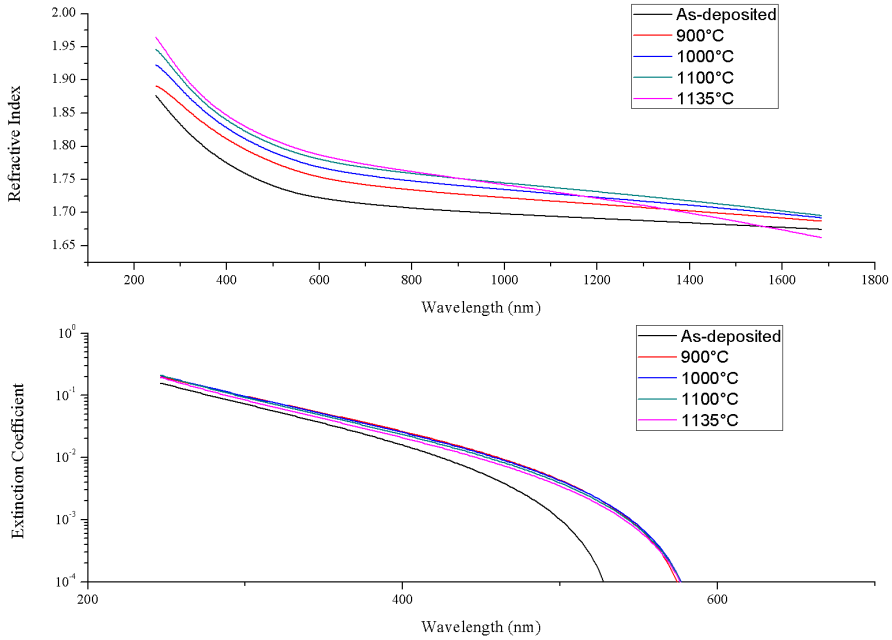

Figure C.1: Refractive index and extinction coefficient for Th-1 after annealing at various temperatures.

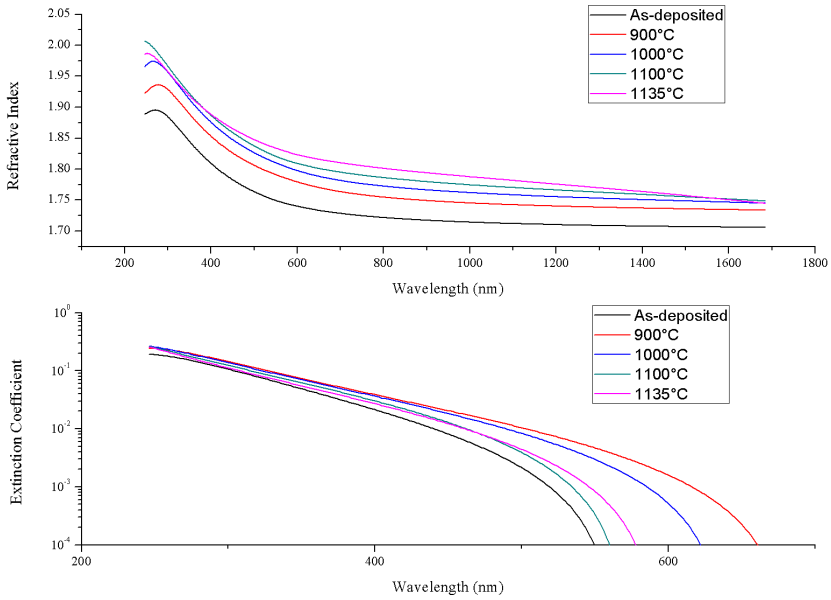

Figure C.2: Refractive index and extinction coefficient for Th-2 after annealing at various temperatures.

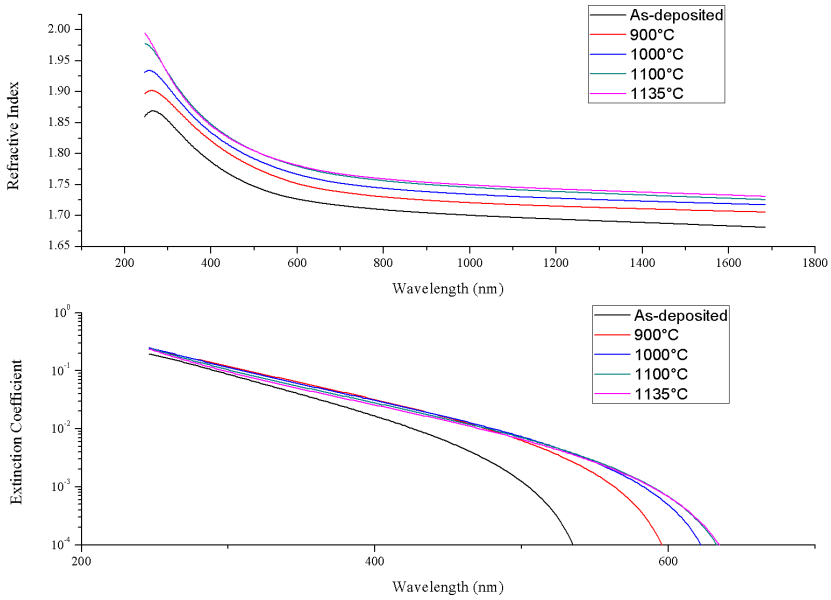

Figure C.3: Refractive index and extinction coefficient for Th-3 after annealing at various temperatures.

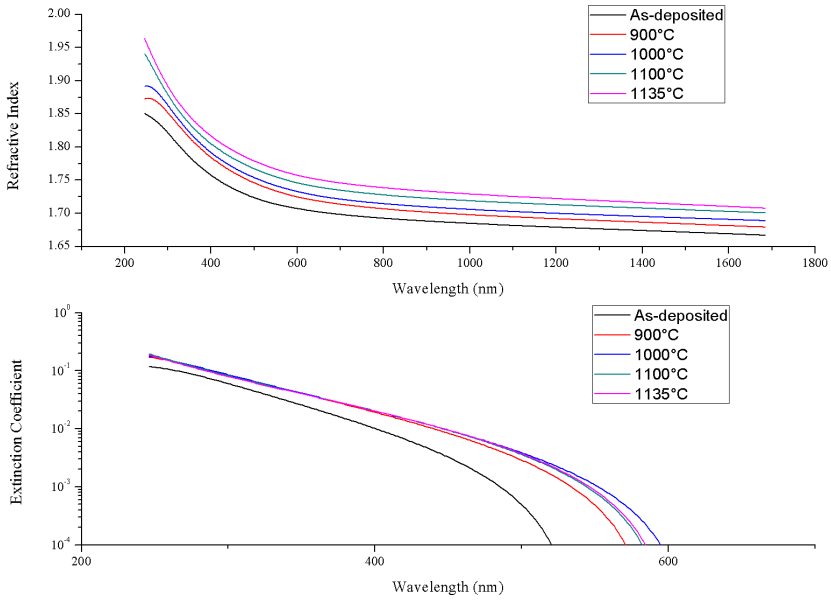

Figure C.4: Refractive index and extinction coefficient for Th-4 after annealing at various temperatures.

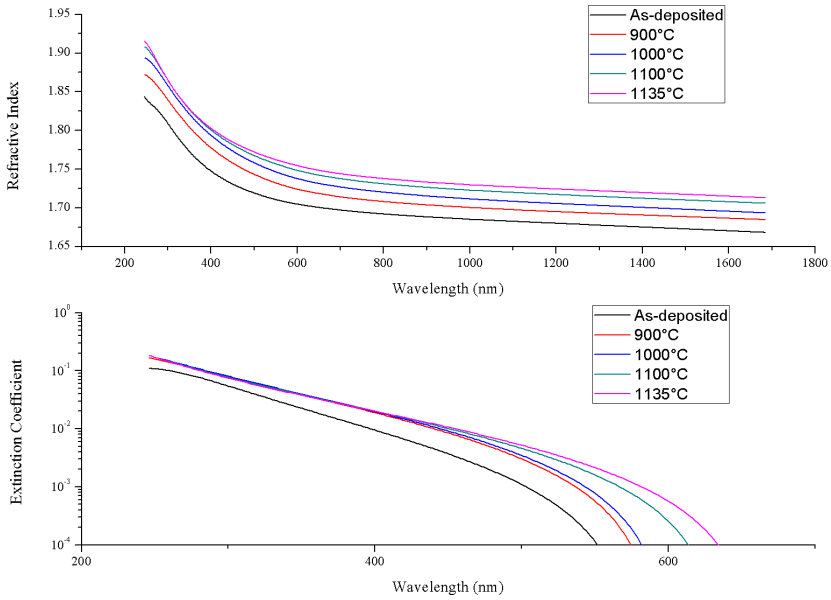

Figure C.5: Refractive index and extinction coefficient for Th-7 after annealing at various temperatures.

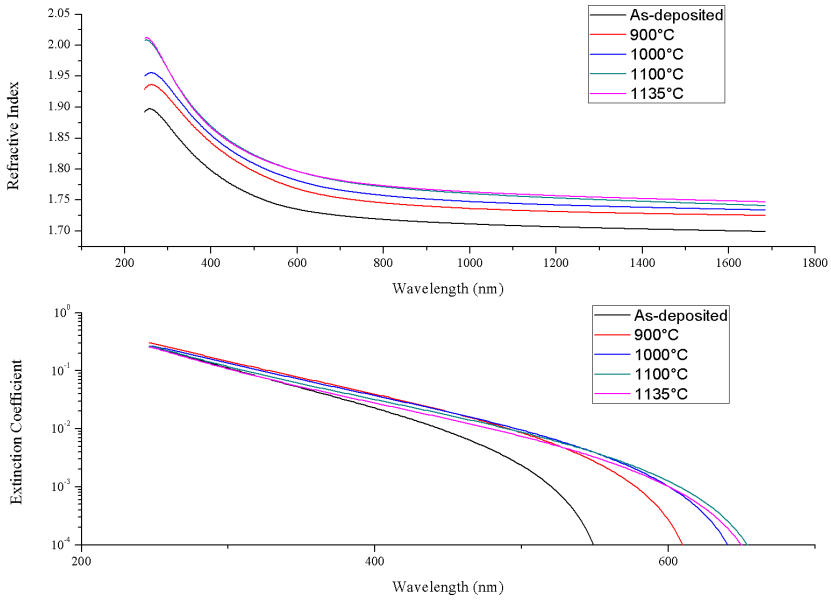

Figure C.6: Refractive index and extinction coefficient for Th-8 after annealing at various temperatures.

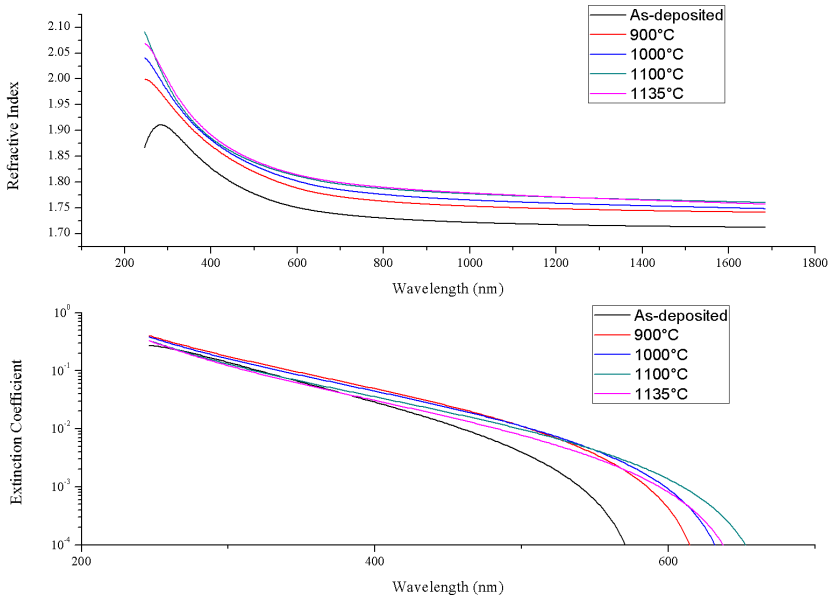

Figure C.7: Refractive index and extinction coefficient for Th-9 after annealing at various temperatures.